CROSS-COUPLING BETWEEN DEVICE-LEVEL CFD AND OCEANOGRAPHIC MODELS APPLIED TO TISECS IN MINAS PASSAGE AND PETIT PASSAGE

FINAL REPORT

Submitted: February 11th, 2013

Reporting Period: October 1st, 2012 – February 11th, 2013

Project No.: 305-170.014

Prepared For: **Offshore Energy Research Association of Nova Scotia**
5151 George Street, Suite 602
Halifax, NS B3J 1M5
Tel: 902 424-0789
Attention: Nalani Perry

Project Partners: **Mavi Innovations Inc**. (Principal Investigator)
307-865 West 15th Ave
Vancouver, BC, V5Z 1R8
Tel: 778 899-7007
www.mavi-innovations.ca
Contact: Voytek Klaptocz, *voytek@Mavi-innovations.ca*
Timothy Waung, *tim@Mavi-innovations.ca*

University of Victoria
Dept. of Mechanical Engineering, Institute of Integrated Energy Systems
PO Box 3055 STN CSC
Victoria, BC, V8W 3P6
Tel: 250 721-7969
www.ssdl.uvic.ca
Contact: Dr. Curran Crawford, *curranc@uvic.ca*
Michael Shives, *mrshives@uvic.ca*

Acadia University
Dept. of Mathematics and Statistics
12 University Ave. Wolfville, NS, B4P 2R8
Tel: 902 585-1608
www.acadiau.ca
Contact: Dr. Richard Karsten, *rkarsten@acadiau.ca*

Cascadia Coast Research
2576 Cook Street
Victoria, B.C. V8T 3R9
Tel: 778 433-7682
***Contact*:** Clayton Hiles, *clayton@cascadiacoast.com*
Roy Walters, *rawalters@gmail.com*

LIST OF REVISIONS

Rev No.	Issue Date	Description	Prepared By:
0	Feb. 11th, 2012	Initial Issue of Final Report	VK, TW,CC, RK, CH, MS, RW
1	May 14th, 2013	For public release. Removal of project execution details. Minor correction to Minas Passage power estimates.	CH

This work is dedicated to the memory of the late Michael Tarbotton of Triton Consultants who spearhead the initiative to take up this work. Through this project, he spawned a new generation of modelers, who, by following his example, will continue to push the boundaries of tidal models to ensure the successful, safe and environmentally benign build out of tidal power projects.

SUMMARY

This project set out to develop a link between Oceanographic computer models and Computational Fluid Dynamics (CFD) models in order to improve state of the art modeling techniques used for resource assessments and tidal turbine siting for both single and multiple TISECs.

The research was completed in two phases:

1. CFD Modeling and flume tank experiments of single and multiple turbine facsimiles in a straight channel;
2. A case study modeling single and multiple turbines in Minas Passage and Petit Passage.

Experiments were completed in the flume tank at the University of Victoria to measure thrust and study downstream wake dissipation for turbine arrays. Porous disc mounted on a force-measurement rig in the flume tank were used to represent the turbines. Particle image velocimetry (PIV) measurement equipment was used to visualize and quantify the wake structures behind the disks. The PIV system provided very rich flow-field data for a variety of array configurations clearly showing disc interactions and wake structure. Data from the experimental results was subsequently used to validate the turbine thrust and wake field computed using the CFD and Ocean models.

It was found that the CFD simulations did a reasonable job in predicting the thrust force acting on porous discs in several different array configurations. For all cases considered as part of this project, the thrust was predicted within 8% error of experimental results. The CFD simulations also did an adequate job predicting the wake recovery behind porous discs; however, significant tuning of turbulence parameters was required to get a good match to experimental data. The fact that thrust forces for each of the turbines can be predicted with reasonable accuracy and the wake can be tuned will allow site developers to use this simplified method for planning the initial layout of turbine arrays.

A team workshop was hosted by the University of Victoria on July 10th, 2012 to brainstorm CFD – Ocean model coupling approaches. Two cross-coupling methods were identified at the workshop:

i. Mid Field CFD model: 100s of meters or even few km in size (see Figure 1)
ii. Near Field CFD model: 10s of meters, only spanning one or few Ocean model elements around the turbine(s) (see Figure 2)

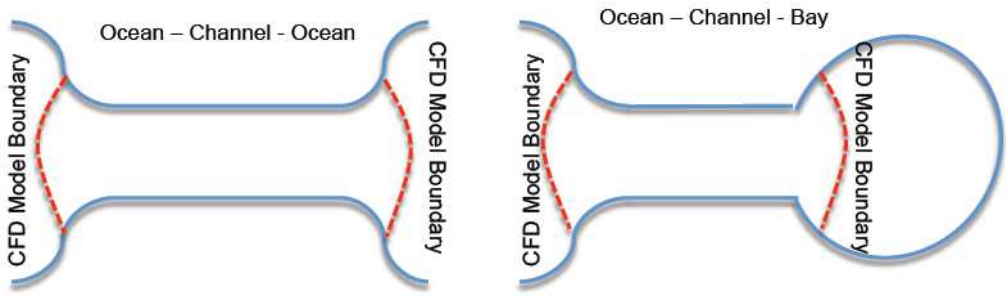

Figure 1: Mid Field CFD model approach

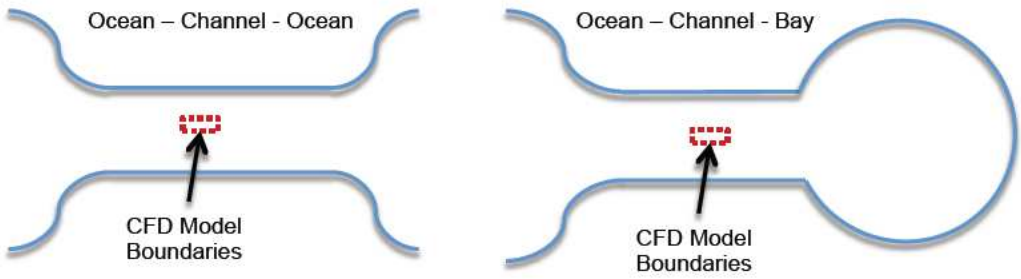

Figure 2: Near Field CFD model approach

One of the key objectives of this project was to apply these cross coupling methods to tidal sites in Nova Scotia. At the project outset, it was anticipated that all of the work would be applied to modeling the flows through Minas Passage with inclusion of 4 turbines at the test berths. As the project progressed, and the two different cross coupling approaches were identified, the team decided to include Petit Passage as a case study for testing the mid-field CFD approach while Minas Passage was used for testing the near-field approach.

The near field-modeling approach was tested on the Minas Passage site by modeling four 16m diameter turbines, one at each of the FORCE test berths. Each of the four turbines was first modeled in CFD (as a porous disk) in a 200m x 200m area surrounding each berth with inclusion of detailed bathymetry. Inflow and turbulence conditions were sourced from the Ocean model for the peak flood. To simplify the analysis only the M2 tidal component was used to drive the system. At peak flood (nominally U=2.5m/s) the total estimated power production in the Ocean model was 5MW.

The near-field coupling method work shows great promise. The objective was to ensure consistency between the Ocean and CFD models and in large part this was achieved. This methodology has a range of potential applications including:

- estimation of total extractable power from a tidal system;
- informing wide tidal site selection,
- array layout and channel build-out;
- investigation of the impact of a tidal installation on current patterns and tidal range;
- Investigation of the impacts of tidal installations on one another, etc.

With this methodology in place, regulators, developers and other stakeholders in the tidal industry can virtually investigate any number of ‘what if’ scenarios for the installations of free stream turbines before ever driving a pile or laying cable.

The mid-field cross-coupling method was also successfully implemented and demonstrated for Petit Passage. The flow through Petit Passage was modeled for both ebb and flood conditions (6 h each). In general results from the CFD simulations showed good agreement with Ocean model data, especially where the flow is relatively uni-directional and not dominated by large eddies.

A methodology was also proposed and subsequently demonstrated for how best to use the mid-field modeling approach to identify suitable turbine deployment locations. A deployment location along the north eastern shore was identified as a possible turbine deployment site. A simulation was subsequently run with the inclusion of a turbine. This simulation demonstrated the potential for using CFD to

calculate power extracted by the turbine over a tidal cycle as well as modeling the wake generated by the turbine. This methodology could therefore be extended to modeling tidal farm arrays with inclusion of turbine interaction effects.

At this point, the CFD model of Petit Passage is still considered preliminary because it has not been validated against field data. While ADCP measurements have been completed at several locations in Petit Passage, the data is not yet available for public release.

The team therefore succeeded in meeting initial project objectives by testing two separate methods of coupling CFD and Ocean models. Detailed models of both Minas Passage and Petit Passage now exist that can be used as tools by project developers for laying out turbine arrays and technology developers to better understanding local inflow conditions.

TABLE OF CONTENTS

LIST OF FIGURES

LIST OF TABLES

DETAILED TECHNICAL REPORT

A detailed report documenting the work completed as part of this project is provided in the following sections. Due to the highly specialized topic of this work, certain sections of the report are very technical in nature and therefore presume the reader is familiar with the fields of Ocean modeling, experimental testing and Computational Fluid Dynamics.

1 INTRODUCTION

This project aimed to develop a link between Ocean computer models and Computational Fluid Dynamics (CFD) models in order to improve state of the art modeling techniques used for resource assessments and tidal turbine siting for both single and multiple TISECs.

Ocean tidal models are the tool of choice when calculating tidal height and associated current velocity for large coastal areas spanning hundreds of kilometers over periods of days or even months. To achieve this by practical means without use of supercomputers, oceanographic models neglect some of the small scale physics, such as wake modeling and small scale turbulence that are extremely important to the performance of in-stream tidal devices.

Conversely, CFD models are much better suited at simulating small scale physics to capture interactions between turbines, but are very computationally expensive especially when individual turbine blades are modeled. Typically, CFD models simulate turbine performance in an idealized channel for a specific current speed and for short durations no more than a few minutes. CFD models therefore neglect the effects that energy extraction has on the overall tidal resource and fail to account for the complexity of a real world tidal flow that is continuously reshaped by the local topography.

Therefore, traditionally, Ocean models are used for assessing the magnitude of tidal resources in large areas such as the Bay of Fundy while CFD models are used by technology developers to predict turbine performance.

This project set out to draw from the strengths of both modeling approaches by developing methods of combining the ability of Ocean models to capture far field effects and CFD models to accurately predict the flow in very close proximity to the TISEC. Outcomes of this project will benefit both tidal turbine farm developers for site assessment as well as machine designers for better understanding local inflow conditions.

In order to successfully complete this project, a multifaceted team of researchers was assembled both from industry and academia with expertise in oceanographic modeling as well as experimental testing and CFD modeling of both horizontal and vertical axis turbines.

2 OBJECTIVES

This project aimed to develop a link between Oceanographic computer models and Computational Fluid Dynamics (CFD) models in order to improve state of the art modeling techniques used for tidal resource assessments as well as turbine-resource interactions for both single and multiple Tidal In Stream Energy Converters (TISECS). Tidal sites in Nova Scotia with anticipated turbine deployments were used as test cases.

Experimental testing, CFD simulations and Ocean modeling techniques were used to achieve the scientific objectives. The research was completed in two phases:

1. Modeling and flume tank experiments of single and multiple turbines in a straight channel;
2. A case study modeling single and multiple turbines in Minas Passage and Petit Passage.

The objective for the first phase of the work was to focus on generating high quality data and simulation results for the idealized case of single and multiple TISECS in a straight channel. Experiments in the flume tank at the University of Victoria were completed to study downstream wake dissipation and measure turbine thrust. Porous disc mounted on a force-measurement rig in the flume tank were used to represent the turbines. Particle image velocimetry (PIV) measurement equipment was used to visualize and quantify the wake structures behind the disks. Data from the experimental results was subsequently used to validate the turbine thrust and wake field computed using the CFD and Ocean model.

The first phase of the work therefore determined the strengths and limitations of both the CFD and Ocean models.

The objective of the second phase of the project was to apply cross coupling methods to tidal sites in Nova Scotia in order improve the state of the art of modeling tidal turbine and resource interactions. At the project outset, it was anticipated that all of the work would be applied to modeling the flows through Minas Passage with inclusion of 4 turbines at the test berths. As the project progressed, and new information became available, the team decided to also include Petit Passage as a case study for testing a mid-field CFD approach to cross-coupling. The objective of the mid-field approach was to push the boundaries in terms of model size by attempting to model part or even an entire tidal channel using CFD.

3 LAB SCALE TURBINE EXPERIMENTS

The first phase of the work focused on generating high quality data and simulation results for the idealized case of single and multiple TISECS in a straight channel. Experiments were conducted in the University of Victoria Fluids Research Lab. A picture of the water tunnel is shown in Figure 3-1. Experimental results provided data to validate the turbine thrust and wake field computed using the CFD and Ocean models. Several array configurations were tested in the flume tank. Particle image velocimetry (PIV) data were collected for a horizontal plane covering most of the tunnel test section. This provided a far richer data-set than would be feasible using other measurement techniques such as pitot tubes, hot-wires or ADCP.

Figure 3-1: Flume Tank at the University of Victoria

3.1 WATER TUNNEL

The water tunnel test section has a cross section of 45cm × 45cm and length of approximately 2.5m. The top of the test section can be open for tests involving a free surface (air-water surface), or can be closed using two acrylic lids. With the lids installed, the flow can be slightly pressurized, and the effects of free surface deformation are then no longer present. This was the chosen configuration for this study to avoid the additional computational expense and complexity of modeling a free surface. The walls of the test section are clear acrylic allowing optical access through the sides and bottom.

The flow is driven by a single-stage axial flow propeller pump delivering a maximum flow rate of 405L/s. The pump shaft RPM is controlled using Toshiba VT130H7U6270 frequency controller. The frequency setting is specified as a percentage of the max and the nominal frequency of 40% (corresponding to approximately 1.4 m/s in the test section) was used for most of the experiments presented here. The test section velocity can reach up to 2.0m/s; however it was found that in practice, speeds above 1.5m/s led to entrapped air-bubbles in the flow, which were detrimental to the collection of PIV data. The inflow to the test section is conditioned with a perforated plate, honeycomb section, 5 high-porosity screens and a 6:1 contraction. Downstream of the test section the flow is diverted by turning vanes in the return plenum into the return flow pipe located underneath the test section. The design turbulence level is approximately 1.0% however this was also assessed as part of the experimental campaign.

As part of this project, the water tunnel lids were modified to incorporate access hatches which allowed the porous disks to be mounted in a wide variety of configurations. The hatches were placed at three

preset distances away from the flume inlet. Additional mounts are also provided to secure the disks a varying distances away from the flume tank centerline. The depth of submergence can be easily adjusted by clamping the tubular mount at the desired location. The circular hatch seen in Figure 3-2 is for the physical rotor testing apparatus, so that combinations of porous discs and a spinning rotor can be tested together. The test rig therefore allows for testing a wide range of turbine configurations.

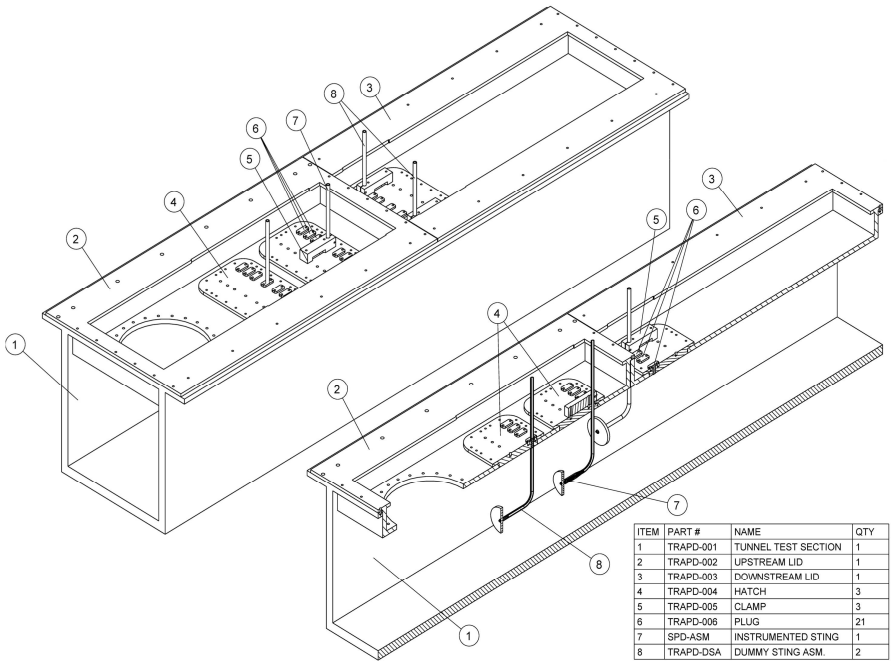

Figure 3-2: Water tunnel test section with lids installed. The three rectangular access hatches were added during this project to allow for many array configurations.

3.2 POROUS DISKS

The turbines were represented in the experiments by porous disks. These disks were designed to provide a specific resistance to the flow such that the total disc thrust force was representative of the thrust of an actual spinning rotor.

The porous disks were designed using the commercial CAD tool ProE and fabricated using a fused deposition modeler (FDM). This is essentially a 3D printer that builds-up the model geometry in layers. In the early stages of the project, several disks were created with varying porosity. These were tested to determine the relationship between the disk drag coefficient and porosity. It was determined that a porosity of 50% gave a drag coefficient of approximately 0.9, which is similar to that of a turbine operating at its maximum efficiency. Thus 50% porosity disks were used for all of the experiments presented in this study. Discs were fabricated with diameters of 10cm and a regularly spaced grid of square pores. A sample disk is shown in Figure 3-3.

It is important to note that porous disks are only similes of actual turbines. Their primary similarity is that both turbines and discs extract energy (momentum) from the flow. Of course, the flow phenomenon is different in both cases; for turbines, a combination of lift (pressure) and drag (viscous) forces are created locally by the blades, whereas the discs create the pressure drop through the disc

through viscous losses and associated downstream small-scale turbulence only. Flow phenomenon such as swirl and discrete vortex sheets shed from the blades are also neglected when using porous disks. In sum, the overall pressure drop and momentum change experienced by the flow passing through an actual rotor or porous disc is similar, but the physical mechanism is different.

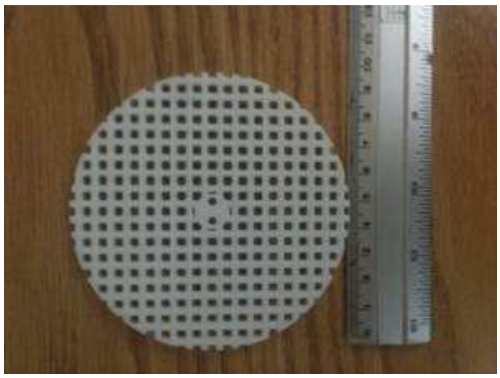

Figure 3-3: 10 cm dia. porous disk printed using FDM machine

3.3 FORCE MEASUREMENT

It was necessary to mount the porous discs in the tunnel and to measure the thrust force. Two conceptual designs were assessed early-on in the project for achieving these goals. The first involved measuring the force with a load cell and a lever arm. That design would have measured the drag of both the porous disk and the sting holding it in place. This would have led to increased uncertainty in the force readings because it would not measure the disc drag directly. The solution was to house a load cell in a watertight enclosure which connected the disk to the mounting sting. The design is shown in Figure 3-4.

This setup allowed the disk drag to be measured directly. The chosen load cell was the Omega LCMKD-20N, rated to a maximum load of 20N. The expected forces in the experimental campaign were approximately 10N. The sensor was chosen to provide a good signal-to-noise ratio, and to be as unobtrusive to the flow as possible. The load cell had a diameter of 0.5in = 1.27cm. The housing was made to have the smallest diameter feasible, which ended-up being 0.75in = 1.905cm. While this may seem large compared to the disk diameter of 10cm, the cross sectional area of the sensor housing was only 3.6% of the disc area. This was considered acceptable.

The manufacturer's calibration for the load cell was no longer applicable due to some frictional effects present in the housing seals, so a detailed calibration was conducted for the in-situ load cell. The sting was oriented vertically and known masses were loaded onto the porous disk, during which time the sensor output was recorded. Plotting the sensor output vs. load provided a calibration curve shown in figure 3. The calibration tests were repeated three times to assess the repeatability. Some minor hysteresis was observed, but there was good consistency between the three tests. The uncertainty from sensor repeatability was estimated using standard statistical techniques and is given in Table 3-1.

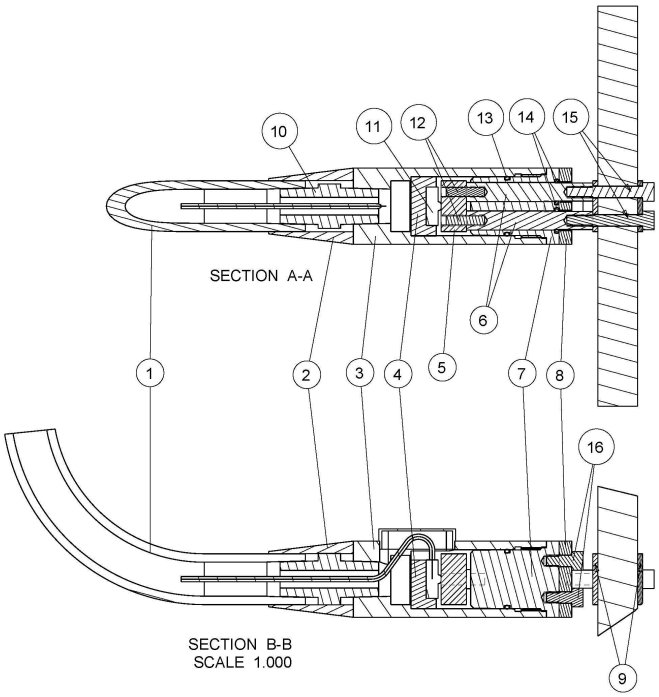

ITEM	PART #	NAME	QTY
1	SPD001	PILON	1
2	SPD002	REDUCER FITTING	1
3	SPD003	HOUSING	1
4	SPD004	CELL HOLDER	1
5	SPD005	PUSHER PLATE	1
6	SPD006	SLIDER ROD	2
7	SPD007	SLIDER BUSHING	1
8	SPD008	END PLATE	1
9	TRAPD012	WASHER PLATE	2
17	SPD009	CONDUIT	1
10	51205K471	1/8 NPT NIPPLE	1
11	LCMKD-20N	LOAD CELL	1
12	-	CUT-OFF 4-40 SCREW	2
13	9262K614	1X13 METRIC O-RING	1
14	9262K611	1X4.5 METRIC O-RING	2
15	92185A112	4-40X3/4 SCREW	2
16	92185A106	4-40X1/4 SCREW	2

Figure 3-4: Detail of the load cell housing

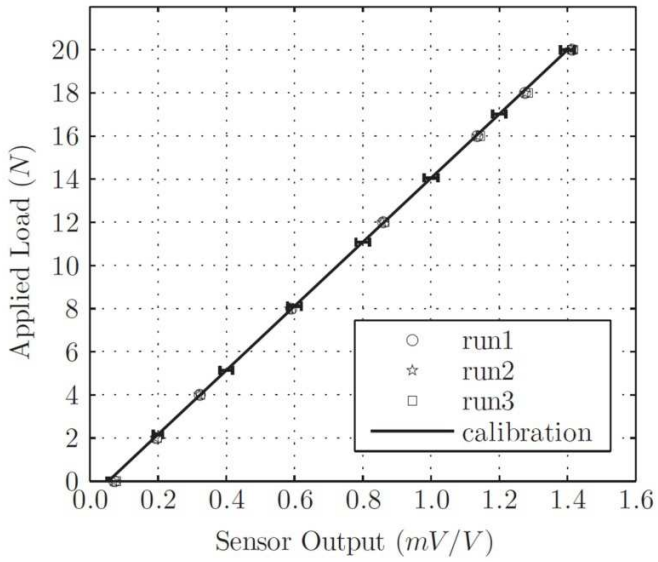

Figure 3-5: Sensor Calibration Curve

Table 3-1: Sensor uncertainty determined from calibration tests

Sensor output $\left(\frac{mV}{V}\right)$	**Uncertainty** $\left(\frac{mV}{V}\right)$
0.0759	0.0056
0.2030	0.0134
0.3340	0.0182
0.6010	0.0201
1.6000	0.0201

3.4 RAIL SYSTEM

Since PIV data were required along the entire tunnel length and width, it was necessary to move the camera many times to obtain a full flow field for each test case. This would not have been feasible with the existing camera mounting system in place in the lab, so a set of rails (visible in Figure 3-6) were installed to allow the camera to be placed at any horizontal position easily. The rails ensured that the camera was always at the same height. Similarly the laser was mounted on rails to allow translation in the x direction. Great care was taken to ensure that all of the rails were perfectly level so that the laser sheet would always be at the same height. With this system in place, images could be taken at all of the required horizontal locations without having to re-focus the camera or adjust the laser.

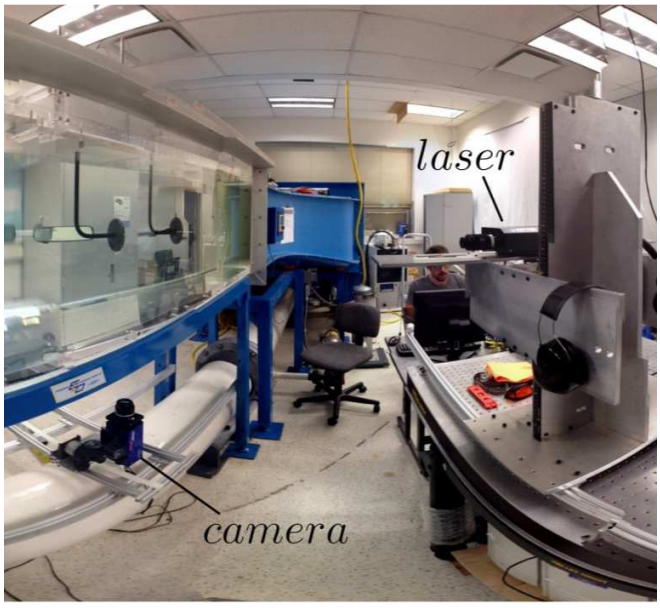

Figure 3-6: Experimental setup. The camera and laser were mounted on rails to facilitate efficient collection of PIV data over the entire test section width and length.

3.5 ARRAY CONFIGURATIONS

At the beginning of the project, a large number of different array configurations were defined. During the experimental campaign, it was realized that a subset of the original planned configurations would suffice. The final set of disk configurations is summarized in Table 3-2. The parameter Δx/D refers to the streamwise separation between two disks (in terms of disk diameters), while Δz /D refers to the lateral (side by side) spacing between disks. A more detailed visual description of each test set is

provided in Table 3-3. The tests have been selected to first determine baseline resistance coefficients for the various disc porosities, before investigating the discs in various configurations. Note that disc porosity determined the resistance coefficient, which as a non-dimensional quantity did not vary with test condition and was an input to the analysis codes.

Table 3-2: Summary of porous disc array configurations

Set	Description	Case	# disks	Δx/D	Δz/D	f
1	test Re dependence	a	1			25
		b	1			35
		c	1			40
		d	1			45
3	two disks in tandem	a	2	3	0	40
4	two disks side-by-side	a	2	0	0.10	40
		b	2	0	0.80	40
6	three disks side-by-side	a	3	0	0.25	40
7	three disks staggered	b	3	3	0.25	40

Table 3-3: Description of experimental tests

Test	Description
Set 1	Impact of inflow speed on disk thrust and wake characteristics Velocity sweep: 0.5m/s to 1.8 m/s, Dia.=10cm, $C_T \approx 0.9$ 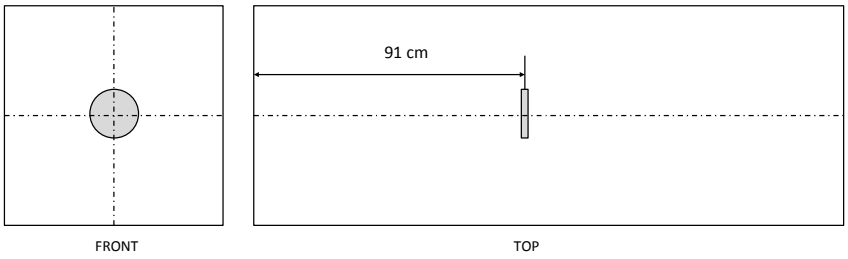
Set 3	Two disks aligned streamwise, Dia.=10cm, $C_T \approx 0.9$, Δx=30cm, U≈1.5m/s 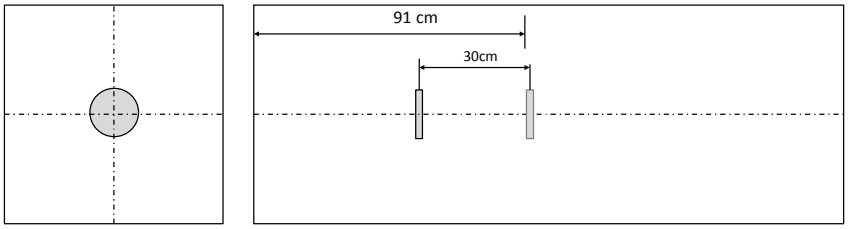
Set 4	Two Disks aligned transverse: Dia.=10cm, $C_T \approx 0.9$, $\Delta y = \{1,8\}$cm, U ≈1.4 m/s 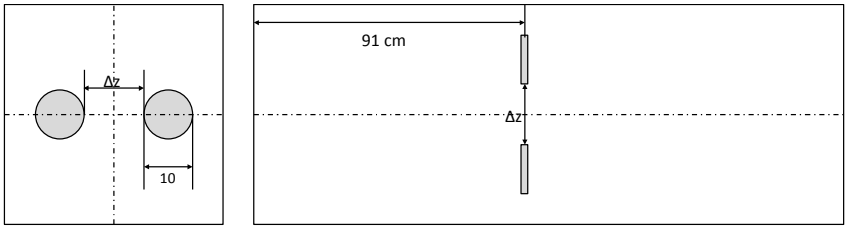
Set 6	3 disks aligned transverse, Dia. = 10 cm, C_T= 0.9 (approx.), Δz =2.5 cm 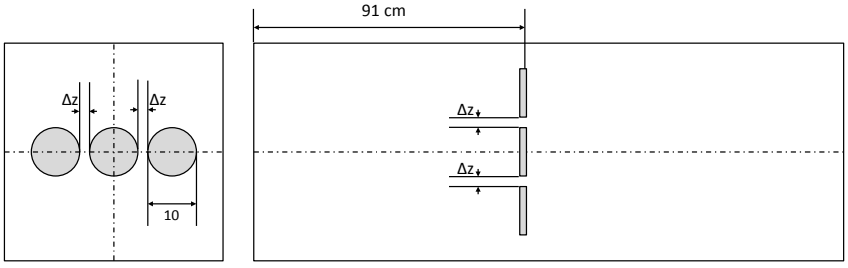
Set7b	Impact of Staggered Spacing 3 disks: Dia.=10cm, $C_T \approx 0.9$, Δz=2.5cm, Δx=30 cm 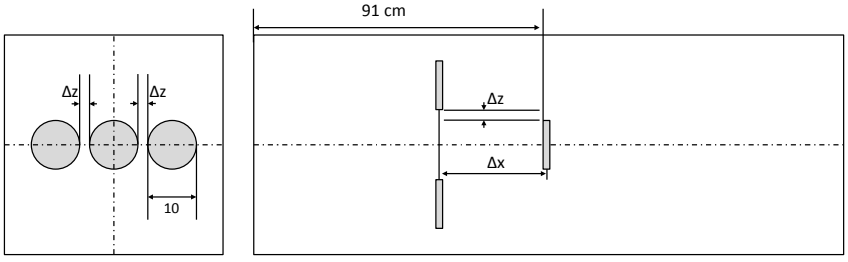

3.6 PIV SETUP

The camera was mounted on the carriage assembly on the rails under the water tunnel test section, while the laser was positioned on a second set of rails mounted on an optics table beside the tunnel test section as shown in Figure 3-6. The camera used was the *LA-Vision VC-Imager Intense*. A lens with a focal length of 14mm was used to capture fairly wide angle images to reduce the total number of camera positions required for each test case. The largest aperture setting (*f-stop*=1.4) was used to capture the most light possible, allowing a relatively low power setting to be used for the laser (typically 40%). The laser model was a *New Wave Research SOLO PIV* (class IV) operating at a wavelength of 532nm with a maximum energy per-pulse of 100mJ and pulse duration of 6ns.

Images were taken in a double-pulse double-exposure mode. In this mode, the laser is fired a first time while the camera records the first frame, then after a user-defined time delay, the laser fires a second time and the camera takes a second frame. The vector fields are then calculated using a cross correlation analysis of the two recorded frames. The time delay is set depending on the flow velocity and size of the interrogation window size (interrogation windows are described in the next section) and can be fine tuned to provide an optimal particle displacement from the first frame to the second. Most of the experiments were at a flow speed of approximately 1.4m/s, and the time delay was typically 700µs. The system was operated at a data collection rate of 5Hz, meaning that two frames (to produce a single vector field) were collected each 0.2s. For each experiment, images were taken with the camera in many different positions to capture the flow field in a plane spanning most of the test section. For each camera position, 150 image pairs were taken to ensure an acceptable level of uncertainty in the calculated mean velocity field. (See section 3.8 for details on how the uncertainty was assessed). Once the time-averaged flow fields were obtained for each camera location, they were stitched together to create a single continuous vector field spanning the entire measurement plane.

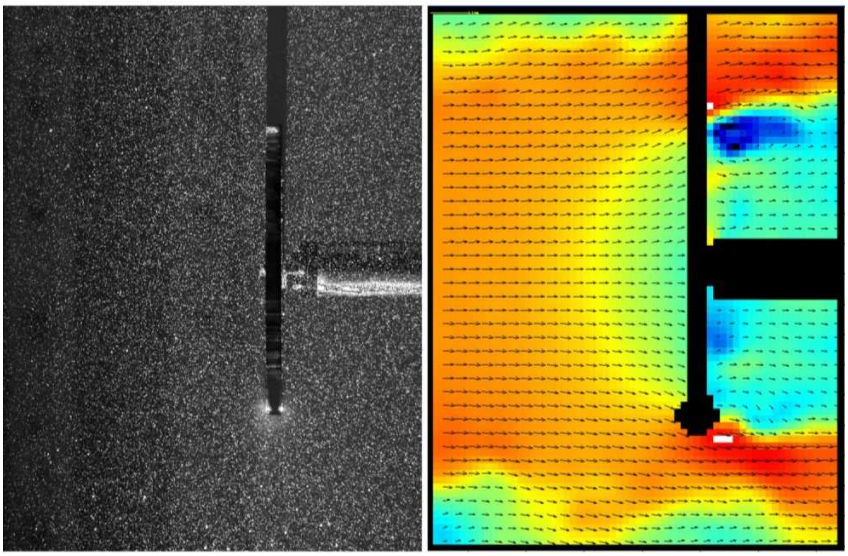

Figure 3-7: Sample PIV image and computed vector field for the downstream disc in case 7b.

3.7 PIV PROCESSING: OBTAINING INSTANTANEOUS VECTOR FIELDS

The PIV data were processed using the commercial software *Davis v7.2*. A sample raw image and the resulting velocity field are shown in Figure 3-7. This section describes the general methodology for obtaining vector fields from PIV data. A more detailed description of the specific software options applied is provided in Appendix A.

The PIV method splits-up each image into a set of interrogation windows. For every window in the first frame, there is a corresponding window in the second frame. The method computes the cross-correlation function between the image intensities in the corresponding interrogation windows from the first and second frames. The cross correlation is defined by;

$$C(dx,dy)\sum_{x=0,y=0}^{x<n,y<n} I_1(x,y)I_2(x+dx,y+dy),\quad dx<\frac{n}{2},dy<\frac{n}{2} \qquad \textbf{(1)}$$

where x and y are coordinates with their origin at the bottom left of the interrogation window. I_1 and I_2 are the image intensities (brightness) in the first and second interrogation windows. The second interrogation window is often shifted by a distance corresponding to the estimated velocity. Provided the window shift corresponds to the true velocity the peak correlation should occur at dx=dy=0. Without shifting the second interrogation window, it is impossible to calculate velocities corresponding to a particle displacement larger than ½ of the interrogation window length.

The methodology employed during this study was to first calculate a coarse resolution vector field with large interrogation windows. Then that field was used to shift the interrogation windows for the next iteration, which used smaller windows, providing better resolution. This process of refining the vector field resolution was repeated several times.

3.8 PIV POST-PROCESS: OBTAINING A TIME-AVERAGED VELOCITY FIELD

The goal of the experimental campaign was to obtain time-averaged velocity fields for comparison to steady-state CFD simulations. During the data collection campaign, an analysis was done to determine the number of instantaneous vector fields required to obtain a statistically converged mean velocity field. The time-averaged velocity $\overline{u}_x(x,y)$was found using:

$$\overline{u}_x(x,y)=\frac{1}{N_t}\sum_{i-1}^{N_t}u_x(x,y,t_i) \qquad \textbf{(2)}$$

The uncertainty in the mean was found for a 95% confidence interval using:

$$U_{\overline{u}_x}(x,y)=1.96\sqrt{\sum_{i=1}^{N_t}\frac{[\overline{u}_x(x,y)-u_x(x,y,t_i)]^2}{N_t}} \qquad \textbf{(3)}$$

This gave an uncertainty field which varied spatially. The spatial rms of the uncertainty was evaluated using;

$$\mathrm{rms}\left(U_{\overline{u}_x}\right) = \sqrt{\frac{1}{N_{xy}}\sum_{i=1}^{N_{xy}}\left[U_{\overline{u}_x}(x_i, y_i)\right]^2} \qquad (4)$$

The rms and maximum uncertainty were then plotted against number of time samples (N_t) for each camera position. The desired level of uncertainty was < 2% for the rms, and < 5% for the max. These goals were met using less than 150 samples in all camera locations except for right at the porous disk, where the highly varying velocity field resulted in higher uncertainties. Figure 7 shows how the rms and max uncertainty converged with increasing number of samples for case 7b at the downstream disk location. Figure 8 shows the spatial variation of the uncertainty with 150 samples for the 7b case. Note that the uncertainty is well below 5% except for a few locations just downstream of the porous disk.

The vector fields from all different camera locations were then stitched together using linear interpolation in overlapping regions. For each test case, the inflow velocity U_0 was determined by taking the spatial average of the time-averaged velocity over the entire camera frame for the most upstream camera position recorded. This inflow velocity was later used as a boundary condition for the CFD simulations.

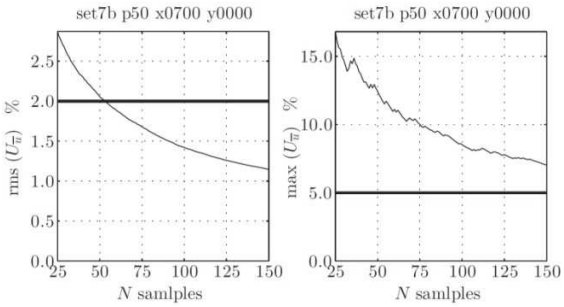

Figure 3-8: Convergence of the uncertainty in the time-averaged velocity with increasing number of samples for case 7b at the downstream disk location

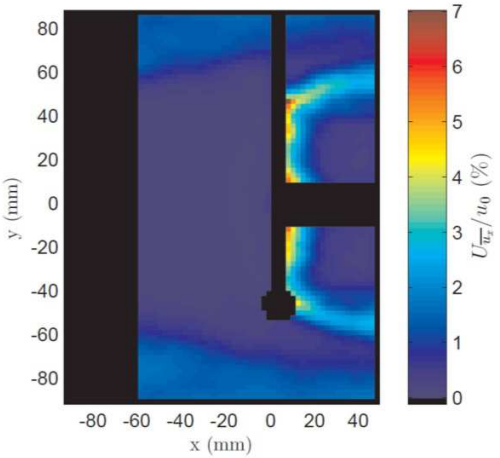

Figure 3-9: Spatial variation of the uncertainty in the time-averaged velocity for case 7b at the downstream disk location using 150 samples. The black region is where a mask has been applied (no vectors have been calculated)

3.9 TURBULENCE ANALYSIS

The wake recovery behind porous disks is sensitive to the level of turbulence present in the flow. Thus it was required to evaluate some fundamental characteristics of the turbulence present in the experimental runs. The CFD simulations used a two-equation turbulence model which solves transport equations for the turbulent kinetic energy k and the dissipation rate ϵ. These quantities must be set at the inlet to the CFD simulation, but often the turbulence intensity I and length scale L_ϵ are defined by the user, and k and ϵ are calculated using:

$$k = \frac{3}{2} I^2 U_0^2 \tag{5}$$

$$\epsilon = \frac{k^{\frac{3}{2}}}{L_\epsilon} \tag{6}$$

3.9.1 Turbulent Kinetic Energy

The turbulent kinetic energy was obtained from PIV data using its definition;

$$k = \frac{1}{2}\left(\overline{u_x'^2} + \overline{u_y'^2} + \overline{u_z'^2}\right) \tag{7}$$

Because 2D PIV data were collected, the vertical (z) velocity component was not available, so it was assumed that $\overline{u_z} = \overline{u_y}$. This is likely a good assumption given the symmetric geometry of the test section. The values of the fluctuating velocity components u_x and u_y were obtained in the following manner. The PIV data from the most upstream camera position were used. The camera field of view at this location covered a region from 400mm to 250mm upstream of the upstream disc position. The time-averaged velocity field was first obtained by taking the average of 150 samples in time. Then, the fluctuating velocity components were found by subtracting the time-average from the original instantaneous velocities. The turbulent kinetic energy was then found using:

$$k = \frac{1}{2}\overline{u_x'^2} + \overline{u_y'^2} \tag{8}$$

The uncertainty in each fluctuating velocity component depends on the number of independent samples N_s. For samples to be independent they must be separated by twice the length scale of the dominant eddies (the integral length scale), and also they must be separated in time by twice the time-scale of the dominant eddies [1]. The number of spatially independent samples was defined based on the estimated integral length scale (defined later) and the size of the camera capture area. With an estimated length scale of 25mm, only nine sampling locations in the vector field could be considered independent. However, all samples in time were independent due to the relatively slow collection rate (5Hz) of the PIV system. This gave a total of $N_s = 1350$ independent samples for the fluctuating velocity components. The uncertainty in the fluctuating velocity components was found using the method described in Benedict and Gould [2].

$$U_{\overline{u_i'^2}} = 1.96\left\{\frac{1}{N_s}\left[\overline{u_i'^4} - \left(\overline{u_i'^2}\right)^2\right]\right\}^{\frac{1}{2}} \quad \text{for } i = \{x, y\} \tag{9}$$

The uncertainty in the turbulent kinetic energy was then defined using typical techniques for uncertainty propagation.

$$U_k = \sqrt{\left(\frac{1}{2}\right)^2 \left(U_{\overline{u_x'^2}}\right)^2 + \left(U_{\overline{u_y'^2}}\right)^2} \tag{10}$$

The turbulent kinetic energy was typically around $k \approx 2.0 \times 10^{-4}$ with an uncertainty of approximately 10%. This uncertainty could be improved by taking more samples in time. This gave a turbulence intensity *I* of approximately 0.8%.

3.9.2 Turbulent energy dissipation

The dissipation rate is much more complicated to determine than the turbulent kinetic energy. Typical methods involve determining spatial gradients in the turbulent energy using finite differencing techniques, and require very precise data at a very high resolution. For example, Tanaka and Eaton [3] have developed a correction method for reducing the effect of senor noise on the calculated dissipation rate which requires a spatial resolution between 1/10 and 1/2 of the Kolmogorov microscale, (typically on the order of 200µm). Such resolution was not possible with the current camera system at UVIC.

For these experiments, the dissipation rate was estimated using an alternate approach which relies on the universal similarity of turbulent energy spectra in the inertial subrange. In the inertial subrange, energy is transferred from larger eddies to smaller ones at a rate equal to the dissipation rate ϵ. In this range the effects of viscosity are negligible and dimensional analysis yields Kolmogorov's famous $K^{-5/3}$ law:

$$E(K) = C\epsilon^{\frac{2}{3}}K^{-\frac{5}{3}} \tag{11}$$

Where C is a constant, typically $C = 5.$ K is the wave-number, and E is the turbulent kinetic energy present at a specific wave number. The expression for the power spectrum can be non-dimensionalized using the Kolmogorov length scale $= (\nu^3/\epsilon)^{1/4}$:

$$\frac{E(K)}{(\epsilon\nu^5)^{\frac{1}{4}}} = C(K\eta)^{-\frac{5}{3}} \tag{12}$$

Now, the above equation represents a 3D energy spectrum. Using 2D PIV data it was not possible to define the 3D energy spectrum as defined above. However, it was possible to define 1D spectra along the x direction for both x and y velocity components using standard fast-Fourier-transform (FFT) techniques. The theoretical solution for these 1D energy spectra $E_{11}(K_1)$ and $E_{22}(K_2)$ are given for isotropic turbulence by:

$$E_{11}(K_1) = \frac{18}{55}E(K) \tag{13}$$

$$E_{22}(K_2) = \frac{22}{55}E(K) \quad \textbf{(14)}$$

When non-dimensionalized, these 1D spectra are universal for all flows if isotropy can be assumed. Thus, assuming the experimental turbulence is isotropic; the spectra obtained from the PIV data must adhere to these analytical solutions. This assumption was used in a method whereby an assumed integral length scale was tuned until the energy spectra obtained from the PIV data matched the known solutions in the inertial subrange. This approach is further discussed in Appendix B. The results of the method are summarized in Table 3-4 .

Table 3-4: Summary of the inlet turbulence analysis results for case7a

Parameter	**value**	**units**
Turbulent kinetic energy	$k = 1.9 \times 10^{-4}$	m^2/s^2
Integral length scale	$L_\epsilon = 25$	mm
Dissipation rate	$\epsilon = 1.0 \times 10^{-4}$	m^2/s^3
Kolmogorov scale	$\eta = 310$	μm

3.10 Reynolds Independence and Consistency Between Discs

There were two goals of the set1 experiments. The first was to evaluate the Reynolds dependence of porous disks, and the second was to compare the drag force of the three porous disks (of the same design) used in the experiments. The drag force determined from the sensor readings, and the computed thrust coefficient C_T are shown for a variety of water tunnel inflow speeds (U_0) in Figure 3-10. Based on these results, it was decided that the disks behaved similarly enough to be considered equivalent. This justified using symmetry planes in the CFD simulations, which reduced computational expense. The plot of C_T may seem to imply a slight upward trend with increasing U_0, however this was within the experimental repeatability, and it has been assumed that C_T is invariant with Reynolds number. A more detailed study with a larger range of Reynolds numbers and highly repeatable results would be required to fully assess the Reynolds independence of porous disk C_T and wake characteristics.

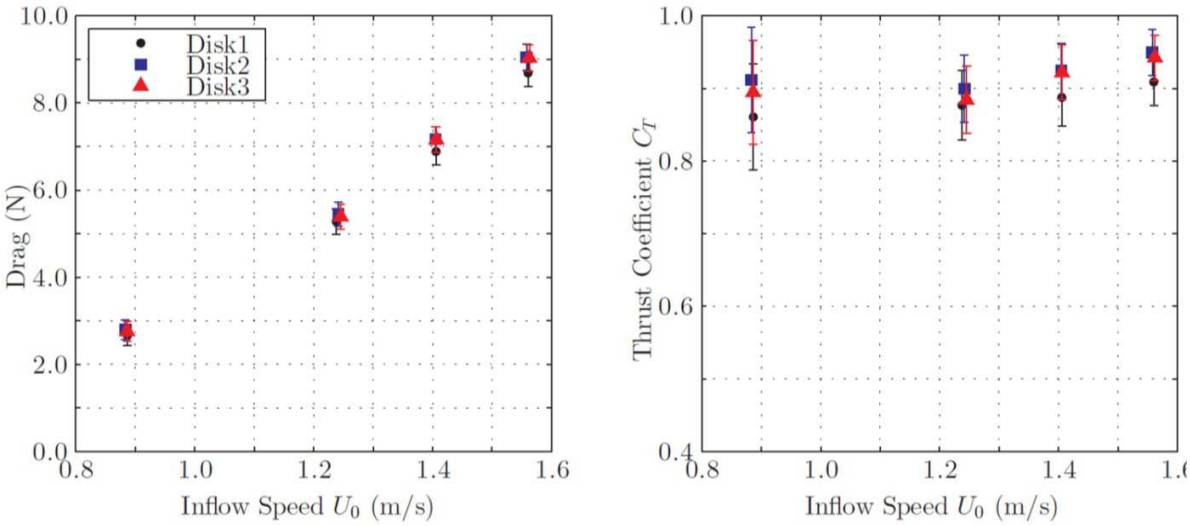

Figure 3-10: Disc drag force (left) and thrust coefficient (right) for three different discs and a variety of inflow speeds

3.11 SHED VORTICES

The PIV data in the immediate wake was quite chaotic, and contained large scale turbulent eddies of diameter up to approximately 1/3 of the disc diameter. These flow structures remained relatively coherent for several diameters behind the discs before becoming totally chaotic. An example plot is given in Figure 3-11 showing a streak of eddies shed from the disc edges. The black region is where the vector field has been masked out due to the sting in the image background. The color of the plot corresponds to vorticity and the vectors show the velocity relative to the spatially averaged velocity. Large vortical structures are evident in the wake.

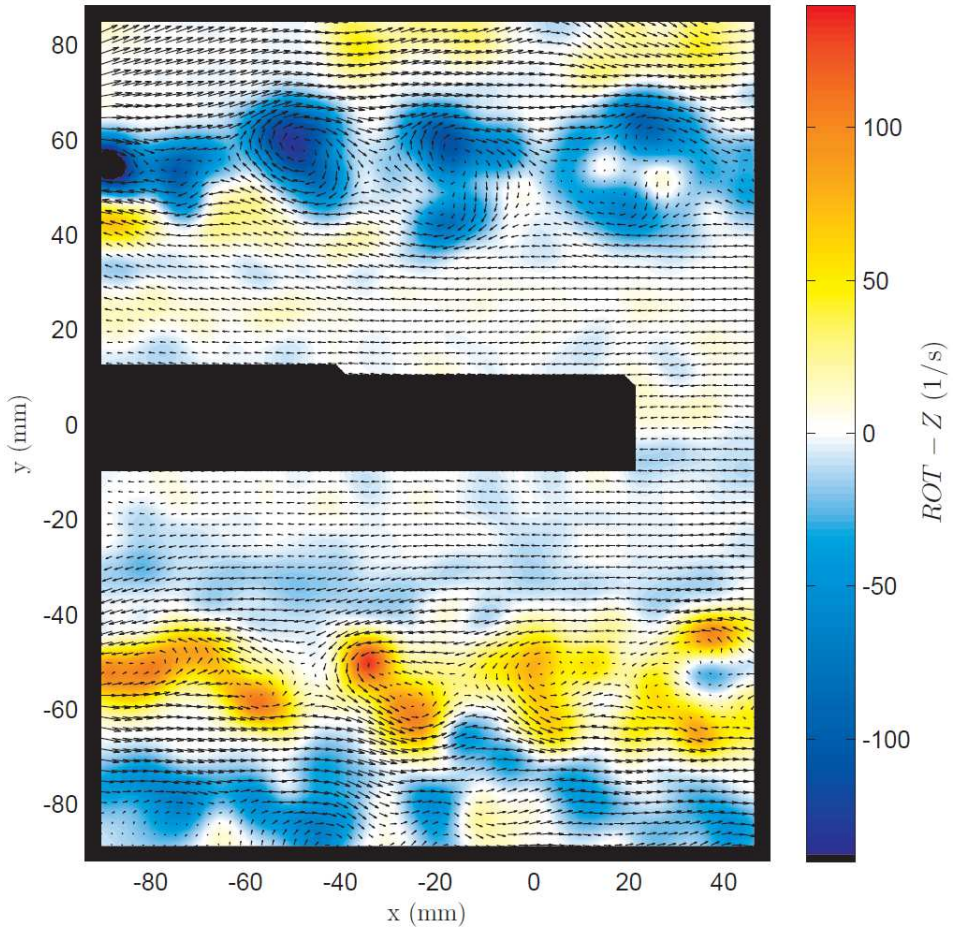

Figure 3-11: Large vortical structures shed from the disc edges were evident in the experimental flows.

3.12 Summary of Force and Inflow Velocities

The inflow velocity, disc force and thrust coefficient are summarized for all of the experimental cases in Table 3-5. The uncertainty in the disc force was determined using the values from Table 3-1. The thrust coefficient was calculated using;

$$C_T = \frac{D_{exp}}{\frac{1}{2}\rho U_0^2 A_d} \qquad \textbf{(15)}$$

where D_{exp} is the experimental disc force, and A_d is the cross sectional area of the porous disc. The thrust coefficient uncertainty was determined using typical error propagation techniques for the force uncertainty.

Table 3-5: Summary of disc force and inflow velocity

Config.	Inst. disc position	U_0 (m/s)	disc force (N)	C_T
1a	Center	0.8965	2.65 ± 0.22	0.836 ± 0.069
1c	Center	1.4251	6.88 ± 0.30	0.863 ± 0.037
3a	Upstream	1.4079	6.96 ± 0.33	0.897 ± 0.042
3a	Downstream	1.4055	1.86 ± 0.19	0.238 ± 0.024
4a	Left	1.4081	7.67 ± 0.34	0.985 ± 0.043
4b	Left	1.4016	7.40 ± 0.33	0.959 ± 0.043
6a	Center	1.4145	7.77 ± 0.32	0.989 ± 0.040
6a	Side	1.4178	7.82 ± 0.33	0.991 ± 0.042
7b	Front	1.3957	7.24 ± 0.37	0.946 ± 0.048
7b	back	1.3983	7.78 ± 0.31	1.013 ± 0.040

4 CFD MODELING OF FLUME TANK EXPERIMENTS

Mavi and UVic both created CFD models to replicate flume tank experiments. This chapter contains a general description of the CFD methods used, as well as documentation of several studies conducted by UVic and Mavi.

4.1 SIMULATION SOFTWARE

UVic and Mavi used different CFD software packages throughout this study. This was done to assess whether the simulation results were software-dependent and to provide a means to implement slightly different approaches to the CFD modeling that would have been difficult to implement in just one of the two software packages employed.

4.1.1 UVic CFD Software

UVic used the general purpose CFD solver ANSYS CFX for all simulations. CFX uses a finite volume Navier-Stokes solver formulated in primitive variables. The advection scheme chosen for all simulations was the high resolution option, which is a blend between the 2nd order accurate central-difference-scheme (CDS) and the 1st order accurate upwind scheme, where the blend factor is determined throughout the simulation and favors the CDS scheme except in situations where the stability of the solution may be compromised. CFX uses a co-located grid and avoids even-odd decoupling with a modified Rhie/Chow interpolation. The software uses a fully implicit discretization and a coupled solver which uses an incomplete lower upper (ILU) factorization technique. This is an iterative solver that approaches the exact solution to the discretized equations over the course of many iterations. This approach allows the specification of a timestep for steady state simulations; however this term serves only to under-relax the governing equations. The solver is accelerated using an algebraic multi-grid technique called additive correction.

4.1.2 Mavi CFD Software

Mavi used the general purpose CFD solver STAR-CCM+ for all simulations. Similar to ANSYS CFX, STAR-CCM+ uses a finite volume Navier-Stokes solver. The convection scheme used is a 2nd order accurate upwind scheme. The solver uses Rhie/Chow type pressure velocity coupling combined with a SIMPLE type algorithm.

4.2 GOVERNING EQUATIONS

Both analysis codes solved the Reynolds-Averaged Navier Stokes (RANS) equations for all simulations. The flow was assumed to be incompressible and all lab-scale simulations sought steady state solutions. The simulations in this paper neglected thermal effects, allowing the energy equation to be neglected. Thus, the dissipation of turbulent kinetic energy did not contribute to heat production, nor did viscous shear. The impact of heat production is negligible because as demonstrated by Corten [4], the heat produced by a turbine is insufficient to cause a noticeable temperature increase in the downstream flow. For steady, incompressible flows, the RANS equations can be expressed in a compact form using Einstein notation:

$$\frac{\partial \overline{u_i}}{\partial x_j} = 0 \qquad \textbf{(16)}$$

$$\overline{u}_j \frac{\partial \overline{u_i}}{\partial x_j} = \frac{\partial}{\partial x_j}\left[-\frac{\overline{p}\delta_e}{\rho} + \nu \frac{\partial \overline{u_e}}{\partial x_j} - \overline{u_i' u_j'}\right] + \frac{\overline{\Phi_i}}{\rho} \qquad \textbf{(17)}$$

where $\delta_{ij} = 1$ for $i = j$ and equals zero otherwise. $\overline{S_i}$ is a time-averaged momentum source, used to impose the porous disc forces on the flow.

4.2.1 Turbulence Closure

The Reynolds averaging process introduces additional stress terms (Reynolds stresses) into the instantaneous Navier-Stokes equations, as documented in numerous CFD text such as Versteeg and Malalasekera [5]. The Reynolds stresses are modeled using a turbulence model and several options exist. In all simulations presented here, the k-ω SST model by Menter [6] was used due to its well documented [6] [7] [8] [9] performance.

The SST model is as a combination of the standard k-ϵ and Willcox k-ω models, taking advantage of their mutual strengths. Namely, the k-ϵ model performs well for free shear flows, while the k-ω model works well in the viscous sub-layer. The SST model uses a blending function to implement the k-ω model near no-slip boundaries, and a re-formulated version of the k-ϵ model outside of the boundary layer. Since many of the flows presented in this report did not employ no-slip boundaries, the SST model is equivalent to the standard k-ϵ for these cases. The turbulence model transport equations were solved using the first order upwind scheme.

4.3 Specifying Porous Disk Forces

Two differing approaches were taken for setting the porous disk forces in the simulations.

UVic employed a method for setting the disc force so as to match the experimental drag for every test case. This was useful for assessing the differences between the experimental and simulated wakes with the exact same disk force applied to both flows.

Mavi, on the other hand used a methodology where the disk resistance coefficient was always constant. This allowed an assessment of the ability of CFD to predict the influence of different array configurations on the disc force.

4.3.1 Method 1: Predetermined Disk Force

In the simulations by UVic, the disk forces were set to match the experimental results. The disc forces were imposed on the domain through the momentum source term $\overline{\Phi_{i\,Uvic}}$. The momentum source term defines the pressure drop through the porous region for a given thickness. The momentum source terms at each disk were specified using a directional loss model using linear (viscous term) and quadratic (inertial term) resistance coefficients $K_{v\,Uvic}$ and $K_{i\,Uvic}$. The model requires defining a streamwise direction (x^s), and different resistance coefficients may be specified for the streamwise (superscript s) and transverse (superscript t) directions.

$$\overline{\Phi_{x^s\,Uvic}} = -K^s_{v\,Uvic}\overline{u_{x^s}} - K^s_{i\,Uvic}|\overline{u}|\overline{u_{x^s}} \quad \textbf{(18)}$$

$$\overline{\Phi_{(y^t,z^t)\,Uvic}} = -K^t_{v\,Uvic}\overline{u_{(y^t,z^t)}} - K^s_{i\,Uvic}|\overline{u}|\overline{u_{(y^t,z^t)}} \quad \textbf{(19)}$$

In this project, only the streamwise quadratic resistance term $K^s_{i\,Uvic}$ was used and all other resistance coefficients were set to zero. For setting the simulation disc force to match that of the experiment, the following formulation was employed.

$$K^s_{i\,Uvic} = \frac{D_{exp}}{\int_{\mathcal{V}} |\overline{u}|\overline{u_{x^s}} d\mathcal{V}} \quad \textbf{(20)}$$

where D_{exp} was the disc drag force measured during experiments, and the integral term was evaluated over all finite volumes inside the porous disk region. Specifying the force in this manner ensured that the total drag acting on the disc was equal to the experimental value, but also allowed the distribution of drag to vary spatially over the disk. Such spatial variation is important for flows with non-uniform flow approaching the disk, which is likely in arrays of turbines.

4.3.2 Method 2: Fixed Disk Parameters

In the simulations by Mavi, the porous disk resistance coefficients were set to constant values, which were determined by tuning the values until the CFD disc force matched the experimental force for the single disk experiments. In STAR-CCM+, the pressure drop over a given thickness of the porous region can be defined as

$$\overline{\Phi_{x^s\,Mavi}} = K^s_{v\,Mavi}\overline{u_{x^s}} + K^s_{i\,Mavi}|\overline{u_x}|\overline{u_{x^s}} \quad (21)$$

where $\overline{\Phi_{x^s Mavi}}$ is pressure drop over the porous region thickness, $K^s_{v\,Mavi}$ and $K^s_{i\,Mavi}$ are the viscous and inertial resistance coefficients respectively, and $u_{x^s}$is the velocity through the porous region. The calibrated porous disk resistant coefficient values were based on the results of single disk experiments, conducted by UVic, run at two inlet velocities. The single disk experiments were run at multiple inlet velocities, however; only experiments at two inlet velocities were able to record reliable force measurements. Table 4-1 shows the average results for each inlet velocity.

Table 4-1: Single Disk in Flume Tank Experimental Results

Set	U_0 (m/s)	Thrust (N)
1a	0.8965	2.65
1c	1.4251	6.88

Based on the disk dimensions and the recorded disk force, the $\overline{\Phi_{x^s Mavi}}$ at each U_0 can be calculated from the experiments.

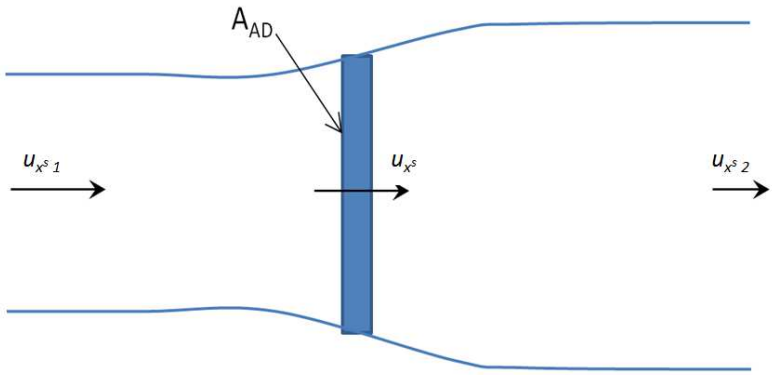

Figure 4-1: Stream-tube analysis of actuator disk.

The velocity through the disk, u_{x^s}, was not measured directly in the experiments and therefore must be estimated. An idealized stream-tube analysis of an actuator disk can be used to estimate the flow velocity through the porous disk. Figure 4-1 shows a diagram of a stream-tube through an actuator disk. From the stream-tube analysis, the drag force,D, on the actuator disk can be calculated as:

$$D = \rho A u_{x^s}(u_{x^s 1} - u_{x^s 2}) \qquad (22)$$

And *u* can be defined as:

$$u_{x^s} = \frac{1}{2}(u_{x^s 1} - u_{x^s 2}) \qquad (23)$$

Combining Eqn. 25 and Eqn. 26, and noting that $u_{x^s 1}$ = U_0, u_{x^s} can be solved for. A 2nd order polynomial was then fitted to the experimental data to determine the initial values of $K^s_{v\,Mavi}$ and $K^s_{i\,Mavi}$. The values of $K^s_{v\,Mavi}$ and $K^s_{i\,Mavi}$ were iterated until the CFD disk thrust value matched the experimental value at U_0= 1.425. CFD simulations were also run at the remaining values of U_0. Figure 4-2 shows the percent difference between the final CFD disk thrust values and the experimental results. At U_0 = 1.425 m/s, the error is -0.52%, and at U_0 = 0.90 m/s, the error is 3.5%. Comparisons of CFD disk thrust measurements for other single disk experiments run at different velocities were all within 3.5% of the experimental value, with error decreasing as inlet velocity increased. The variation in disk thrust error with inlet velocity is an indication that the values of $K^s_{v\,Mavi}$ and $K^s_{i\,Mavi}$ may need further adjusting. It should also be noted that as inlet velocity decreased, and therefore disk force decreased, the error bands on disk force measurements increases. Overall, these results provide some confidence that the single porous disk in a channel is being modeled to a reasonable degree of accuracy in the CFD simulations.

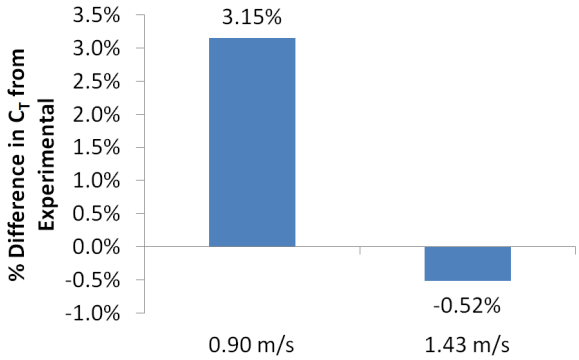

Figure 4-2: Percent difference in C_T between CFD simulations and experiments

4.3.3 Disk Force and Power Extracted Calculations

The details of the disk force and power extracted calculations are provided in the following sections.

4.3.3.1 Disk Force Calculations

The disk force was calculated by UVic according to the following equation:

$$D_{sim\ Uvic} = \int_{\mathcal{V}} K^{s}_{i\ Uvic} |\overline{u}| \overline{u_{x^s}} d\mathcal{V} \qquad \textbf{(24)}$$

The disk force calculated by Mavi was based on pressure difference between the disk upstream and downstream faces. This alternate thrust calculation method was done due to the unstructured nature of the mesh used by Mavi. The disk force was calculated by Mavi according to the following equation:

$$D_{sim\ MAVI} = \int_{S} \Delta p dS \qquad (25)$$

where Δp is the pressure difference between the upstream and downstream disk faces and S is the disk surface.

For the simulations, them method employed by UVic always gave the experimental disc force, while for Mavi's simulations, the difference between $D_{sim\ MAVI}$ and D_{exp} gave an indication of the CFD method's ability to predict the impact of different array configurations on the disc thrust.

The disk thrust coefficient is defined as

$$C_T = \frac{D_{sim}}{\frac{1}{2}\rho U_0^2 A_d} \qquad (26)$$

4.3.3.2 Disk Power Output

The mechanical power output for a turbine (approximated by the porous disc) was calculated by UVic using the following volume integration performed over the porous disc region:

$$P_{sim\ Uvic} = \int_{\mathcal{V}} K^{s}_{i\ Uvic} |\overline{u}| \overline{u_{x^s}}^2 d\mathcal{V} \qquad \textbf{(27)}$$

The disk power calculation used by Mavi differs from the UVic calculation due to Mavi's unstructured mesh. In the unstructured mesh, a cell on the front face of the disk does not necessarily have an

identical cell on the rear face of the disk. Using Eqn. 28 would require interpolation of velocities through the disk. Instead, Mavi's power calculation used the average velocity through the entire disk to calculate power according to the following formula:

$$P_{sim\ MAVI} = D_{sim\ MAVI}\,\overline{u_{x^s ave}} \tag{28}$$

The use of the average velocity in Eqn. 28 is adequate for disks that do not encounter wakes, or are completely engulfed in a disk wake. All of the disk configurations used in this report fall into these categories. In cases where a disk is partially in a disk wake, the power calculation described in Eqn. **27** is more appropriate.

These power calculations provide an ideal mechanical power output because they neglects losses from several sources including blade drag, wake swirl and bearing friction. In practice, mechanical power output will be lower than calculated by this equation.

Note that it is also possible to specify the applied momentum source terms directly. This can be used to specify any distribution of force (most commonly uniform) over the disk area. This method is termed the actuator disk approach. It is also possible to specify the momentum sources for a spinning turbine rotor based on airfoil lift and drag coefficients. Please see [10] section 2.4 for more details. Such approaches may be more useful for modeling real turbines; however the present approach is thought to be the most valid for porous disks.

The disk power coefficient is defined as

$$C_P = \frac{P_{sim}}{\frac{1}{2}\rho U_0^3 A_d} \tag{29}$$

4.4 CFD Model Geometry

The CFD model geometry is a replica of the test section of the flume tank at UVic. The flume tank was modeled as a simple rectangular channel with cross-section dimensions of 45cm by 45cm and a length of 2.5m. The porous disk is modeled as a thin cylindrical region. For simplicity, the disk support stings were not modeled. Figure 4-3 shows an example of the computational domain for the single disk configuration.

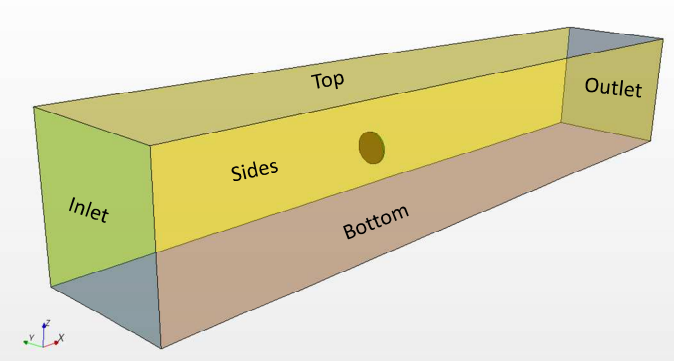

Figure 4-3: CFD model of flume tank

Due to the symmetry of the geometry, it is only necessary to model a quarter of the domain shown in Figure 4-3. This was done by UVic as it allowed for a more refined mesh to be used given the computational resources available.

In anticipation of modeling the porous disk in realistic tidal channel that will not allow for symmetry planes, Mavi chose to model the entire domain shown in Figure 4-3.

4.5 MESH

As described in the previous section, UVic and Mavi used two different mesh types; UVic modeled a *quarter domain structured mesh* while Mavi modeled a *full domain unstructured mesh*. Details on each mesh are provided below.

4.5.1 Quarter Domain Structured Mesh

UVic employed structured meshes generated by ICEM CFD software. Grid convergence studies were conducted for cases 1c and 7b to determine the grid spacing requirements to reduce the expected discretization error of $\overline{u}_x/U_0$ to less than 5% at all points within the wake. The mesh topology was slightly different for each case, but certain features were common for all meshes. The topology consisted of an octagonal region located in the core of each actuator disk, which was surrounded by orthogonal 'o-grid' blocks. This strategy allowed for a smooth transition of the mesh geometry from the circular porous disk to the square tunnel cross-section. It also maintained cell orientations orthogonal to the porous disks and resulting shear layer. The mesh was designed to have refined radial grid spacing Δr in the strong shear layer which forms at the outer edge of the actuator disk, which increases in diameter with downstream distance until the wake is fully expanded. The outer edge of this refined zone was located at a radial distance of $\sqrt{2}R$ which corresponds to the wake expanding to twice the area of the actuator disk, which occurs for the theoretical solution at the maximum power condition for a disk in an unbounded flow [11]. The z and y mesh spacing did not vary in the streamwise direction.

The general mesh topology for case 7b is depicted in Figure 4-4, where each edge is labeled. Note that symmetry boundary conditions were used along two planes to reduce the overall extents of the computational domain. The specific spacing used to define the mesh are summarized in Table 4-2. Note that in Table 4-2 the subscript 1 always refers to the end of the edge closest to the origin of the coordinate system. The edges 10 to 14 refer to the axial (x) mesh spacing. Edge 10 is from the inlet to Disc2 (at x = 61cm). Edge 11 is across Disc2. Edge 12 is from Disc2 to Disc1 (at x = 91cm), and Edge 14 is from Disk1 to the outlet. The resulting mesh is depicted in Figure 4-5.

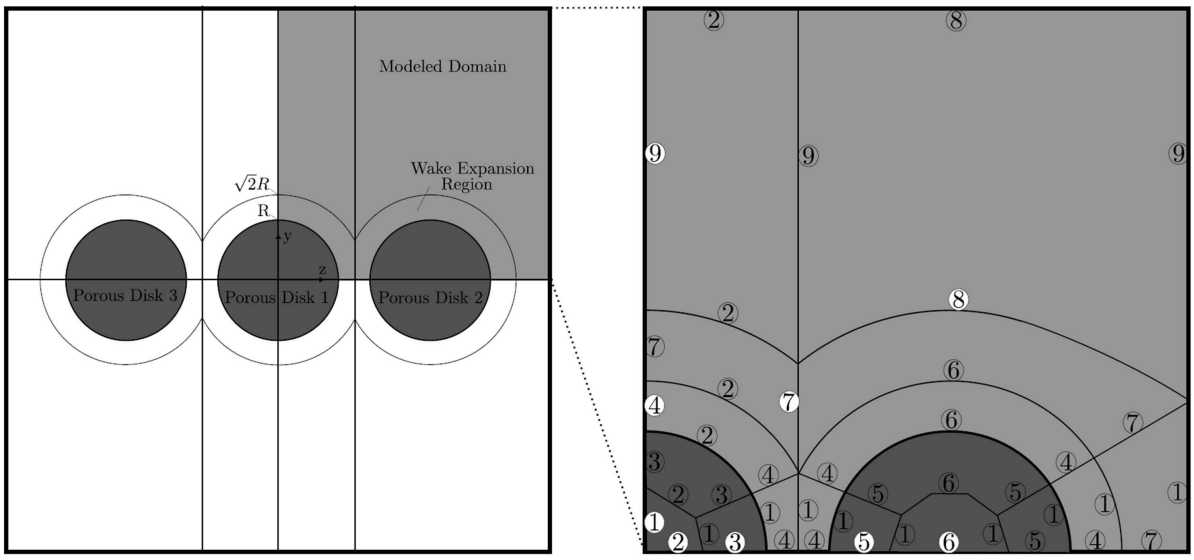

Figure 4-4: General mesh topology employed by UVic (z,y) plane (z axis is horizontal, x axis is in the streamwise direction)

Table 4-2: UVic mesh spacing for case 7b. Other cases used similar mesh sizes.

Edge	N_{nodes}	Expansion Law	$\Delta_1\ (mm)$	ER_1	$\Delta_2\ (mm)$	ER_2
1	15	uniform				
2	27	uniform				
3	27	bi-geometric			0.592	1.058
4	35	uniform				
5	27	bi-geometric	0.592	1.058		
6	54	uniform				
7	30	bi-geometric	0.592	1.058		
8	54	bi-geometric	2.070	1.029		
9	32	bi-geometric	1.780	1.058		
10	76	bi-geometric			0.592	1.058
11	10	uniform				
12	127	bi-geometric	0.592	1.029	0.592	1.058
13	10	uniform				
14	154	bi-geometric	0.592	1.029		

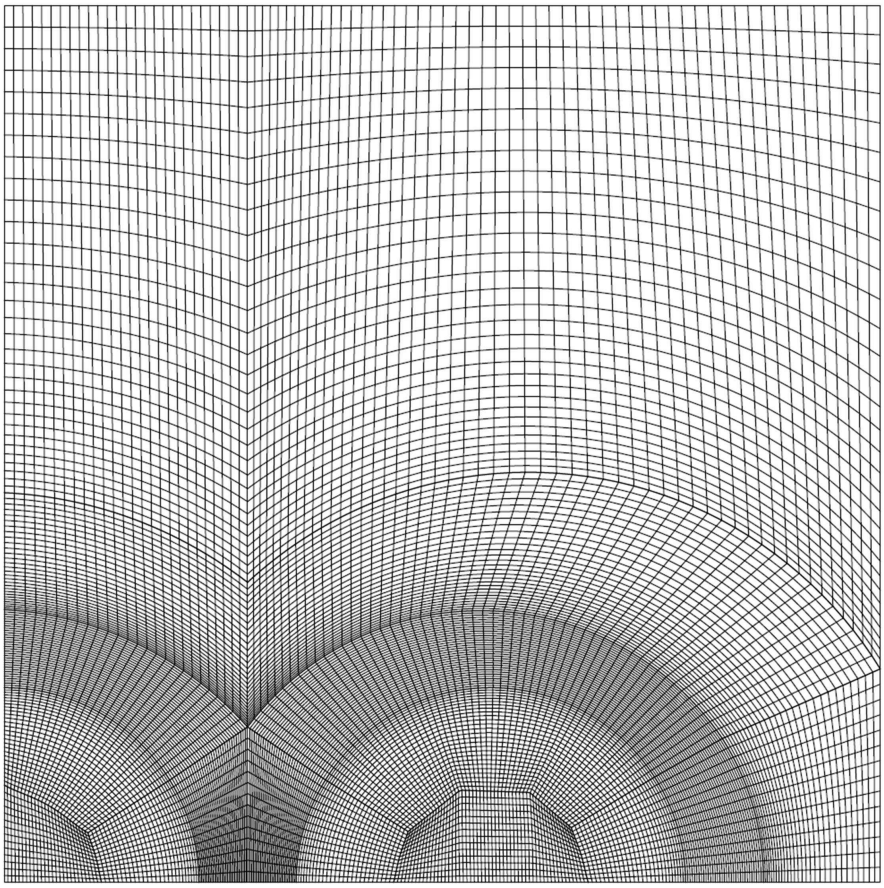

Figure 4-5: Transect of the UVIC mesh used for case 7b

4.5.2 Full Domain Unstructured Mesh

Mavi employed unstructured meshes generated by the STAR-CCM+ meshing software. A grid convergence study was conducted for the single disk configuration (case 1). The mesh topology was defined as shown in Figure 4-6 and Figure 4-7. Figure 4-6 shows a quarter of the porous disk mesh that is refined close to the disk edge. Figure 4-7 shows a top view of the CFD domain. Two cylindrical refinement regions are positioned around the disk. The inner refinement region extends 1 disk diameter upstream of the disk and 9.5 diameters downstream. The outer refinement region extends 2 disk diameters upstream of the disk, and 16 diameters downstream. Prism layers are also located on the sides and top and bottom of the domain to capture boundary layer development.

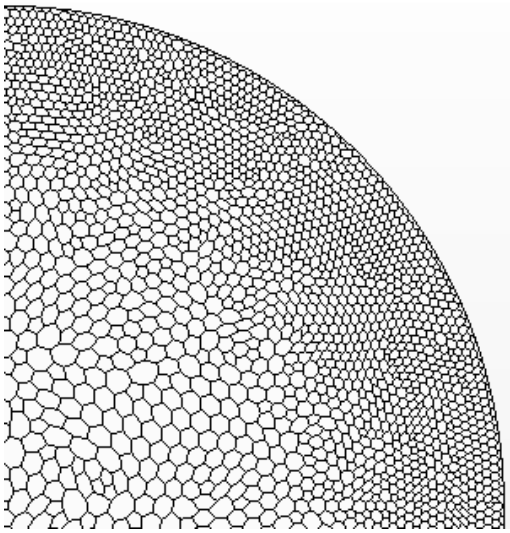

Figure 4-6: Mavi unstructured disk mesh

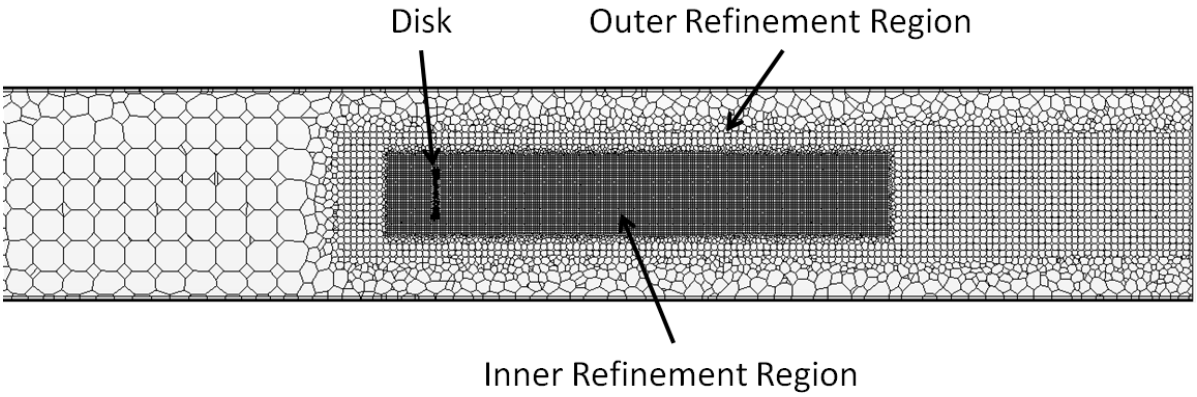

Figure 4-7: Mavi unstructured domain mesh

Three unstructured meshes were created of increasing density. The C_T and C_P values were compared between meshes. The difference between the medium and high density mesh in terms of C_T and C_P was 0.5% and 0.7% respectively. Based on these results, the medium density mesh was chosen. The mesh cell sizes on the disk, and refinement regions were used for all simulations, including multiple disk configurations. Mesh cell sizes are defined with respect to disk diameter so that the mesh can be easily scaled when modeling a larger disk in an ocean channel. Table 4-3 details the cell sizes with respect to disk diameter.

Table 4-3: Summary of Unstructured Mesh Parameters

Surface	Cell Size as a Percentage of Disk Diameter
Disk Face	1.8%
Disk Perimeter	0.9%
Inner Refinement Region	13.7%
Outer Refinement Region	64.0%

4.6 BOUNDARY CONDITIONS

The boundary conditions settings are depicted in Figure 4-8.

At the inlet, a uniform velocity was specified corresponding to the experimental data summarized in Table 3-5. The turbulence intensity and length scale were also set at the inlet. Uvic used an inlet turbulence intensity of 0.8% and a length scale of 25mm corresponding to the final values obtained from analyzing the experimental flows. Mavi used 2.0% intensity and a length scale of 17mm based on earlier estimates of turbulence provided by UVic. The top boundary used a free-slip condition.

UVic used free-slip boundaries for the sides, while Mavi used a no-slip condition.

The outlet was modeled as a pressure outlet set to atmospheric pressure in all cases.

The choice to use free-slip walls on the tunnel walls was made based on the fact that the walls of the tank are smooth. In addition, given the short length of the tank, the boundary layer would not grow beyond a few millimeters by the time it reaches the disk. Neglecting shear on the tank walls should therefore have a negligible effect on the flow field and thrust measured on the disk. This simplification allowed for the use of fewer cells because fine mesh near the boundaries is not required. In retrospect, due to the turbulence introduced by the discs the boundary layer growth may have been more significant than originally anticipated.

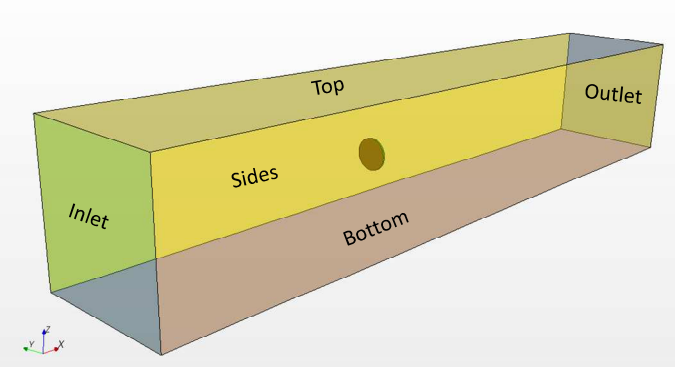

Figure 4-8: Closed channel CFD model of flume tank

4.7 INFLUENCE OF TURBULENCE INTENSITY AND LENGTH SCALE ON WAKE

Modeling multiple three-dimensional turbines in an array is not currently practical. Due to computational resource limits, turbine arrays are typically modeled using porous disks which remove energy from the flow as well as produce a wake region downstream of the disks. The length and size of a turbine's wake determines the minimum allowable spacing between multiple turbines arranged in an array. Therefore, these porous disks will need to be defined to produce a wake similar to that produced by the turbines they are representing.

To understand how free-stream and disk turbulence settings affect wake size and length, single disk CFD simulations were run. Four turbulence parameters were varied on a single disk configuration; inlet turbulence intensity, inlet turbulence length scale, disk turbulence intensity, and disk turbulence length scale. The following sections describe the results.

4.7.1 Inlet Turbulence Intensity

Free-stream turbulence intensity can vary significantly. Turbulence intensities in ocean channels can reach 20% while the turbulence intensity in a flume tank can fall below 1%. To determine the effect of free-stream turbulence intensity, or in the case of a flume tank, inlet turbulence intensity, simulations were run at different inlet turbulence intensities. The centre-line velocity through the tank is plotted in Figure 4-9 for three inlet turbulence intensity levels.

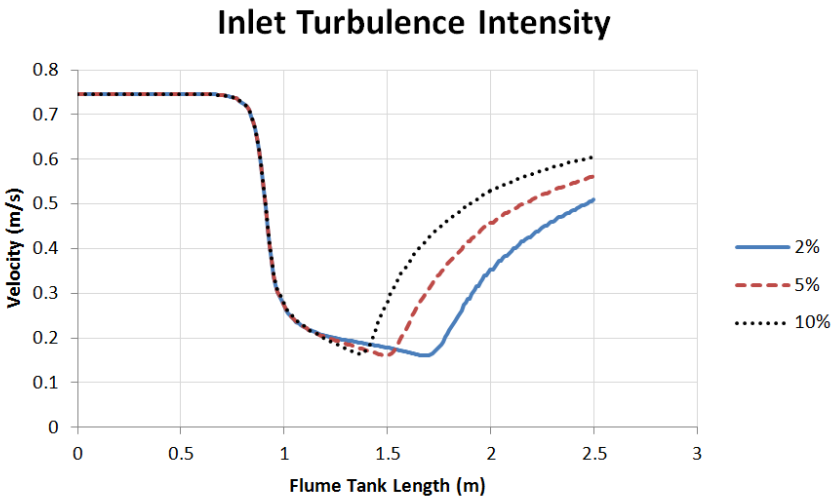

Figure 4-9: Centre-line velocity at different inlet turbulent intensities

The results show that inlet turbulence intensity has a significant effect on the disk wake recovery. As inlet turbulence intensity increases, mixing between the low energy disk wake and the high energy free-stream flow increases, causing the wake to recovery more quickly. The effect of inlet turbulence intensity on porous disk power coefficient is shown in Table 4-4

Table 4-4: Effect of Inlet Turbulence Intensity on C_P

Inlet Turbulence Intensity (%)	C_P
2	0.5903
5	0.5932
10	0.5992

The results in Table 4-4 show that inlet turbulence intensity has a minor effect on porous disk C_P with a difference of 1.02% between a turbulence intensity of 2% and 10%.

4.7.2 Inlet Turbulent Length Scale

Another factor that affects wake is turbulent length scale. Turbulent length scale describes the size of the large eddies in a turbulent flow. Inlet turbulent length scale was varied with all other settings being fixed. The centre line velocity through the tank is plotted in Figure 4-10 for three inlet turbulent length scales. The turbulent length scale of 0.0171m is calculated based on a fully developed pipe flow equation.

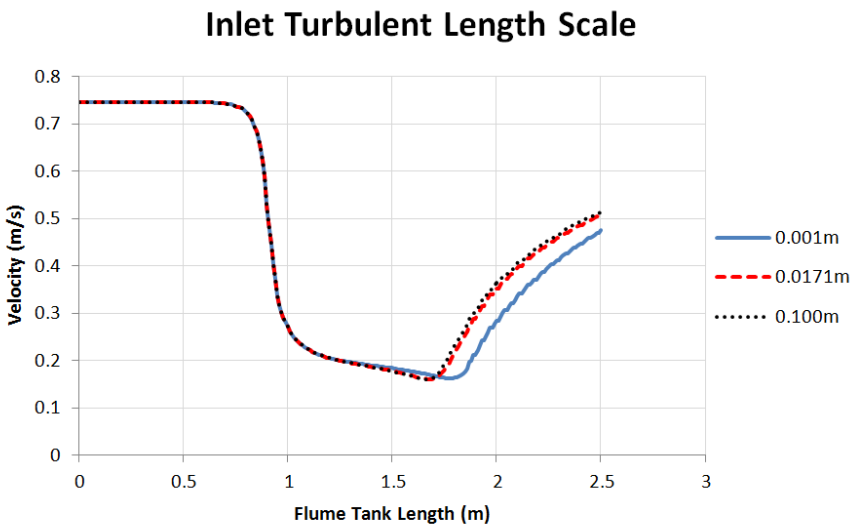

Figure 4-10: Centre-line velocity at different inlet turbulent length scales

The results show that inlet turbulent length scale affects the disk wake recovery. As inlet turbulent length scale increases the wake recovers more quickly. The change between a length scale of 0.001m and 0.0171m is greater than the change between 0.0171m and 0.10m.

The effect of inlet turbulent length scale on porous disk power coefficient is shown in Table 4-5. These results show that inlet turbulent length scale has only a minor effect on disk C_P.

Table 4-5: Effect of Inlet Turbulent Length Scale on C_P

Inlet Turbulent Length Scale (m)	C_P
0.0010	0.5898
0.0171	0.5903
0.1000	0.5908

4.7.3 Disk Turbulence Intensity

In physical experiments, as water flows through the porous disks, turbulence is introduced into the flow. This added turbulence increases mixing and accelerates wake recovery. To determine how much of an effect disk turbulence intensity has on wake recovery, disk turbulence intensity was varied with all other settings being fixed. The centre line velocity through the tank is plotted in Figure 4-11 for three inlet turbulent length scales.

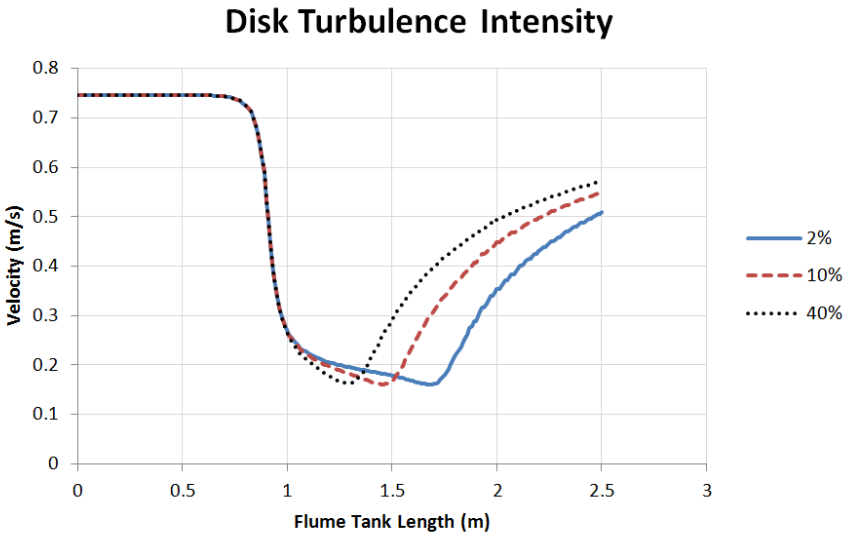

Figure 4-11: Centre-line velocities for different disk turbulent intensities

The results in Figure 4-11 show that disk turbulence intensity has a significant effect on wake recovery. Increasing disk turbulence intensity accelerates wake recovery. It was found that above a disk turbulence intensity of 40%, the rate of wake recovery did not significantly increase. Experiments by Harrison et al [12] showed the turbulence intensity directly behind a porous disk to be approximately 35%. Therefore, a disk turbulence intensity of 30% to 40% appears to be a reasonable level of turbulence intensity.

The effect of disk turbulence intensity on disk C_P is shown in Table 4-6. Disk turbulence intensity has a minor effect on disk C_P, with a 1.17% difference between 2% and 40% disk turbulence intensity.

Table 4-6: Effect of Disk Turbulence Intensity on C_P

Disk Turbulence Intensity (%)	C_P
2	0.5903
10	0.5935
40	0.6004

4.7.4 Disk Turbulence Length Scale

Disk turbulent length scale was varied with all other settings being fixed. The centre line velocity through the tank is plotted in Figure 4-12 for three disk turbulent length scales.

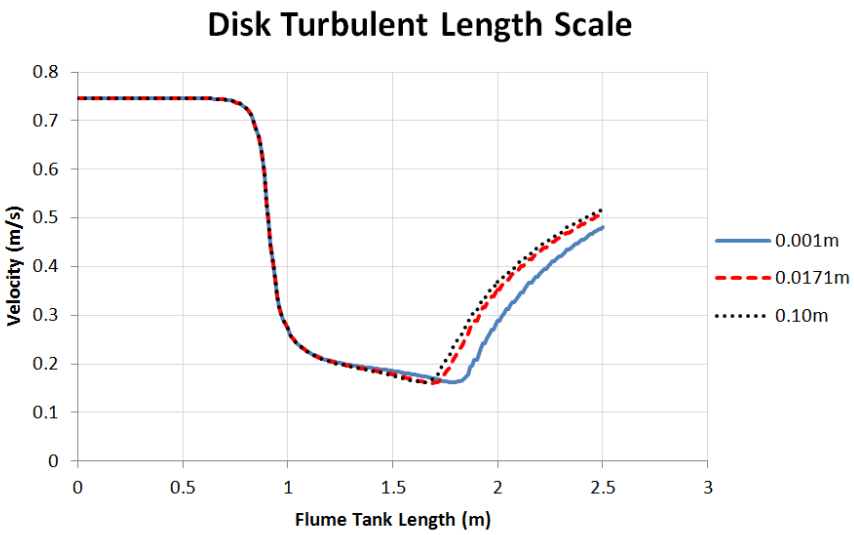

Figure 4-12: Centre-line velocities at different disk turbulent length scales

Table 4-7 shows that disk turbulent length scale has a similar effect on wake recovery as inlet turbulent length scale. Increasing disk turbulent length scale increases wake recovery rate.

Table 4-7: Effect of Disk Turbulent Length Scale on C_P

Disk Turbulent Length Scale (m)	C_P
0.001	0.5900
0.0171	0.5903
0.100	0.5905

4.8 Porous Disk Force Comparison to Experiments

As discussed in section 4.3, two approaches were taken when modeling the porous disks in CFD simulations. The approach taken by Mavi was to calibrate the CFD porous disk to the single disk experiments conducted by UVic. The porous disk resistance coefficients and disk turbulence settings were adjusted to have the same thrust as the single disk experiments while having a wake recovery as close to experiments as possible. The same porous disk settings were then used for all disk configurations and velocities. This approach allows one to assess how well the CFD porous disk model simulates porous disks arranged in arrays.

4.8.1 Final Porous Disk Settings

Using the knowledge of how wake is affected by disk turbulence settings, the disk turbulence intensity was set to 35% and disk turbulent length scale was set to 0.075m to increase wake recovery. Figure 4-13 shows a comparison of the experimental and CFD centre-line velocity for experiment Set 1c. Figure 4-13 shows that the CFD simulation wake initially recovers at a faster rate than the experiment. However, beyond approximately 6 diameters downstream, the experimental wake velocity recovers more than the CFD results. Based on the experiments by Harrison et al [12], increasing disk turbulence intensity above 35% was determined to be unrealistic, and increasing disk turbulent length scale beyond

0.075m did not have a significant effect. Possible reasons for the lower wake recovery in the CFD simulations are discussed in section 4.9.1.

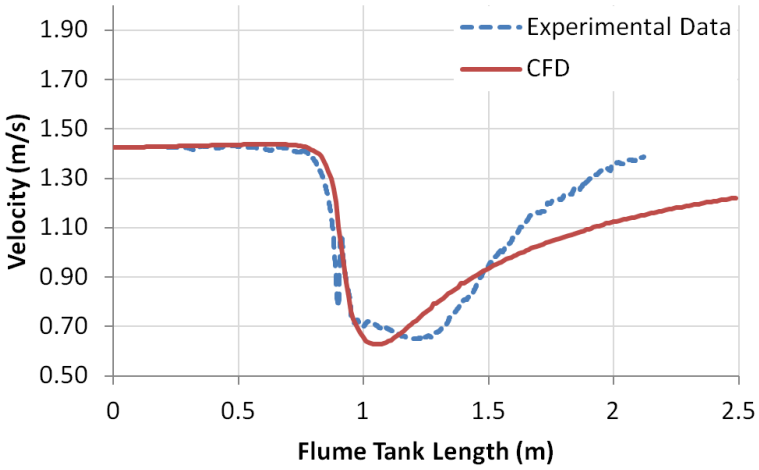

Figure 4-13: Centre line velocity comparison between experiments and CFD

4.8.2 Multiple Porous Disk Comparisons

Using the porous disk settings defined in section 4.8.1, several multiple disk configurations were run in CFD and compared to the experimental results. The difference between CFD and experimental thrust for experiments 1c, 3a, 4a, and 7b are shown in Table 4-8. The results show that the CFD simulations are able to predict disk forces on multiple disk simulations to within plus or minus 7.7%.

Table 4-8: Percent difference in disk thrust from experimental

	% Difference in Thrust from Experimental	
Set 1c	**Front Disk**	
	-0.52%	
Set 3a	**Front Disk**	**Rear Disk**
	-5.30%	7.01%
Set 4a	**Side Disks**	
	-6.27%	
Set 7b	**Side Disks**	**Centre Disk**
	-6.41%	-7.69%

In general, the CFD simulations tended to under predict the force on the porous disks. An under prediction of the disk force was expected based on the single disk calibration results. However, the magnitude of the under prediction for the multiple disk simulations was significantly larger than the single disk results.

Several factors may contribute to the larger under prediction of disk force for multiple disk configurations. As discussed in section 4.3.2, the porous disk model used in the CFD simulations may not accurately characterize the porous disk behavior over the full range of free-stream velocities. Another possible factor is that the steady-state CFD simulations do not fully capture the time dependant vortex structures that are shed from the disks and their interactions with each other.

An exception to the disk force under prediction is the CFD simulation of Set 3a, where the rear disk force is over predicted. Referring to Table 3-3, experiment 3a consists of two disks arranged with one disk directly downstream of the other. The force on this downstream disk is highly dependent on the wake velocity of the upstream disk. From Figure 4-13, it is known that the CFD wake velocity tends to be higher than the experimental wake velocity within about 6 disk diameters downstream of the disk. In Set 3a, the downstream disk is located 3 disk diameters downstream of the front disk, and therefore sees a higher CFD velocity than the experiments. This higher CFD velocity results in an over prediction of the downstream disk force. This result illustrates how important it is to accurately model turbine wakes when they are arranged in array configurations.

4.9 ASSESSMENT OF CFD WAKE PREDICTION

This section provides a direct comparison of the wakes predicted using CFD simulation to those obtained from PIV data. The simulations by UVIC used the estimates for turbulence intensity (0.8%) and length scale (25mm) determined from the PIV data. The simulations by Mavi were run before the turbulence analysis was finalized, and used 2% turbulence intensity at the inlet with a length scale of 17mm. Additionally, Mavi's simulations used a no-slip condition on the tunnel walls, and simulated the full domain. The UVIC simulations used a no-slip wall condition and used two symmetry planes to model only 1/4 of the domain. Mavi also introduced sources of turbulence at the porous disk location which produced 35% turbulence intensity at a length scale of 7.5cm.

This section presents a comparison of the wakes predicted by UVic's and Mavi's simulations to the PIV data using contour plots shown in Figure 4-14 to Figure 4-17. In each plot the PIV wake is the uppermost plot, with the UVIC simulation in the middle, and Mavi's simulation at the bottom. The contours depict the time-averaged axial velocity normalized by the inflow velocity ($\overline{u}_x/U_0$). The x-axis is normalized with disc diameter, while the y-axis is normalized with the disc radius. This scaling results in wakes that appear shortened relative to their width, and was done to allow a better visualization of the wake structures.

In general, the wakes predicted by UVic are similar to the PIV data until approximately 4 diameters downstream of the disc. Beyond that, the wake recovery is too slow. The experimental wakes recover much faster and more fully. The simulations by Mavi show a faster initial wake recovery due to the larger inflow turbulence intensity and turbulent sources at the disc. The wakes shown in Mavi's simulations still recover too slowly downstream of about 6 diameters.

The contours for case 3a show less variation between the simulations by UVIC and Mavi. It seems that the inflow/disk turbulence parameters have less impact on the initial wake recovery with two disks in tandem compared to the single disc or other multi-disc cases.

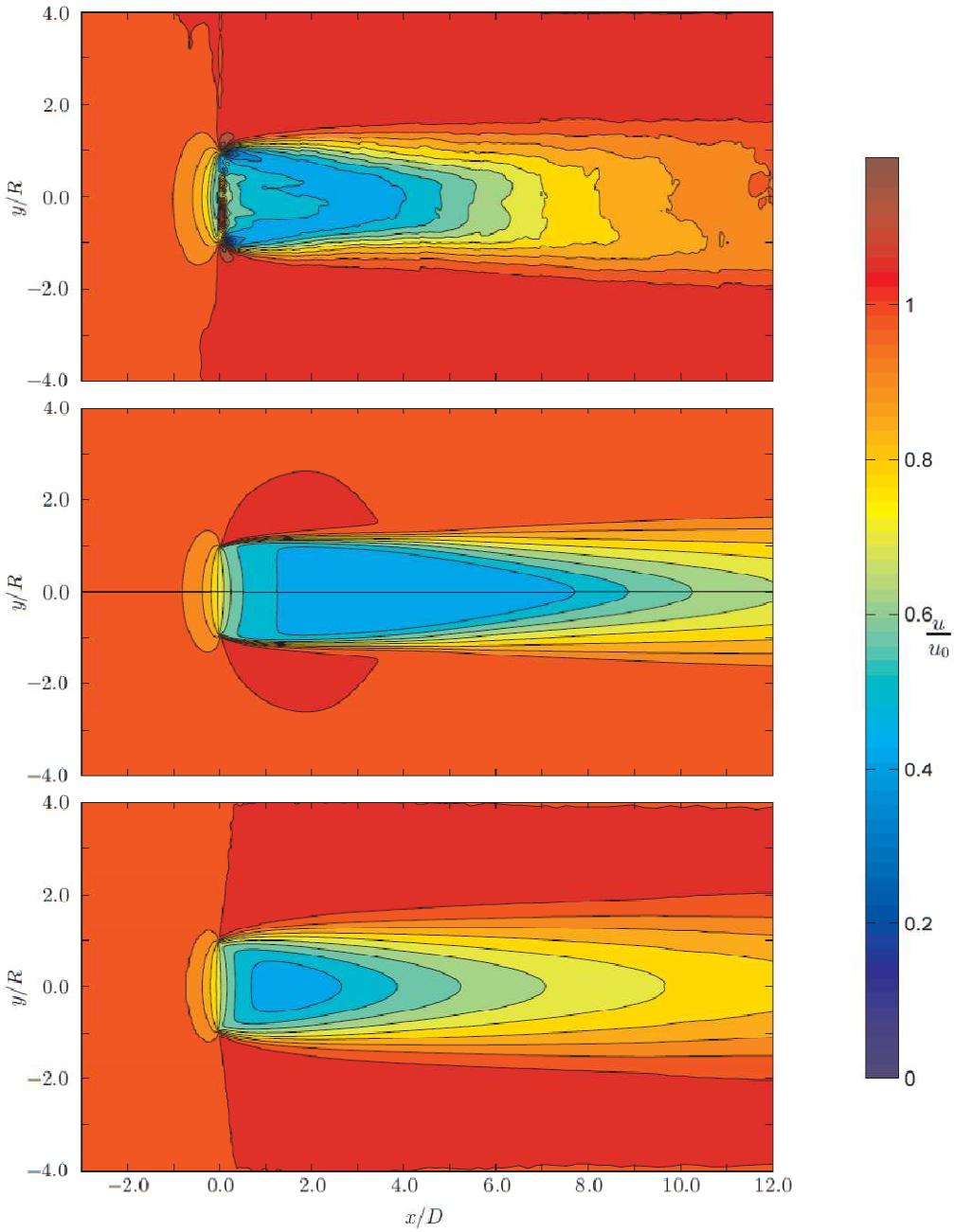

Figure 4-14: Contour plots comparing the wake structure for case 1c (single disc) from PIV (top), UVIC sim (middle) and Mavi sim (bottom)

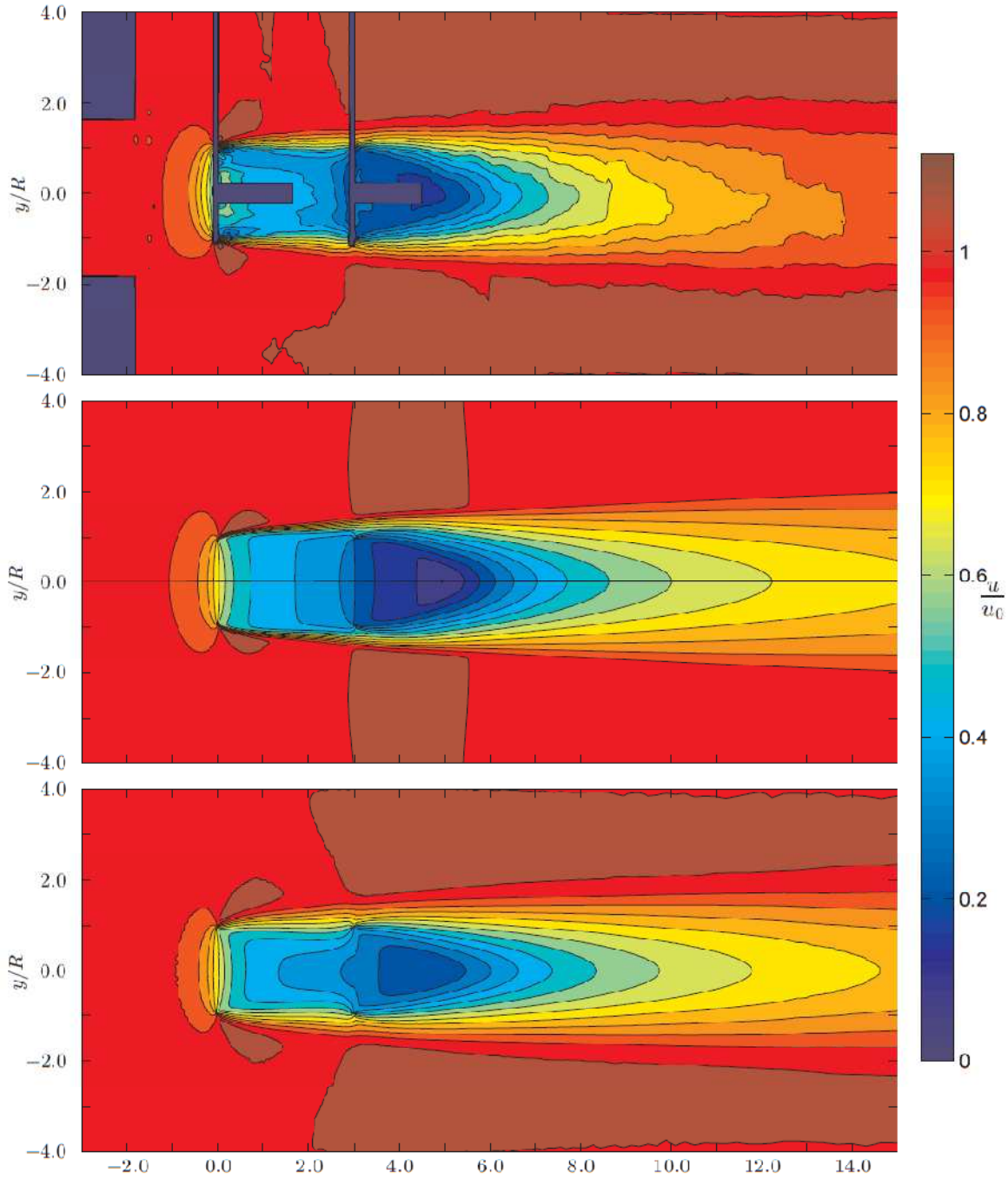

Figure 4-15: Contour plots comparing the wake structure for case 3a (two discs in tandem) from PIV (top), UVIC sim (middle) and Mavi sim (bottom)

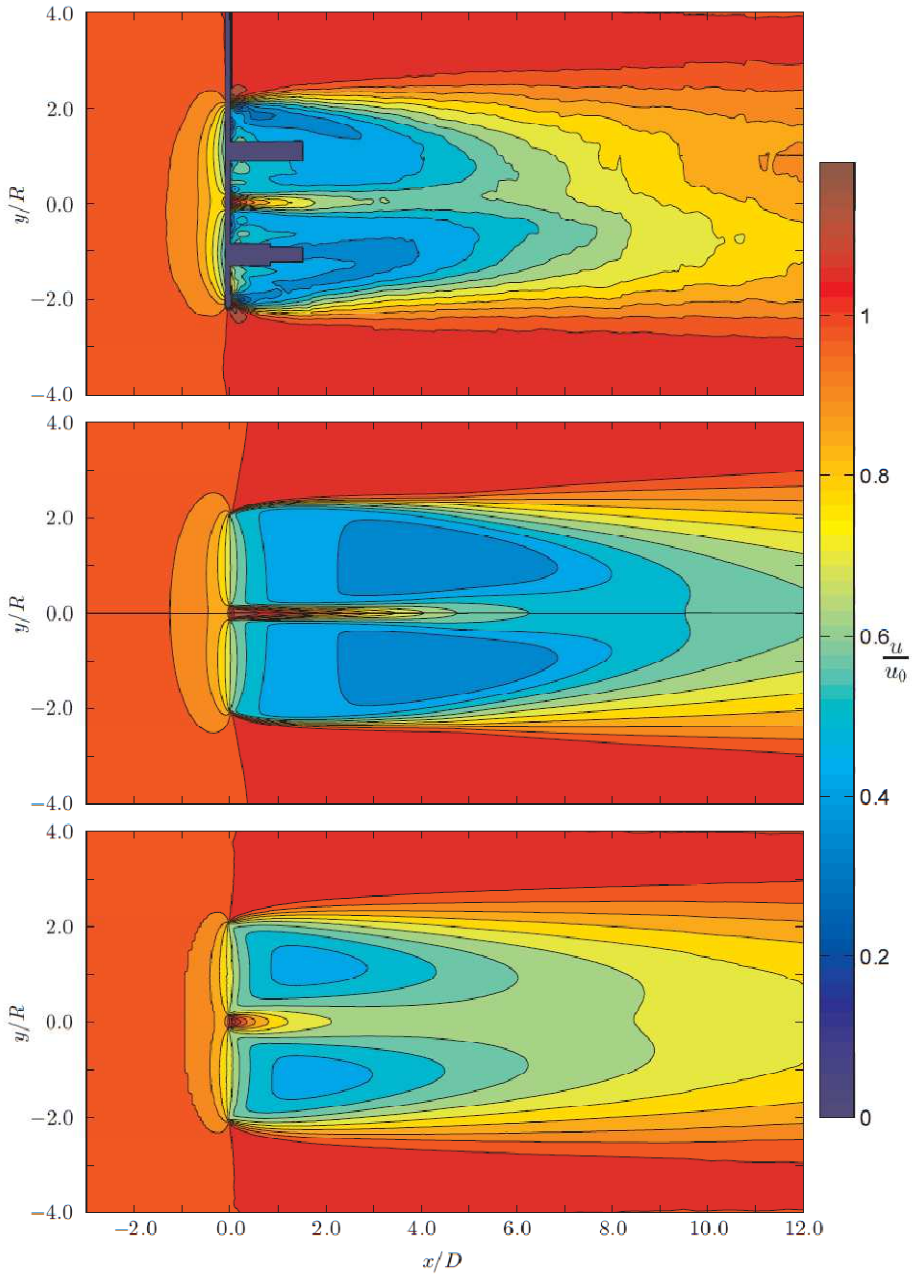

Figure 4-16: Contour plots comparing the wake structure for case 4a (two discs side-by-side) from PIV (top), UVIC sim (middle) and Mavi sim (bottom)

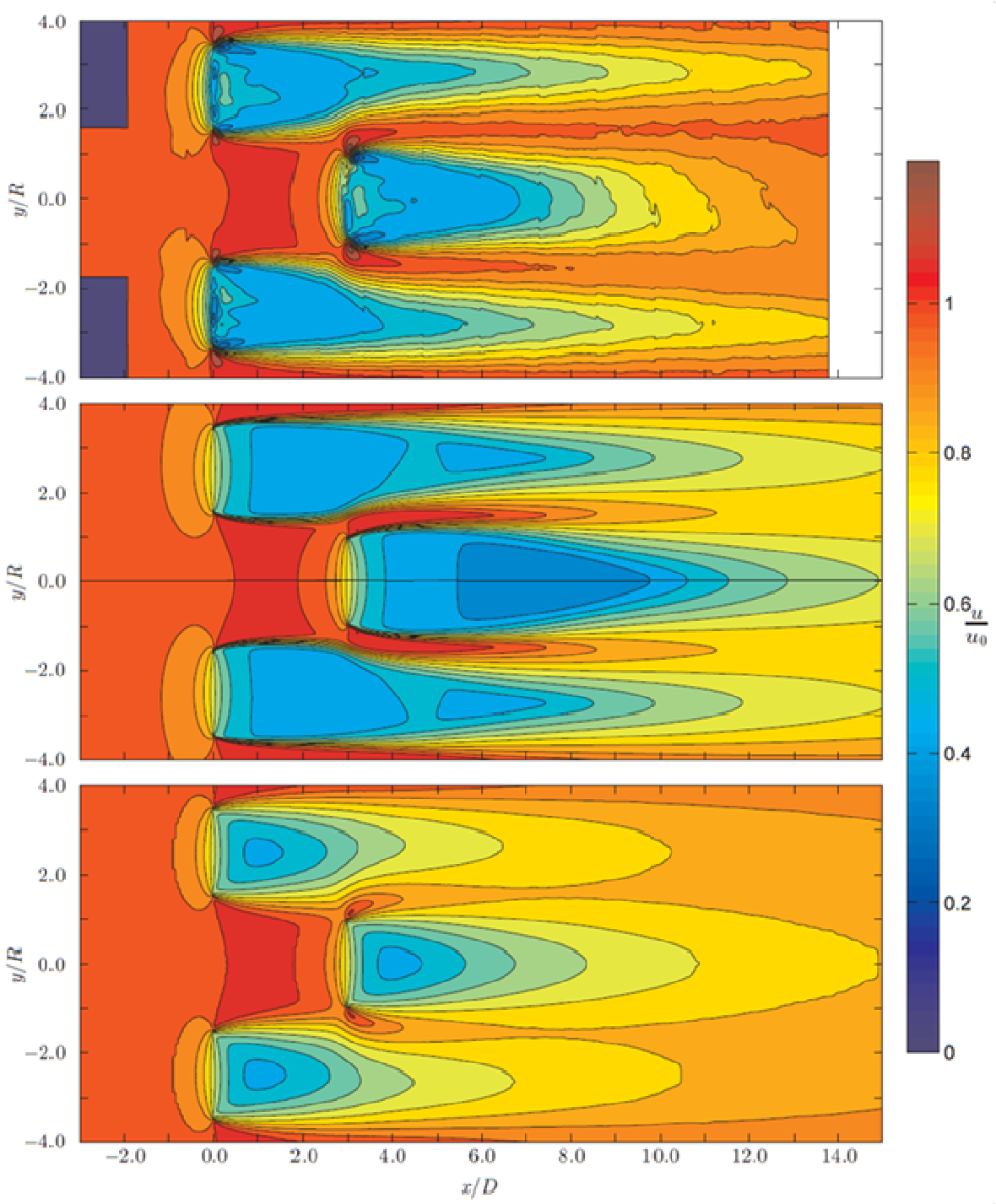

Figure 4-17: Contour plots comparing the wake structure for case 7b (three discs staggered) from PIV (top), UVIC sim (middle) and Mavi sim (bottom)

4.9.1 Using turbulent sources as tuning parameters

It is interesting to observe that in Mavi's simulations, the wake recovery immediately behind the disk is initially faster, and then slows down further downstream when compared to experimental data. Since

greater levels of turbulence result in faster mixing and therefore faster wake recovery, this could imply that the turbulence is initially too high, but then decays too quickly. A reasonable approach to improving the CFD method for porous disks may be to adjust the empirical constants used in the equation for the dissipation rate to mitigate this observed behavior. This strategy has not yet been attempted due to time constraints.

It is evident that it is possible to use the inflow turbulence intensity as well as the disk turbulence sources as tuning parameters to adjust the wake recovery in the simulation. However the problem with such an approach is that as more turbulence is added, the wake becomes increasingly diffused-out and loses its correct structure. As more turbulence is added, the effective viscosity increases, smoothing out any gradients in the flow. This is most evident in the Figure 4-17 for case 7b. The flow is characterized by three distinct wakes with fast flowing jets in between. In UVIC's simulation, the faster flowing jets are quite similar to the PIV data, but the wakes recover far too slowly. In Mavi's simulations, the wakes recover faster (but not as fully as the experimental flow) but the faster flowing jets become completely diffused out. This trend was also noted in UVIC simulations with source terms for turbulent kinetic energy added in the porous disk region (not shown here).

From the experimental data, it has been noted that large vortical structures were shedding from the edges of the porous discs (see section 3.11). The shed vortices had diameters approaching 1/3 of the disc diameter, and persisted as coherent structures for several diameters downstream of the discs. RANS simulations attempt to model the momentum transport of turbulent structures by increasing the effective viscosity. This gives faster transport across shear layers and does give faster wake recovery. However it also assumes that the underlying turbulence is isotropic (for two-equation turbulence models) and that it consists of small-scale eddies. Neither of these assumptions is true for the experimental flows presented in this report. It seems that the correct momentum transport for these flows would be best modeled using large eddy simulation, which would resolve the larger eddies explicitly while treating the smaller scale eddies with a sub-grid closure, but at greatly increased computational cost compared to RANS simulations.

It is important to note that the wakes of actual turbines will not have the same type of vortex shedding as the porous disc experiments present in this report. Their wakes will be characterized by a more typical helical wake consisting of strong, coherent tip vortices. Adequate validation of the ability of CFD simulations using the porous-disc approximation to predict the wake recovery behind spinning rotors remains to be carried out. Despite the mediocre ability of the porous disc simulations to replicate the experimental flows in this study, they may perform better for real rotor wakes, which will be less chaotic than the porous disc flows presented in this report.

4.10 SUMMARY

It was found that the steady-state RANS simulations do a reasonable job in predicting the thrust force acting on porous discs in several different array configurations considered in this study. The largest discrepancies between the experiments and the CFD prediction of thrust occurred for a porous disc in the immediate wake of an upstream disc (separated by 3 diameters), and for the array with one turbine in the faster-flowing jet created in the gap between two upstream discs. Even in those cases, the thrust was predicted within less than 8%.

The prediction of power will vary in proportion to the product of thrust and the volume averaged velocity through the disc. Since experimental values of the flow velocity through the disc were not directly available, the accuracy of power predictions is more difficult to assess. A rough assessment is possible by noting that the thrust is proportional to u^2 while the power is proportional to u^3, and assuming that the underlying reason for the discrepancy in thrust is a discrepancy in u. Then, using error propagation methods, we can state that the error in power is 3/2 times the error in thrust. Thus, the power prediction for the RANS CFD simulations is likely within 12% for all of the array configurations considered in this report.

The steady-state RANS simulations do a reasonable job in predicting the wake recovery behind turbines, however significant tuning of turbulence parameters is required to get a good match to experimental data. Generally, the simulated wakes recover too slowly unless sources of turbulence are added at the disc. Furthermore, the turbulence seems to decay too rapidly in the simulations. This could be addressed in the future by changing turbulence model coefficients. Considering that the wake behind a spinning rotor will likely differ from that of a porous disc, there is not a great deal of value in fine-tuning the turbulence parameters for the porous disc simulations. This should, however be done as detailed wake recovery data for real rotors becomes available. The CFD simulations were considered adequate for the purpose of assessing the feasibility of integrating CFD and ocean-scale simulations methods, and were used as described for the remainder of the project.

5 OCEAN MODELING OF IDEAL CHANNEL

Hydrodynamic ocean models are used to calculate large-scale circulation resulting from a range of ocean physics. Over the last 15 years, these types of models have increasingly been used to estimate tidally driven flows for the purpose of assessing the available tidal energy resource. The problem with this methodology for tidal resource assessment is that it only examines the tidal system in its natural state neglecting the impact of turbines on the flow.

Deployment of tidal turbines changes the tidal system, and so the energy potential is also changed. Admittedly, for small projects, the change in energy potential of the system is also small, so assessment of resources of the natural tidal system is valid. But the tidal industry is nearing a point of commercialization, and as that happens developers are perusing larger and larger installations. As this happens, strategies are required to assess the tidal system including the proposed tidal installation.

This section covers the development of a methodology for approximating tidal turbines within a general Ocean model. This method takes advantage of the inherent computational efficiency of the Ocean model by representing the turbines as sub-grid drag elements.

5.1 METHODS OF REPRESENTING TURBINES IN OCEAN MODELS

General Ocean models, such as the one used for this study, cannot approximate turbines directly. This class of models uses the Reynolds equations with the hydrostatic (no free-surface deformation) approximation. The spatial approximation is decomposed into a 2-dimensional horizontal part and a 1-dimensional vertical part for computational efficiency and to properly account for gravity forces.

Although the grid is unstructured in the horizontal direction, it is structured in the vertical direction because vertical cell edges are placed below each vertex in the horizontal grid. Hence there is a limited ability to represent other shapes than squares. Moreover, any increase in resolution around an object must extend both vertically and horizontally. This leads to reduction in time step size to preserve accuracy and may exceed Courant number constraints. It is not feasible to accurately resolve a tidal turbine in a model that extends over a large area; under resolving leads to invalid solutions.

The alternative is to volume average over the sub-grid objects. This leads to a classic closure problem with new terms accounting for spatial dispersive stresses, for form drag, and for skin friction. Form drag is the most important term and can be treated with standard form drag expressions. Of interest here is to calculate these terms based on the results of a CFD model, thereby effectively coupling the large scale and small scale models.

5.2 FORM DRAG IN OCEAN-SCALE MODELS

Form drag can be formally introduced into the governing equations through double- averaging methods (DAM) [13] [14]. First the equations are Reynolds-averaged over turbulent time scales following traditional methods, and then the equations are volume- averaged in space. The unresolved sub-grid objects appear as volume integrals in the equations and are usually dealt with as form drag. Here we assume that the solid fraction in a volume is much less than the fluid volume, and that the integrals can be expressed as a standard quadratic drag force. The latter is justified by many published experiments with circular discs and from turbine power rating curves. A study by Walters and Plew [15] gives more detail about the methods adopted here.

Form drag is defined as:

$$F_d = (1/2)\rho A_f C_T \mid \boldsymbol{u} \mid \boldsymbol{u} \tag{30}$$

Where ρ is density, A_f is the frontal area of an object measured in the plane that is normal to the direction of flow, C_T is the non-dimensional drag coefficient, u is the reference free-stream velocity, and boldface type denotes a vector quantity.

Form drag that is modeled as a subscale process can be included into the momentum equation in a general sense with the body force terms. To achieve this form drag must be specified per unit volume, which is given by:

$$f_d = (1/2)\rho \lambda_f C_T \mid \boldsymbol{u} \mid \boldsymbol{u} \tag{31}$$

where λ_f is the frontal, A_f divided by the averaging volume and $\boldsymbol{f_d}$ is the volume averaged force applied in the Ocean model. From a model perspective, the obvious averaging volume is the volume of a computational cell (an element volume when using finite element methods).

Several issues arise from this formulation for turbine induced drag in the Ocean model. The first is that the free-stream velocity is not well defined in the ocean model. Only the cell averaged velocity is available. Using a cell averaged velocity from a cell upstream of the turbine is an option but is problematic to implement because of changes in flow direction induced by tides. In the initial development of this methodology (discussed in Section 6.2), the free stream velocity was approximated as the local cell averaged velocity then corrected based on empirical relations derived from experiments with flow through vegetation [15]. Current work focuses on improving these approximations.

A second issue follows from the first in that C_T for a turbine is usually derived from physical or numerical experiments of a single turbine in a free-stream flow. The free stream current velocity is not available in the Ocean model. These issues necessitate an adjusted representation of the turbine drag based on the cell averaged velocity.

The turbine representation of current research focus is:

$$f_d = (1/2)\rho \lambda_f C_T^* \mid \boldsymbol{u_{cell}} \mid \boldsymbol{u_{cell}} \tag{32}$$

Where u_{cell} indicates the velocity averaged over the Ocean model computational cell. The local turbine drag coefficient C_T^* is calculated as follows:

$$C_T^* = T/(1/2\,\rho {u_{cell}}^2 A_f) \tag{33}$$

Where T is the turbine thrust imparted on the flow by both the turbine and support structure. Where the turbine spans more than one cell an appropriate portion of the total turbine thrust (T) and frontal area (A_f) is used.

A power coefficient, C_P^*, similar to C_T^* in Eq. (**33**), may be used to estimate turbine power in the Ocean model. The relationship between power, P, and C_P^* is:

$$C_p^* = P/(1/2\,\rho \boldsymbol{u_{cell}}^3 A_f). \tag{34}$$

5.3 FLUME TANK SCALE RICOM MODEL

The Ocean model was used to simulate the Fume Tank Experiments performed by UVic. Using the concept of volume averaging, the grid was kept coarser than the disk. The grid was extended to 4.5 m to allow an upstream relaxation of the flow before the 2.4 m test section. The simulation has a free surface while the experiments did not. A discharge is introduced at the end of the extended flume and a water surface elevation of 0m was maintained at the outflow. The grid was adjusted so that the disk was located at x = 0, where x is the distance along the flume. Two grids were assessed:

1. 10 quadrilateral elements along the flume and 1 across (0.45 m by 0.45 m), and;
2. 30 quadrilateral elements along the flume and 3 across (0.15 m by 0.15 m).

The latter is representative of the scaling between cell size and turbine diameter that would be used in the field-scale simulations.

The form drag from the disk is represented as in Eq. (**32**). A disk diameter of 0.1m was used. The 0.15 m by 0.15 m grid was used with turbine drag applied to the centre cell at x = 0 m. Figure 5-1 shows the color contours of the water elevation and current vectors for this test. The location of the disk is given by the identifier 'd'. The flow is driven to 1.8 m/s by the head difference between the inlet and the outlet. The current vectors show the flow deviating around the cell containing the turbine.

Because of the size of the disk, the grid size could not be further reduced. Given the tank dimensions the grid size restriction obviously limits the detail of the result. For this reason most of the testing of the coupling methodology was performed using a full scale idealized open channel. This work is discussed in the following section.

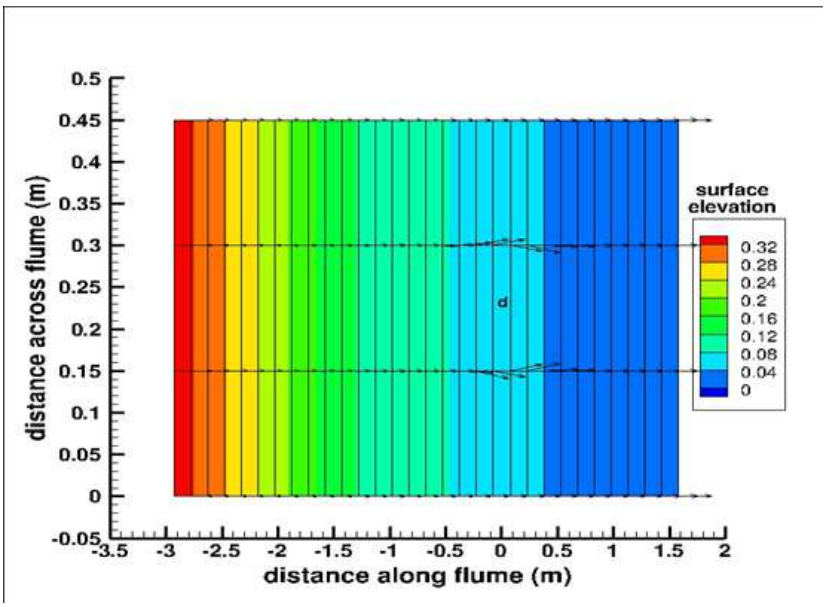

Figure 5-1: RiCOM model of flume tank

5.4 FULL SCALE OCEAN MODEL OF IDEALIZED OPEN CHANNEL

Testing of the form drag based coupling methodology was conducted using a simplified ocean-scale test channel. The purpose of using a simplified test channel was to provide an ocean-scale platform to vet

each aspect of the coupling methodology without introducing complicated flow such as eddies which might obscure the results.

Initially it was proposed to also perform tests using a simplified ocean basin. As the project progressed it was decided to use only the channel. The reason for this is that all flow conditions that might be experienced in the basin scenario can also be reproduced in the channel scenario and the flow conditions in the channel scenario are easier to control. In the basin scenario the flow would depend not only on the boundary forcing, but also the geometry of the basin. In the channel scenario the flow is dependant only on the boundary forcing.

The first tests were performed with a single turbine to identify the appropriate averaging volume. A further array of tests was performed with a single turbine to assess the coupling methodologies performance under various flow speeds, in the presence of turbulence and bottom friction. Additional tests were performed to assess the performance of the coupling methodology for a small array of turbines.

5.4.1 Test Channel Description

The test channel is 5*km* long, 1*km* wide, and 50*m* deep from mean-sea-level (MSL, the reference elevation) to the flat bed. A discharges of 50,000, 150,000, and 250,000m^3/s are introduced at the inflow boundary and an essential condition is imposed on water surface elevation, $\eta=0$, at the outlet. These conditions result in average water speeds of 1, 3, and 5*m*/*s*.

Taking the reference location (0.,0.,0.) at the surface (MSL) at the upstream centerline, a single turbine was placed at (2000.*m*,0.*m*,–25.*m*) or at mid-depth on the centerline at a distance of 2*km* from the upstream boundary. The only exception to this was Test Set 3 (bottom friction), in which the turbine was located at (2000.*m*,0.*m*,–35.*m*). In all tests the turbine has a diameter of 10*m*.

5.4.2 Ocean Model Setup

The Ocean model was constructed using a range of regular, rectangular grids. In the horizontal, grid spacing (Δx) of 40, 20 and 10m was used. In the vertical a range of grid spacing (Δz) from 5 to 0.625m was used. The particulars of each grid are given with each test set.

Vertical viscosity (a parameter relating to turbulence), A_v, was specified either as a constant, or calculated through the use of a k-ε turbulence closure sub-model that is appropriate for coastal ocean spatial scales.

In initial tests no bottom friction was applied, so no boundary layer developed. In later tests a bottom friction coefficient of $C_b=0.01$was applied so that a realistic boundary layer developed within the model.

Basic test parameters are summarized in Table 5-1.

Table 5-1: Model coupling initial test parameters

Geometry	Rectangular - 1km wide x 5km long x 50m deep
Inflow condition	Mass flow
Inflow speed	1, 3, 5 m/s
Turbulence	Constant vertical viscosity, k-ε turbulence closure
Bottom Friction	None, C_b=0.01
Turbines	10m diameter, C_T= 8/9
Turbine placement	Centre of channel, 2 km from inlet

5.4.3 Averaging Volume

For all tests, volume averaging was performed over a box which is square in plan view, but possibly rectangular in profile view. The horizontal dimensions of the averaging volume were set equal to the computational grid cell of the ocean model so that a different computational grid was used for each different averaging volume sizes. For the depth-averaged (2d) case, the averaging volume was defined by the area of the computational cell in the horizontal and the depth in that cell. For the 3d case, the averaging volume is defined by the area of the computational cell in the horizontal and a value similar to the horizontal dimension in the vertical. The vertical dimension of the averaging volume did not necessarily correspond to computational cell size in the ocean model, so the averaging volume may span several computational cells in the vertical.

Note that *dx* and *dz* indicate the horizontal and vertical dimensions of the averaging volume and *Δx* and *Δz* indicate the horizontal and vertical dimensions of the computational cells in the Ocean model.

5.4.4 Input Parameters from CFD Models

To obtain the turbine drag and power coefficients UVic constructed a CFD model of a portion of the test channel containing the turbine. The computational mesh from the lab-scale experiments was scaled by a factor of 100 to achieve a turbine of 10m diameter. The domain was extended laterally and used an o*pening* boundary condition on the lateral bounds to eliminate boundary proximity effects on the turbine. The domain was extended vertically to produce a 50m total depth. A rigid lid approximation was used for the free surface, and the top boundary used a *free slip* condition. The bottom boundary was either *free-slip* or used a specified shear stress consistent with the specified velocity profile. Symmetry planes were used when applicable to reduce computational cost. The inflow velocity was set according to the specific test (constant value of 1, 3 or 5 m/s or a specified velocity profile) and the inflow turbulence was set to the option *High* giving 10% turbulence intensity. A pressure outlet was used with the reference pressure set to 0 Pa. The turbines were specified to have a constant resistance coefficient *K* that set the quadratic streamwise resistance term C_{R2}^{s} in Eq. (**35**) according to:

$$C_{R2}^{s} = \frac{1}{2}\frac{\rho K}{t_d} \qquad \textbf{(35)}$$

where t_d is the thickness of the porous disk region in the simulation. Using $K = 2.0$ results in a thrust coefficient of approximately 8/9 (C_T=8/9). For each test case, the velocity around the turbine was

averaged over the appropriate volume, and the local turbine drag coefficient (C_T^*) was calculated using Eq. (**33**). The only parameters passed from the CFD model to the ocean models are C_T^* and C_P^*.

5.4.5 Results

5.4.5.1 TEST SET 1: Averaging Volume and Turbulence Closure

This initial set of tests aimed to identify an appropriate averaging volume over which to calculate the turbine coupling parameters C_T^* and C_P^*. These tests were performed without bottom friction and both methods of turbulence closure.

Averaging volumes with horizontal dimensions (*dx*) of 40, 20 and 10m were used. The vertical dimension (*dz*) was specified either as the turbine height, 10m, or the water column height, 50m.

From the results of the CFD model, the turbine parameters have the values:

- Thrust force *T*=313,952 *N*
  - C_T^* = (1.035, 1.218, 1.661) for *dx*=(40,20,10)*m*.
- Power *P*=642,375 *W*
  - C_P^* = (0.762, 0.972, 1.549) for *dx*=(40,20,10)*m*.

The ocean model is discretized with square elements in the horizontal direction with edge lengths of Δx=40,20, or 10m. In the vertical dimension, the discretization is a depth-average (2d), or Δz=5m or *dz*=2.5m (3d). For the convergence tests, 10, 20, 40, and 80 layers were used, corresponding to Δz=5m, 2.5m, 1.25m, and 0.625m. In addition, vertical viscosity, A_v, was approximated in 3 ways: a constant, moderately large value A_v=0.1; a constant, relatively small value A_v =0.01; and with the use of a k–ε turbulence closure sub-model that is appropriate for coastal ocean spatial scales.

The results of this Test Set are summarized in Table 5-2 to Table 5-4, where the power calculated by the ocean model, P_{ocn} is compared to the power calculated with the CFD model, P_{CFD}. An accurate estimate of power indicates that the ocean model has successfully reproduced the correct volume average velocity. Because velocity appears as U_0^3 in the power equation, a 1% error in *P* represents a 0.33% error in velocity. Hence an accurate estimate for velocity is essential.

Vertical viscosity, turbulent kinetic energy (*tke*), dissipation (*e*), and length scale (*ls*) are shown in Figure 5-2 through Figure 5-5 for locations at the turbine and 500m upstream and downstream.

Table 5-2 - table of 2d results for various averaging volumes with U_0=3m/s.

dx	C_T^*	C_P^*	P_{CFD} **(kW)**	P_{ocn} **(kW)**	***% Diff***
40 m	0.909	0.627	642.4	637.2	-0.8%
20 m	0.940	0.659	642.4	639.1	-0.5%
10 m	0.993	0.716	642.4	624.8	-2.7%

Table 5-3 - table of 3d results, 10 layers, for various averaging volumes with U_0=3m/s.

dx	A_v	C_T^*	C_P^*	P_{CFD} **(kW)**	P_{ocn} **(kW)**	***% Diff***
40 m	0.1	1.035	0.762	642.4	660.6	2.8%
40 m	0.01	1.035	0.762	642.4	650.5	1.3%
40 m	k–ε	1.035	0.762	642.4	653.0	1.7%
20 m	0.1	1.218	0.972	642.4	661.7	3.0%

20 m	0.01	1.218	0.972	642.4	650.4	1.2%
20 m	*k*–ε	1.218	0.972	642.4	656.1	2.1%
10 m	0.1	1.661	1.549	642.4	625.7	-2.6%
10 m	0.01	1.661	1.549	642.4	616.3	-4.1%
10 m	*k*–ε	1.661	1.549	642.4	660.6	2.8%

Table 5-4 - table of 3d results, 20 layers, for various averaging volumes with U_0=3m/s.

dx	**A_v**	**C_T^***	**C_P^***	**P_{CFD} (kW)**	**P_{ocn} (kW)**	**% Diff**
40 m	0.1	1.035	0.762	642.4	649.6	1.1%
40 m	0.01	1.035	0.762	642.4	636.5	-0.9%
40 m	*k*–ε	1.035	0.762	642.4	639.5	-0.4%
20 m	0.1	1.218	0.972	642.4	635.5	-1.1%
20 m	0.01	1.218	0.972	642.4	621.3	-3.3%
20 m	*k*–ε	1.218	0.972	642.4	629.7	-2.0%
10 m	0.1	1.661	1.549	642.4	572.3	-10.9%
10 m	0.01	1.661	1.549	642.4	557.7	-13.2%
10 m	*k*–ε	1.661	1.549	642.4	586.6	-8.7%

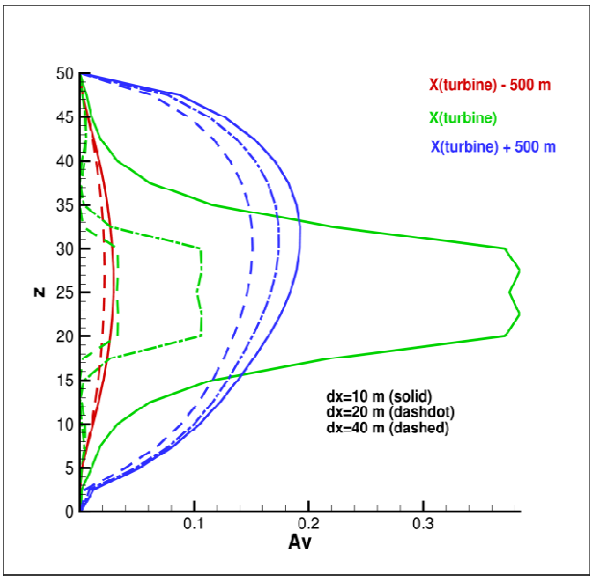

Figure 5-2: Vertical eddy viscosity using k-e turbulence closure.

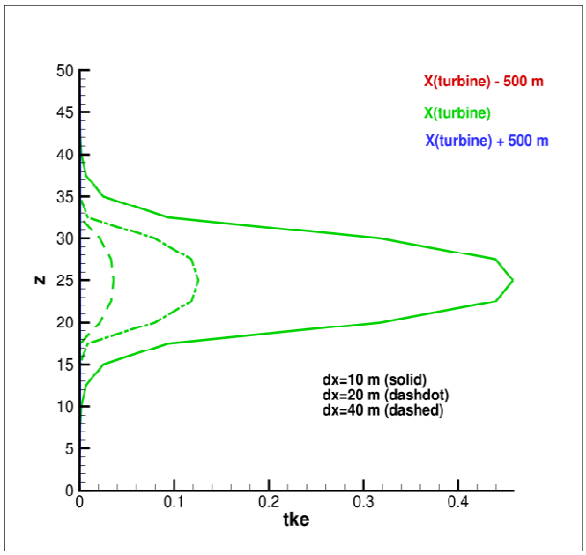

Figure 5-3: Turbulent kinetic energy using k-e turbulence closure.

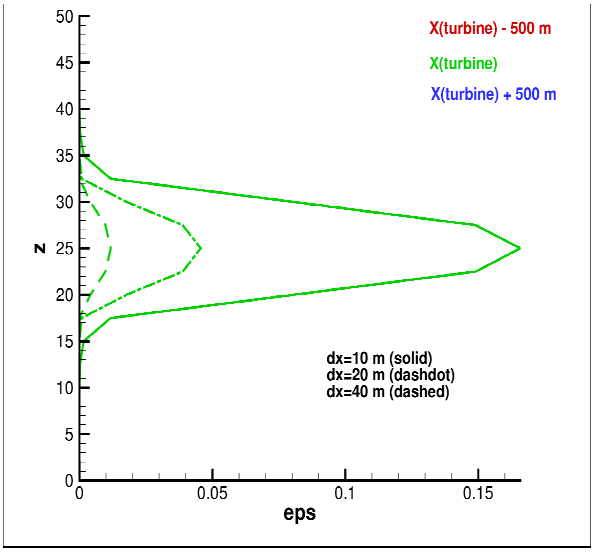

Figure 5-4: Dissipation using k-e turbulence closure.

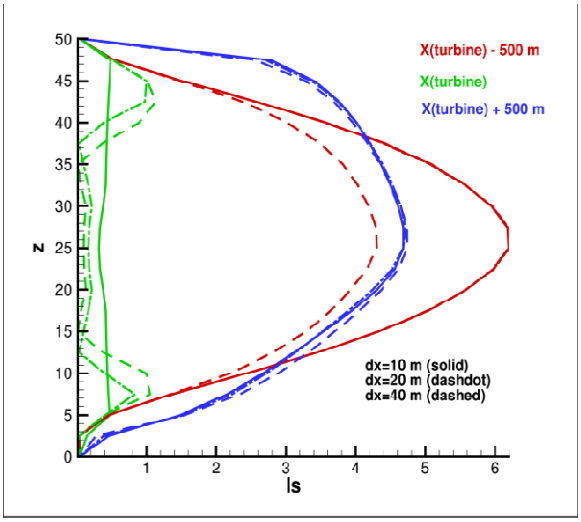

Figure 5-5: Length scale (m) using k-e turbulence closure.

Table 5-5 - convergence for A_v =0.1 m/s²

dx	*Δz*	C_T^*	C_P^*	P_{CFD} *(kW)*	P_{ocn} *(kW)*	*% Diff*
40 m	5 m	1.035	0.762	642.4	660.6	2.8%
40 m	2.5 m	1.035	0.762	642.4	649.6	1.1%
40 m	1.25 m	1.035	0.762	642.4	646.3	0.6%
40 m	0.625 m	1.035	0.762	642.4	645.8	0.5%

Table 5-6 - convergence for k-e closure

dx	*Δz*	C_T^*	C_P^*	P_{CFD} *(kW)*	P_{ocn} *(kW)*	*% Diff*
40 m	5 m	1.035	0.762	642.4	653.0	1.7%
40 m	2.5 m	1.035	0.762	642.4	639.5	-0.4%
40 m	1.25 m	1.035	0.762	642.4	634.2	-1.3%
40 m	0.625 m	1.035	0.762	642.4	631.8	-1.6%

5.4.5.2 TEST SET 2: Averaging Volume and Velocity Variation

The aim of this test set was to assess impact of increasing the vertical averaging dimension from 10m to 20m and to assess the accuracy of the coupling methodology at a range of flow speeds. In this set of results for this test case, the calculation of power is compared for averaging volume heights of 10*m* (turbine diameter) and 20*m* and spanning the range of flow velocity (1, 3, and 5m/s). These tests were performed without bottom friction and both methods of turbulence closure.

For this Test Set, averaging dimensions of 40, 20 and 10m in the horizontal (*dx*) and 10, 20 and 50m in the vertical (*dz*) were used. The water depth is given by *H*. Where *dz=H=50m*, the simulation is two-dimensional.

The results from the CFD model, the turbine parameters, are summarized in Table 5-7 and Table 5-8. Note that the volume averaged velocity is smaller when the averaging volume is smaller. Hence the trend in the coefficients is an increase in magnitude with decreasing *dz* and *dx*.

Table 5-7 - Values for C_T^* based on different averaging volumes and 3 different velocities.

dx (m)	***U_0 (m/s)***	***dz=10m***	***dz=20m***	***dz=H***
20 m	1	1.285	1.093	0.981
20 m	3	1.285	1.093	0.981
20 m	5	1.285	1.093	0.981
40 m	1	1.085	1.002	0.948
40 m	3	1.085	1.002	0.947
40 m	5	1.085	1.002	0.947

Table 5-8 - Values for C_P^* based on different averaging volumes and 3 different velocities.

dx (m)	***U_0 (m/s)***	***dz=10m***	***dz=20m***	***dz=H***
20 m	*1*	1.019	0.799	0.680
20 m	*3*	1.019	0.799	0.679
20 m	*5*	1.019	0.799	0.679
40 m	*1*	0.790	0.702	0.645
40 m	*3*	0.790	0.701	0.645
40 m	*5*	0.790	0.701	0.645

The ocean model is discretized with square elements in the horizontal with edge lengths of Δx=40,20, or 10*m*. In the vertical dimension, the discretization in the ocean model is a depth-average (2d), or 20 layers where Δz=2.5*m* (3d). In addition, vertical viscosity, A_v, was approximated in 2 ways: a constant value A_v=0.1 and with the use of the k–ε turbulence closure model.

The results are summarized in Table 5-9 and Table 5-10, where the power calculated by the ocean model, P_{ocn} is compared to the power calculated with the CFD model, P_{CFD}.

Table 5-9 - table of 2d results

dx (m)	***U_0* (m/s)**	***C_T^****	***C_P^****	***P_{CFD}* (kW)**	***P_{ocn}* (kW)**	**% Diff**
20 m	*1*	0.981	0.680	24.4	24.8	1.3%
20 m	*3*	0.981	0.679	659.2	652.8	-1.0%
20 m	*5*	0.981	0.679	3050.6	2950.0	-3.3%
40 m	*1*	0.948	0.645	24.4	24.3	-0.8%
40 m	*3*	0.947	0.645	659.2	652.5	-1.0%
40 m	*5*	0.947	0.645	3050.6	2979.0	-2.3%

Table 5-10 - table of 3d results, 20 layers

dx (m)	***U_0* (m/s)**	***dz (m)***	***A_v* (m^2/s)**	***C_T^****	***C_P^****	***P_{CFD}* (kW)**	***P_{ocn}* (kW)**	**% Diff**
20 m	*1*	*10 m*	*k–ε*	1.285	1.019	24.4	25.1	2.7%
20 m	*1*	*20 m*	*k–ε*	1.093	0.799	24.4	25.0	2.3%
20 m	*1*	*10 m*	*0.1*	1.285	1.019	24.4	26.1	6.9%
20 m	*1*	*20 m*	*0.1*	1.093	0.799	24.4	25.1	2.6%
40 m	*1*	*10 m*	*k–ε*	1.085	0.790	24.4	25.0	2.4%
40 m	*1*	*20 m*	*k–ε*	1.002	0.701	24.4	24.8	1.4%
40 m	*1*	*10 m*	*0.1*	1.085	0.790	24.4	26.0	6.3%
40 m	*1*	*20 m*	*0.1*	1.002	0.701	24.4	24.9	1.9%

dx (m)	U_0 (m/s)	*dz (m)*	A_v (m^2/s)	C_T^*	C_P^*	P_{CFD} (kW)	P_{ocn} (kW)	% Diff
20 m	*3*	*10 m*	*k–ε*	1.285	1.019	659.2	637.4	-3.3%
20 m	*3*	*20 m*	*k–ε*	1.093	0.799	659.2	647.0	-1.9%
20 m	*3*	*10 m*	*0.1*	1.285	1.019	659.2	636.2	-3.5%
20 m	*3*	*20 m*	*0.1*	1.093	0.799	659.2	646.1	-2.0%
40 m	*3*	*10 m*	*k–ε*	1.085	0.790	659.2	650.5	-1.3%
40 m	*3*	*20 m*	*k–ε*	1.002	0.701	659.2	654.4	-0.7%
40 m	*3*	*10 m*	*0.1*	1.085	0.790	659.2	660.1	0.1%
40 m	*3*	*20 m*	*0.1*	1.002	0.701	659.2	654.8	-0.7%
20 m	*5*	*10 m*	*k–ε*	1.285	1.019	3050.6	2744.0	-10.1%
20 m	*5*	*20 m*	*k–ε*	1.093	0.799	3050.6	2830.0	-7.2%
20 m	*5*	*10 m*	*0.1*	1.285	1.019	3050.6	2638.0	-13.5%
20 m	*5*	*20 m*	*0.1*	1.093	0.799	3050.6	2814.0	-7.8%
40 m	*5*	*10 m*	*k–ε*	1.085	0.790	3050.6	2864.0	-6.1%
40 m	*5*	*20 m*	*k–ε*	1.002	0.701	3050.6	2926.0	-4.1%
40 m	*5*	*10 m*	*0.1*	1.085	0.790	3050.6	2861.0	-6.2%
40 m	*5*	*20 m*	*0.1*	1.002	0.701	3050.6	2924.0	-4.2%

5.4.5.3 TEST SET 3: Bottom Friction

In all the results thus far, we have used the setup for a simple channel with no bottom friction. The flow is then uniform over the cross section. However, in a coastal ocean environment the flow is in the form of a tidal boundary layer where the velocity increases rapidly from the bottom and is more uniform in the upper water column. The actual shape of the velocity profile depends on both the magnitude of bottom stress and the vertical variation in turbulent viscosity. When the viscosity is constant, the problem has an analytical solution with a parabolic variation in velocity. We consider the constant viscosity case first before we introduce the complications with differences in turbulence closure between the CFD and ocean model.

A constant velocity of 3m/s is used. For the constant viscosity case, the vertical viscosity is specified in both the CFD and ocean model as $A_v=0.1m^2/s$ and $u_*^2=\tau_b/\rho=C_b u_b^2$ With $C_b=0.01$ and $u_b=1.344m/s$ (from the ocean model), $u_*=0.1344m/s$ and $\tau_b=18.06336Pa$. Later, the *k*–ε turbulence closure of each model is used to calculate A_v.

For this Test Set, horizontal averaging dimensions (*dx*) of 40, 20 and 10m were used with vertical averaging dimensions of 10, 20 and 50m. The results from the CFD model are summarized in Table 5-11.

Table 5-11: Values for C_T^* and C_P^* based on different averaging volumes..

dx (*m*)	*dz* (*m*)	C_T^* (A_v=0.1)	C_P^* (A_v=0.1)	C_T^* (*k*–ε)	C_P^* (*k*–ε)
10	10	1.612	1.516	1.567	1.452
10	20	1.287	1.081	1.237	1.019
10	50	0.996	0.736	0.995	0.735
20	10	1.212	0.988	1.209	0.984
20	20	1.123	0.882	1.094	0.847
20	50	0.949	0.684	0.952	0.687
40	10	1.050	0.796	1.057	0.805

40	20	1.047	0.793	1.024	0.767
40	50	0.925	0.658	0.929	0.663

The ocean model is discretized with square elements in the horizontal with edge lengths of Δx=10,20, or 40m. In the vertical dimension, the discretization in the ocean model is a depth-average (2d), or 20 layers where Δz=2.5m (3d). In addition, vertical viscosity was taken as a constant value A_v=$0.1 m/s^2$ which is appropriate for coastal ocean spatial scales.

The results for the constant viscosity case are summarized in Table 5-12 where the power calculated by the ocean model, P_{ocn} is compared to the reference power calculated with the CFD model, P_{CFD}. Vertical velocity profiles from the vicinity of the turbine are given in Figure 5-6 (ocean model) and Figure 5-7 (CFD model).

Table 5-12: table of 2d results and 3d results with 20 layers

***dx*(*m*)**	***dz*(*m*)**	**A_v (m^2/s)**	**C_T^***	**C_P^***	**P_{CFD} (kW)**	**P_{ocn} (kW)**	**% Diff**
10	10	0.1	1.612	1.516	655.3	534.3	-18.5%
10	20	0.1	1.287	1.081	655.3	580.3	-11.4%
10	50	2d	0.996	0.736	655.3	633.1	-3.4%
20	10	0.1	1.212	0.988	655.3	620.4	-5.3%
20	20	0.1	1.123	0.882	655.3	635.4	-3.0%
20	50	2d	0.949	0.684	655.3	652.7	-0.4%
40	10	0.1	1.050	0.796	655.3	654.3	-0.1%
40	20	0.1	1.047	0.793	655.3	656.3	0.2%
40	50	2d	0.925	0.658	655.3	659.6	0.7%

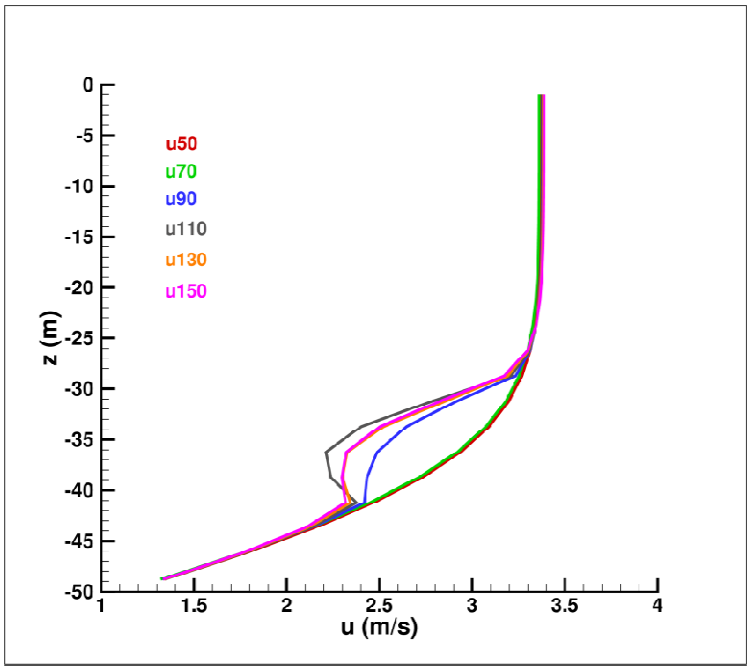

Figure 5-6: Velocity profiles for dx=20m in the ocean model.

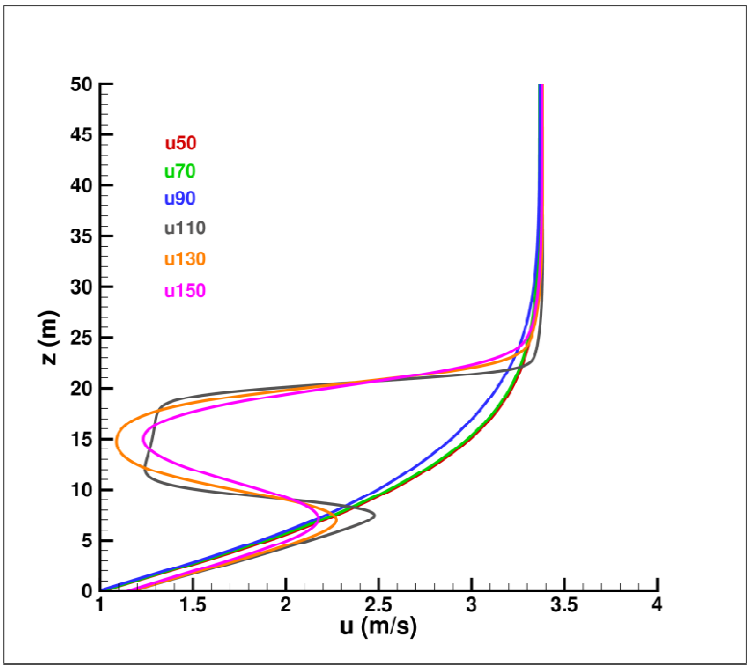

Figure 5-7: Velocity profiles along the centerline in the cfd model.

The results using the k–ε turbulence closure are summarized in Table 5-13. P_{ocn2} indicates power for a simulation including the form drag parameter in the k–ε turbulence closure mode. P_{ocn} indicates power for a simulation neglecting the form drag parameter in the k–ε turbulence closure mode.

Table 5-13: table of 2d results and 3d results with 20 layers

***dx*(m)**	***dz*(m)**	C_T^*	C_P^*	P_{CFD} (kW)	P_{ocn} (kW)	P_{ocn2} (kW)	% Diff	% Diff2
10	10	1.612	1.516	661.8	------	------	------	------
10	20	1.287	1.081	661.8	------	------	------	------
10	50	0.996	0.736	661.8	634.7	------	-4.1%	------
20	10	1.212	0.988	661.8	689.8	------	4.2%	------
20	20	1.123	0.882	661.8	644.6	624.1	-2.6%	-5.7%
20	50	0.949	0.684	661.8	658.3	------	-0.5%	------
40	10	1.050	0.796	661.8	687.8	629.9	3.9%	-4.8%
40	20	1.047	0.793	661.8	664.2	646.8	0.4%	-2.3%
40	50	0.925	0.658	661.8	666.0	------	0.6%	------

Table 5-14: table of 3d results with 80 layers

***dx*(m)**	***dz*(m)**	C_T^*	C_P^*	P_{CFD} (kW)	P_{ocn} (kW)	P_{ocn2} (kW)	% Diff	% Diff2
40	10	1.050	0.796	661.8	680.6	617.9	2.85%	-6.63%
40	20	1.047	0.793	661.8	659.9	642.8	-0.28%	-2.86%

5.4.5.4 Test Set 4: Multi-Turbine Array

The results described here are for an array of three turbines within a simplified channel. The intent is to evaluate the coupling methodology for small arrays. The turbine layout and averaging volumes are shown in Figure 5-8. The turbines are configured in a staggered array with two turbines upstream and one turbine on the centerline downstream. The averaging volumes used here were 50 and 60*m* square cells in the horizontal and either 10 or 20*m* in height.

The results from the CFD model are summarized in Table 5-15 and Table 5-16.

Table 5-15: Values for C_T^* based on different averaging volumes.

***dx*(*m*)**	**U_0 (m/s)**	***dz*=10*m***	***dz*=20*m***
50 m	3	1.545	1.197
60 m	3	1.383	1.136

Table 5-16: Values for C_P based on different averaging volumes.

***dx*(*m*)**	**U_0 (m/s)**	***dz*=10*m***	***dz*=20*m***
50 m	3	1.342	0.916
60 m	3	1.138	0.847

The ocean model is discretized with square elements in the horizontal with edge lengths of Δx=50 or 60*m*. In the vertical dimension, the discretization in the ocean model uses 20 layers where Δz=2.5*m*. In addition, vertical viscosity, A_v, was approximated in 2 ways: a constant value A_v=0.1 and with the use of a k–ε turbulence closure sub-model that is appropriate for coastal ocean spatial scales.

The results are summarized in Table 5-17, where the power calculated by the ocean model, P_{ocn} is compared to the power calculated with the CFD model, P_{CFD}.

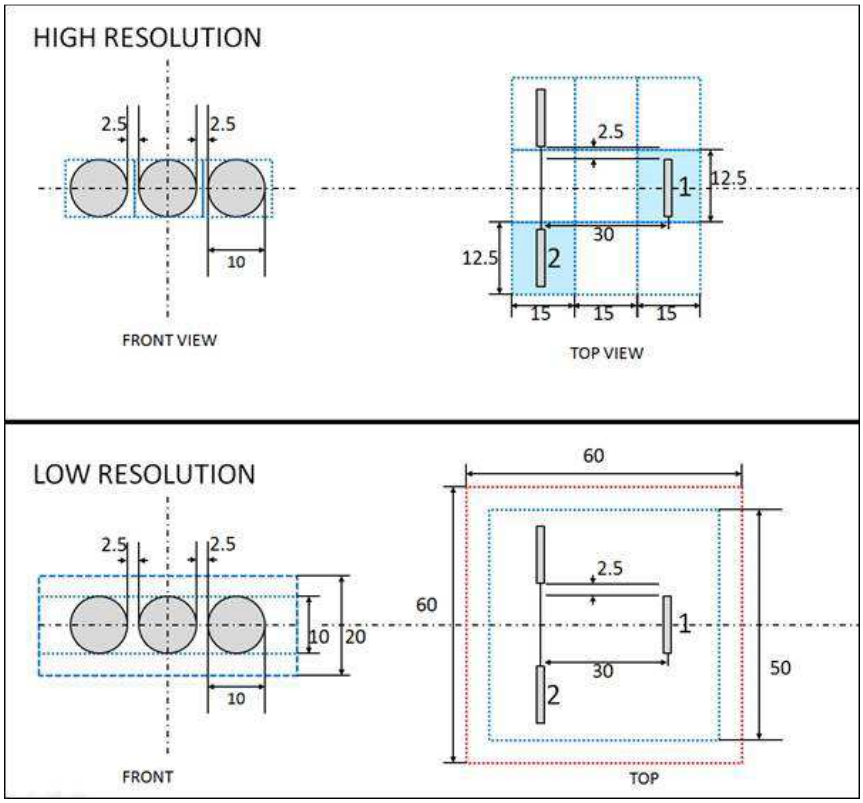

Figure 5-8: Layout for the turbines. Dimensions are in m. *(from Michael Shives)*

Table 5-17: table of 3d results, 20 layers

dx(*m*)	U_0 (m/s)	*dz*(*m*)	A_v (m^2/s)	C_T^*	C_P^*	P_{CFD} (kW)	P_{ocn} (kW)	% Diff
50 m	3	10 m	*k*–ε	1.545	1.342	2018.1	2376.0	17.7%
50 m	3	20 m	*k*–ε	1.197	0.916	2018.1	2149.0	6.5%
50 m	3	10 m	0.1	1.545	1.342	2018.1	2307.0	14.3%
50 m	3	20 m	0.1	1.197	0.916	2018.1	2143.0	6.2%
60 m	3	10 m	*k*–ε	1.383	1.138	2018.1	2329.0	15.4%
60 m	3	20 m	*k*–ε	1.136	0.847	2018.1	2151.0	6.6%
60 m	3	10 m	0.1	1.383	1.138	2018.1	2309.0	14.4%
60 m	3	20 m	0.1	1.136	0.847	2018.1	2094.0	3.8%

5.4.6 Discussion

5.4.6.1 Test Set 1

In general, the most accurate results are for the coarser horizontal resolutions (*dx*=40m and *dx*=20m) and reasonable vertical resolution (20 layers). Typical errors are of the order of 1%. The 2d results are comparable to the more accurate 3d results.

There are a number of reasons why the results using *dx*=10m have poor accuracy. At this resolution, the flow is no longer hydrostatic and governed by the shallow water equations, but is governed by the

Reynolds equations with dynamic pressure included. With the shallow water equations, the only horizontal pressure gradients included are due to the sea surface slope. In reality, a pressure cone develops at the upstream face of the turbine and the pressure gradient forces the flow around the circular face with shear layers at the edges. The shallow water equations simulate this by creating a sea surface slope that diverts the flow around the turbine in a 2d horizontal sense.

In addition, the shear layers are at the edges of the averaging volume with the high resolution (dx=10m). However, this resolution cannot replicate the horizontal stresses accurately. Hence there is insufficient horizontal (and vertical) friction such that the velocity is underestimated and the power is too small.

Of the 3 methods used to specify vertical viscosity, A_v=0.1m/s^2 produces too much vertical friction and the highest estimate of power, and A_v=0.01m/s^2 produces too little vertical friction and the lowest estimate of power. Both of these methods produce wakes that are unrealistically long and extend from the turbine at x=2000m to the outflow exit at x=5000m.

The turbulence closure model produces a more realistic and spatially variable estimate of A_v. Vertical viscosity (A_v), turbulent kinetic energy (*tke*), dissipation (*e*), and length scale (*ls*) are shown in Figure 5-2 through Figure 5-5 for locations at the turbine and 500m upstream and downstream. In the case of the turbulence closure model, the viscosity downstream is much larger than the constant viscosity cases and the wake velocity deficit is reduced by 90% in 500m. Note the length scale in Figure 5-5 where *ls* scales as distance from the wall.

The turbulence model contains a term for production by form drag. The effect of this term is to produce small length scales (Figure 5-5) and relatively small vertical viscosity (Figure 5-2). In this Test Set bottom friction was neglected, so turbulence induced form drag is dominant. Without this term the vertical viscosity is too large and the resultant power is overestimated.

Finally, vertical resolution was increased to examine convergence rate as a function of Δz (Table 5-5 and Table 5-6). With A_v=0.1m/s^2, a constant, the convergence rate is second order. However, with the *k-e* sub-model, the convergence rate is first order.

5.4.6.2 Test Set 2

In the previous test set the height of the averaging volume was the diameter of the turbine. As a result, the estimates for power were sensitive to details of the vertical eddy viscosity because the edge of the averaging volume was at the location of high velocity shear. In essence, the ocean model would need high resolution similar to the CFD model in order to be accurate. However, the ocean model does not have the correct physics at the higher resolution and it is not sensible to replicate the work done by the CFD model. The obvious solution is to increase the size of the averaging volume in the vertical. This set of tests indicates that this approach was more accurate.

In general, the most accurate results are for the coarse horizontal resolution (dx=40m) and reasonable vertical resolution (20 layers). Typical errors are of the order of 1%. The 2d results are comparable in accuracy to the 3d results. These results are also comparable in accuracy to the previous results using a 10m height for the averaging volume.

These results using 20m averaging height tend to be more accurate than the results using a 10m averaging height, particularly for dx=20m. Moreover, they are insensitive to the details of the method

used to calculate vertical viscosity. For these calculations, this is an advantage since the CFD model and the Ocean model use slightly different methods to calculate viscosity.

From a physics point of view, using a 20*m* averaging height removes the non-hydrostatic dynamics and need for high resolution in the shear layers out of the ocean model and places that task in the CFD model. This is reasonable because the CFD model is far more accurate in this domain.

From these tests it appears that a useful averaging volume is a cube with dimensions of twice the turbine diameter on each side. This volume can be increased in the horizontal as necessary to match the element size of the Ocean model. The results with *dx*=20*m* are not as accurate as those with *dx*=40*m* which appears to result from the lack of horizontal friction. The frictional mixing in the horizontal becomes more important as the cell size is reduced.

5.4.6.3 Test Set 3

Constant Vertical Viscosity

For this test case with bottom friction and boundary layer, the most accurate results are for the coarse horizontal resolution (*dx*=40*m*) with typical errors that are smaller than 1%. The 2d results are comparable in accuracy to the better 3d results. For *dx*=20*m* the errors increase to 3% for *dz*=20*m* and 5.4% for *dz*=10*m*. The errors are largest for *dx*=10*m*. These results support the hypothesis made previously that the minimum length scale for the averaging volume must be at least twice the turbine diameter in order to for the calculated power to have reasonable accuracy.

These results can be put in context by adopting a physics point of view and considering the flow dynamics. The ocean model is hydrostatic so the only pressure gradient force is due to the surface gradient. When a form drag is introduced, the flow must be modified to satisfy the continuity constraint. The only way to accomplish this with a pressure gradient force that is constant over depth is to accelerate or decelerate the flow in the entire water column. This leads to a flow that is uniformly increased in the upper and lower water column and in the computational elements adjacent to the element with form drag (see Figure 5-6).

On the other hand, the CFD model contains 2 types of pressure gradient forces: one is the hydrostatic component that drives the flow along the channel and manifests itself as a pressure gradient on the rigid lid, the other is the non-hydrostatic or dynamic pressure that forms a cone upstream from the turbine. When the form drag is introduced, the flow is decelerated across the turbine and forms a jet around turbine (see Figure 5-7). The velocity profiles are then substantially different between the CFD and ocean model.

In comparing Figure 5-6 and Figure 5-7, there is a major difference in the profiles. However, the situation is not as bad as it appears because the velocity is computed differently. In the ocean model, the velocity represents a horizontal average over twice the turbine diameter, 20*m*. For the cfd model, the velocity is a slice taken down the centerline. For a rough comparison, average the centerline velocity in the CFD model with the velocity outside the turbine (u50) to get a value comparable to the ocean model.

These test results reflect the differences in dynamics between the 2 models. In essence, the averaging volume must be sufficiently large to include a substantial part of the flow around the turbine so as to mitigate the differences in the models. Hence the 2d results are always accurate because they include

the entire water column. The least accurate results occur when the averaging volume is restricted in both the horizontal and vertical. By increasing the averaging volume to a large size, the volume averaged velocity approaches the free stream velocity where both models are very accurate.

However, in the real world there is considerable variability in velocity in both time and space. The averaging volume used is then a tradeoff between reducing errors by increasing the volume and increasing the errors due to inadequate resolution of the large-scale flow variations. For the space-scales in these test problems and most coastal ocean problems, dx=20m and dx=40m is probably sufficient to resolve the spatial scales in the ocean model.

k-ε turbulence closure

Except for the 2d simulations, the initial results with the standard k–ε closure model had much larger errors than found in previous results (P_{ocn2} in Table 5-13). On the other hand, the previous results with constant viscosity were quite accurate (Table 5-12). Hence there are significant differences in the closure schemes in the CFD model and the ocean model. After some experimentation, the ocean model results were found to be very sensitive to the formulation of the form drag production term. In this particular scheme, form drag production is added to shear production in both the *tke* and ε equations. This addition results in a larger *tke* and ε in the depth range of the turbine, but a much smaller length scale.

In the power calculation in the CFD model, form drag production is probably not an important factor since the effect is downstream. However, it is a sensitive item in the ocean model due to the volume averages which include both upstream and downstream flows. The ocean model results with no form drag production (P_{ocn} in Table 5-13) tend to be much more accurate except for the 10 m volume height (5% errors). Hence form drag production probably should be ignored in the ocean model for the time being. Then the CFD model and ocean model are consistent in the treatment of this term.

The vertical resolution was increased from 20 to 80 layers in order to evaluate the effect of vertical resolution on the errors. In general, there is a small change in calculated power as a result of small changes in bottom friction. This result indicates that the bottom shear should be adequately resolved; otherwise the resolution in the water column is accurate with 20 layers.

5.4.6.4 Test Set 4

In general, these results for a three turbine array are not as accurate as the power calculations for a single turbine. Typical errors are of the order of 7% for 20m height for the averaging volume and 15% for a 10m height for the averaging volume. The results using 20m averaging height tend to be more accurate than the results using a 10m averaging height, and they are relatively insensitive to the details of the method used to calculate vertical viscosity.

From the previous results for a single disk, a useful averaging volume is a cube with dimensions about twice the turbine diameter on each side or larger. This criterion led to errors of the order of 1% to 2% in power estimates. This volume can be increased in the horizontal as necessary to match the element size of the ocean model.

With the present results, the averaging volume is apparently too small to capture all the dynamical differences between the CFD and ocean model. In this case, the appropriate length scale is the size of

the array rather than the size of a disk as in the previous case. An analysis of the velocity and pressure differences would confirm this hypothesis. Hence, to reduce the errors in power to the range of 1% to 2%, an averaging volume with dx=70 to 140m would be necessary. Unfortunately, this scale is sufficiently large that there may be other problems resolving features in the large-scale flow that is the output from the ocean model.

Further work on array configurations is beyond what can be accommodated in the current project. For future work it is recommended to consider smaller units or building blocks for a larger array. Each of these units would occupy one grid cell in the ocean model. For large uniform arrays, it would make sense to partition the array on lines of symmetry to avoid small-scale features in the CFD model. A test of this would be to examine the 3 disk array used in this Test Set and split it into two averaging volumes divided down the centre of the central disk. Then there would be a right and left volume with half the centre disk and one side disk. If this method is viable, then it would enable simulations of large, regular turbine arrays installed in locations like Minas and Petit Passage. The fence would be partitioned into central parts, which would essentially be repeating unit, and a right and left end part. Unfortunately budget and time constraints require that testing of such a configuration be left for future work.

5.5 SUMMARY AND NEXT STEPS

The results for the different horizontal and vertical sizes of the averaging volume again indicate that the volume should be at least twice the dimension of the turbine in order to maintain accuracy. That is, the volume should average over the differences between the hydrostatic and non-hydrostatic models. Then by passing just two parameters from the CFD model and using the appropriate horizontal and vertical resolution in the ocean model, the effects of the form drag from a turbine and the resulting power output can be calculated with a reasonable degree of accuracy. Typical errors range up to 3%. The general degree of accuracy holds across the velocity range typical for operation of turbines with higher errors at high velocity.

There is no middle ground. Further reductions in the size of the averaging volume lead to substantial errors due to differences in the flow around the turbine caused by formulation differences between the Ocean and CFD model. In essence, the turbine effects must be averaged over a sufficiently large volume or must be fully resolved in order to obtain accurate results.

The only other path is to imbed a highly refined grid within the ocean model grid and perform CFD calculations on the refined part. This is similar to the approach used in the near-field coupling methodology, but with two-way data passing between the models. There are a number of technical impediments to this approach including but not limited to severe loss of efficiency, issues with using one model or two overlapping models, and how to deal with the refinement transition and any overlapping grids. While this approach may be feasible it is outside the scope of the current project.

The k–ε turbulence closure model yields a more realistic and accurate calculation of vertical viscosity and its important horizontal and vertical variations. The k–ε turbulence closure model also produces more realistic turbine wake recovery. However, the results using a k–ε turbulence closure model with a bottom boundary layer (bottom friction) showed significant discrepancies between the CFD and Ocean model. But, by neglecting form drag production, the results could be put into reasonable agreement.

In the ocean model, form drag production is added to shear production in both the *tke* and ε equations. Past experience with form drag in aquaculture arrays has shown that a more accurate approach is to add an additional dissipation term to the *tke* equation. This presents a branching line of inquiry which cannot be pursued within the framework of the current project.

Some tests were performed with multi-turbine arrays. The results indicate that the turbine effects scale with the size of the entire array rather than a single turbine. Hence the averaging volume must be at least twice the size of the array. Depending on the specific problem, this scale may be too large to resolve the large scale flows. A solution may be to use the concept of building blocks of turbines. This involves dividing the arrays along lines of symmetry, then using these planes as walls in the CFD model. The individual pieces would be assembled in the ocean model where the end turbines require special treatment. This concept is similar to the approach used by Ross Vennell [16] where boxes containing the individual turbines were used.

Testing of multi-turbine arrays leads to discussion of blockage effects. This is not believed to be an issue with the ocean model where any distribution of drag and closure is accepted and the flow adjusts accordingly. It is an issue with the CFD calculations however. At high blockage ratios ideal tidal turbine performance can no longer be considered independently; ideal turbine resistance coefficients may be much larger than those predicted by the Betz Limit. This leads into further discussion of independent turbine control within an array as investigated by Vennel [17]. Further research is required to solve these outstanding issues.

The near-field coupling methodology, at its current state of development, is appropriate for simulation of a single turbine or multiple weakly interacting turbines in a tidal flow. The FORCE tidal test facility falls into that later category. In the following Section the near-field coupling methodology is applied to Minas Passage; first using simplified (non-CFD derived) turbine parameters to estimate the total extractable power in the passage, and second, using realistic (CFD derived) parameters to simulate turbines installed at each of the four FORCE test berths.

6 NEAR FIELD CROSS-COUPLING METHOD

This section covers testing of the near-field coupling methodology in the real-world environment of Minas Passage. There are a number of challenges in moving from the simple test channel to a real world test case including the variable current direction and speed, and variable depth. Ideally C_T^* and C_P^* would be fully specified in a lookup table which would require a large number of CFD simulations. In addition, operating conditions would need to be taken into account. However, C_T^* and C_P^* are relatively constant for the maximum power cases presented here so we have adopted single values for this demonstration. Initial testing of the near-field methodology in Minas Passage assumed constant, characteristic values of C_T^* and C_P^*.

6.1 SITE DESCRIPTION

The Bay of Fundy is located on the east coast of North America between approximately 44^o and 46^o N latitude (Figure 6-1). The resonant period of this system is slightly longer than the period of the dominant tidal constituent, M_2, and this area is well known for the large tide range in the upper bay [18] [19]. The node point for the oscillation is near the shelf break east of Georges Bank; however, this is complicated by other resonances parallel to the shelf that extend down to Boston and Cape Cod.

We have chosen to model the entire bay down to Cape Cod and extending offshore for several reasons. When modifying the form drag in the upper bay, the resonance can be altered so that it becomes difficult to specify boundary conditions in a more limited area model. Moreover, previous studies have shown that introducing features such as barrages can modify the resonance and have significant effects on tides as far as Boston [20]. Hence, it seems appropriate to model the entire system.

The particular area of interest here is Minas Basin where the largest tide range occurs, and Minas Passage that connects Minas Basin with the upper Bay of Fundy (Figure 6-2). Minas Basin (and Bay of Fundy in general) contains extensive tidal flats. Model sensitivity tests indicated that treating wetting and drying of these flats accurately is important for attaining accurate model results for velocity amplitude and phase.

The dominant tidal constituent is the M_2 and the amplitude varies from 0.5 m at the open boundary to over 6 m in Minas Basin. In an earlier study, 8 constituents are used in the open boundary conditions– M_2, S_2, N_2, K_2, K_1, O_1, P_1, and Q_1. Most of these constituents are small compared to the M_2 (particularly the diurnal constituents) but were retained in order to assess the accuracy of the model against tide and current observations. The nonlinear interactions between the semidiurnal constituents are important in many situations. The earlier results indicated that this representation of the system was reasonably accurate with constituent amplitude errors of a few cm and phase errors of a few degrees in general.

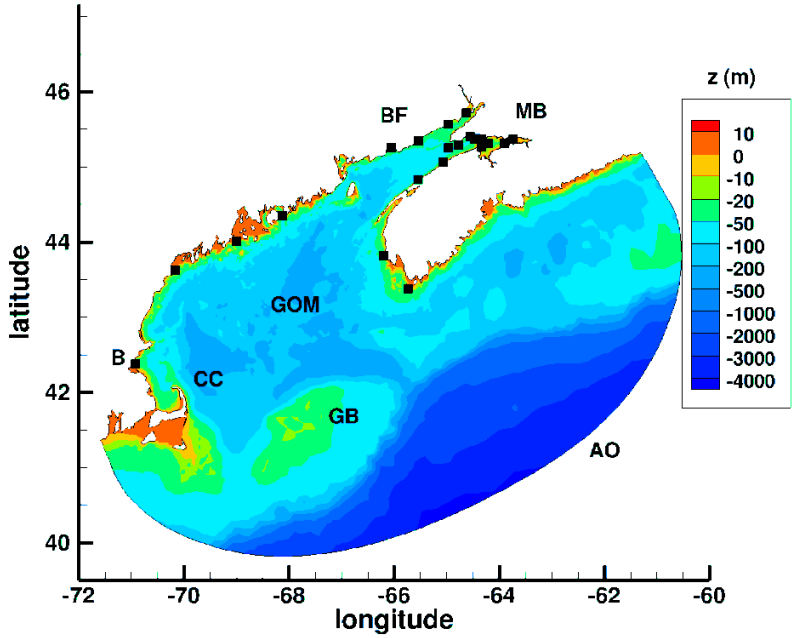

Figure 6-1: Geometry and bathymetry of Bay of Fundy. Sea level observation sites are denoted with a □. AO is Atlantic Ocean, GOM is Gulf of Maine, BF is Bay of Fundy, MB is Minas Basin, GB is Georges Bank, B is Boston, and CC is Cape Cod.

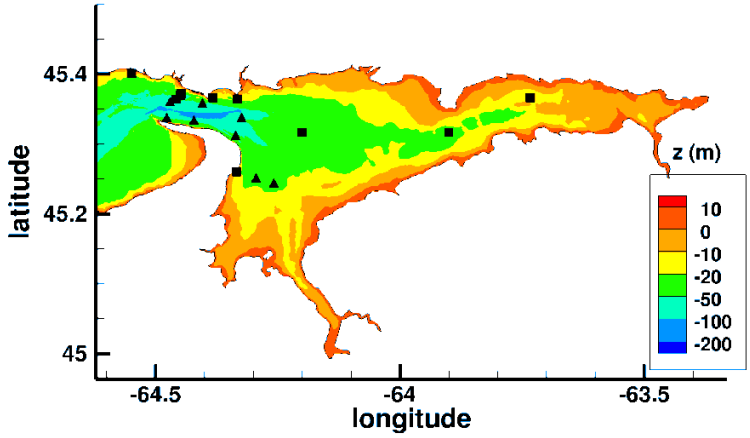

Figure 6-2: Minas Basin and Passage. □, sea level observation sites, Δ, current meter sites.

6.2 Initial Testing in Minas Passage

The first application of the near-field methodology was in a model of Minas Passage using a simple turbine representation. Constant values of C_T and C_P were specified in the calculations and the free stream velocity was approximated as equal to the cell averaged velocity. The goal in this initial work

was to provide an estimate of the maximum extractable power from Minas Passage that could be compared to the analytical relations of Garret and Cummins [21] [22].

A grid was constructed for the coupled Gulf of Maine, Bay of Fundy, Minas Channel, and Minas Basin system. The model is forced with ocean tides form the Atlantic Ocean. The computational grid with depth color contours is shown below in Figure 6-3. Variations of this grid were used by Triton Consultants Ltd to estimate ambient tidal resources in Minas Passage in 2009 and again in 2011.

This work applied the near-field coupling methodology described in Section 5 to represent turbines within Minas Passage. Turbines were applied uniformly across the Passage in a fence configuration and successive runs were performed with increasing turbine drag coefficient until maximum power extraction was achieved. A maximum power value of 5.7GW was found, which compares well to estimates made using the analytical relations of Garrett and Cummins [21] [22]. This work is summarized in a paper published in the Journal of Renewable Energy [23].

The turbines in this work were modeled using a constant turbine thrust coefficient based on a single, isolated device and used empirical relations derived from vegetation experiments to estimate the flow blocking and turbine interactions. These empirical relations are less than ideal when attempting to accurately estimate the power available to a small turbine array such as the FORCE test site.

The following section examines simulations of the FORCE tidal test facility with turbines installed at each of the four berths, with turbine parameters calculated as described in Section 5.

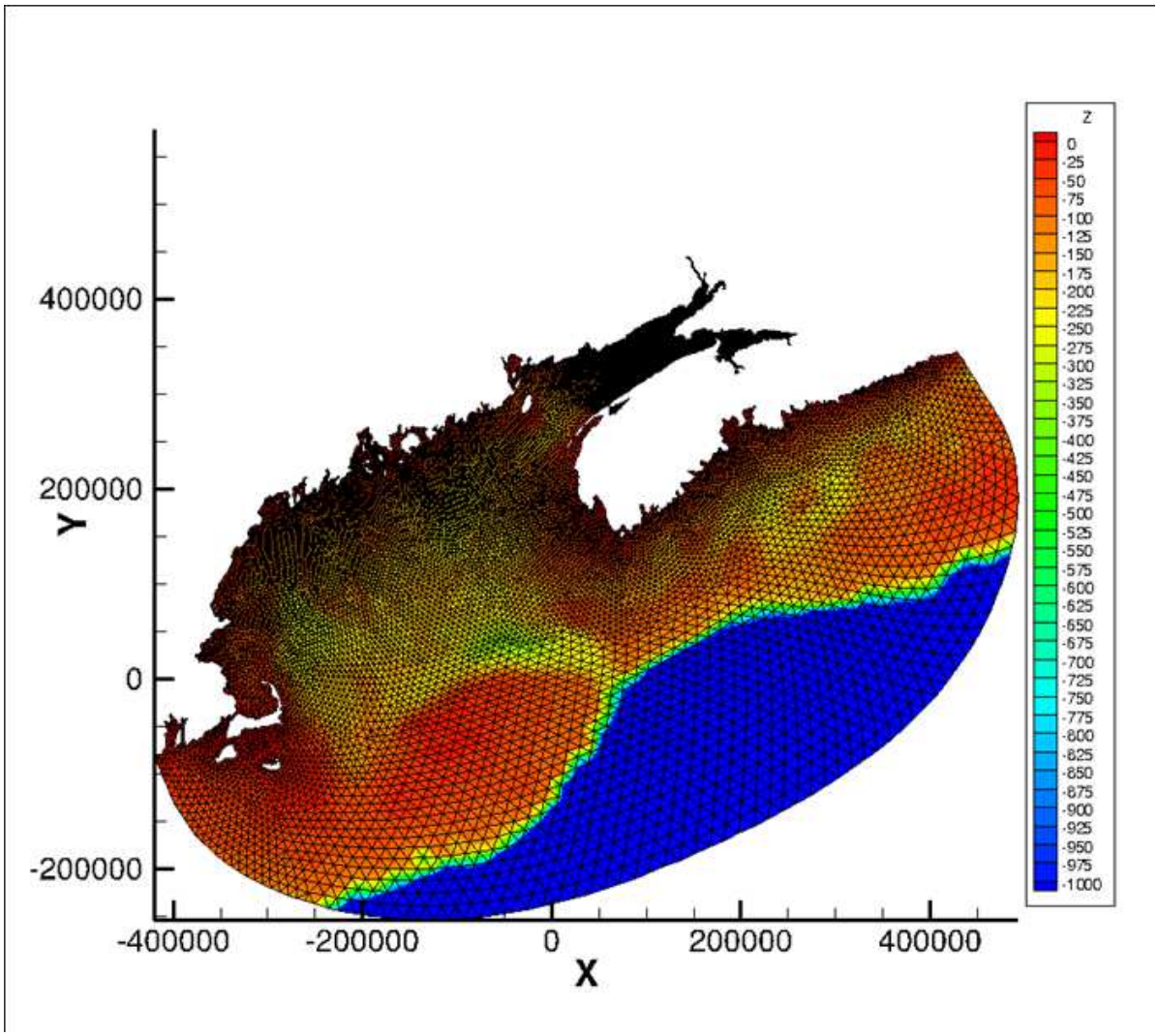

Figure 6-3: RiCOM Model of the Gulf of Maine, Bay of Fundy, and Minas Passage and Basin.

6.3 MODELING OF THE FORCE TEST SITE

In the results presented here, we have extended these methods developed in Section 5 to the field scale problem of four turbines 16m diameter turbines placed in Minas Passage at berths A, B, C, and D of the FORCE test facility (Figure 6-4).

A 200m by 200m horizontal computational grid was created for each site and extended in the vertical from mean sea level to the bottom defined by bathymetric data. For the CFD model, this became the 3-dimensional computational domain and was refined in all 3 dimensions.

Bathymetry in both models was specified based on multi-beam measurements made by the Department of Oceans and Fisheries and Partners in 2007 [24]. Over the course of this project we were made aware of more a more recent multi-beam survey of the FORCE site at 40cm resolution conducted by Seaforth Engineering. The two data-sets were compared over a 40,000m^2 area around each berth. Indeed the newer survey provides increased resolution, but the difference between the measurements is small at an

rms difference of approximately 0.5m. Since 5m resolution is more than adequate for this work, the 2007 measurements were retained.

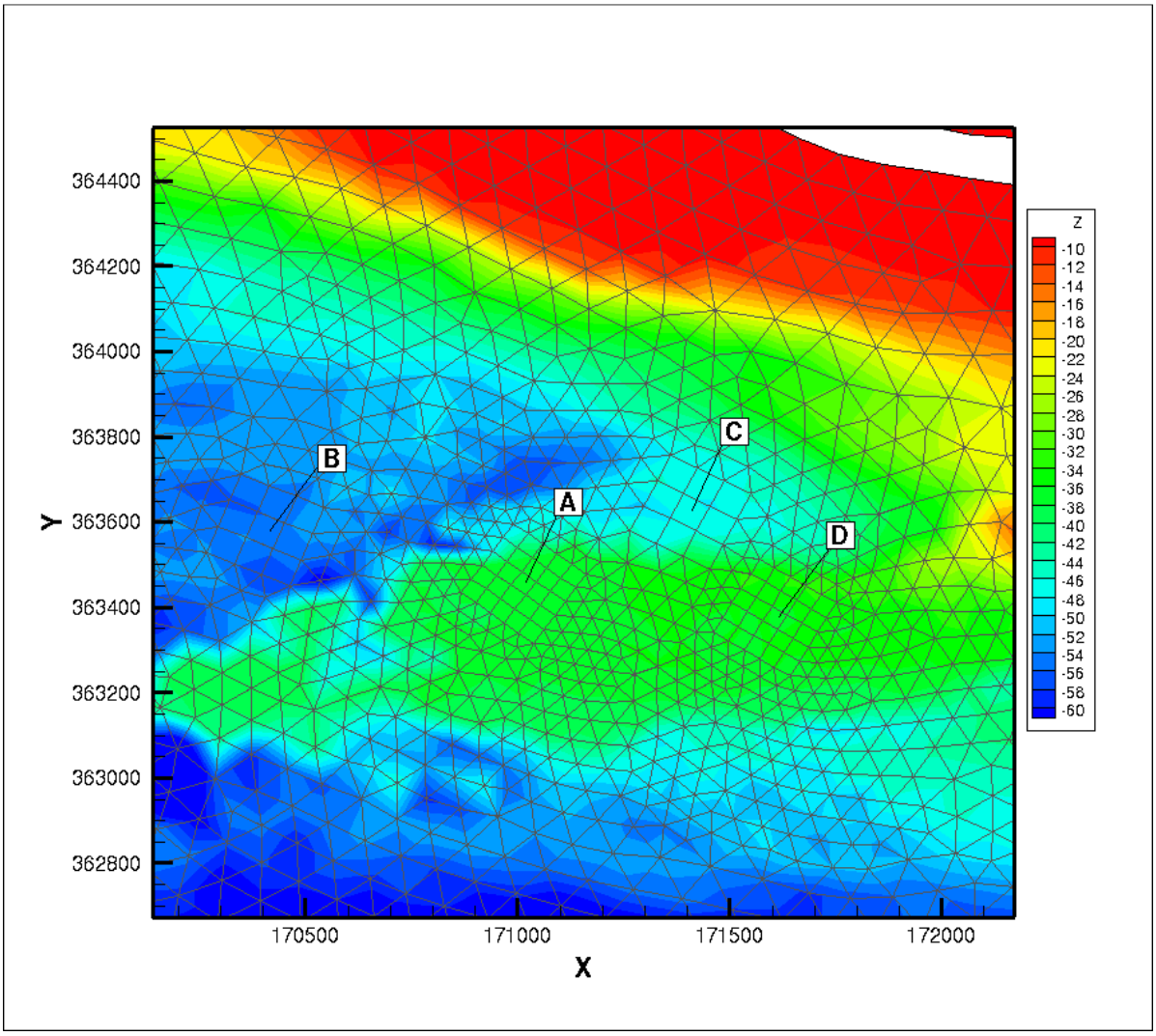

Figure 6-4: Computational grid with colour contours around FORCE test site.

For the Ocean model, each sub-grid was refined to a 3 by 3 (2 deep water sites, B and C) or a 5 by 5 grid (2 shallow water sites, A and D). The computational element sizes were then 66.67 m and 40 m which defined the horizontal averaging dimensions for the CFD model results. Each sub-grid was rotated such that the x axis was parallel to the direction of maximum flood velocity. The sub-grids were inserted into a refined version of the grid used in the initial study of the Bay of Fundy study.

Finally, the ocean model was run with the M_2 constituent until periodic steady state was reached at about 100 hours of simulated time. The maximum flood velocity was extracted on the edges of each 200m by 200m sub-grid and these values were used for boundary conditions in the CFD power calculations.

The CFD model provided a thrust coefficient C_T^* and power coefficient C_P^* that were then used in the ocean model to provide estimates of power for the 4 turbines. To account for non-yawing turbines, power is estimated based only on the component of velocity parallel to the turbine axis.

6.4 LOCAL SCALE CFD SIMULATIONS

The CFD simulations of the four berth sites were conducted by UVic. For each Berth, a mesh was generated with the local coordinate system aligned with the flow direction at the maximum flood condition as determined from previous Ocean-Scale simulations conducted by Cascadia. The bottom boundary was generated from high resolution (5m) bathymetry data [24]. The domain was a square with sides 200m long centered on the turbine location. The height of the top boundary was set based on the water height at the center of the domain for the max flood condition as determined by ocean-scale simulations. The turbine was modeled as a porous disk with the quadratic resistance coefficient C_{R2}^S set to a constant value using K=1.8 and Eq. (**35**).

The disc diameter was 16m for all berths. The mesh spacing was similar to that used for the lab-scale simulations (shown in Table 4-2), but scaled with the turbine diameter.

The applied boundary conditions were as follows;

- **Inlet velocity:** The inlet velocity was specified based on a 2D cubic interpolation of velocity data supplied by the ocean scale model at its node locations along the boundary. The interpolation was done with respect to the lateral position (y) and the height above the bottom (h). (Note that using the z coordinate (depth below chart datum) for the interpolation would have resulted in non-physical velocity profiles between ocean scale node locations due to the irregular bottom geometry.)
- **Inlet turbulence:** The inlet turbulent kinetic energy k and dissipation rate ϵ were set using ocean model output along face-centers. 2D linear interpolation with respect to (y,h) was used for the turbulence quantities.
- **Domain sides**: The side walls of the domain were specified using the *opening* option. The specific conditions set depended on whether or not the ocean scale model had inflow occurring at any point on the boundary. For cases with any inflow, the velocity was set from a 2D cubic interpolation of nodal values produced by the ocean scale model, and turbulence quantities were set using 2D linear interpolation of face-centered values produced by the ocean scale model. For cases with no inflow, the *opening for entrainment* option was used with zero relative pressure, and *zero-gradient* for the turbulence quantities.
- **Outlet:** A pressure outlet with zero relative pressure was specified.
- **Bottom:** The bottom boundary used a specified shear stress instead of attempting to resolve the boundary layer explicitly. This was done primarily to retain consistency with the Ocean scale model. The shear stress was set using a linear interpolation of wall shear stress data from the ocean scale model results.
- **Top:** The top boundary condition was modeled as a fixed, constant height, free slip wall (*rigid lid*). The domain height was set based on the water depth determined by ocean-scale simulations. It was found from ocean-scale simulations that the water height difference across the domain was sufficiently small to justify the rigid lid approach.

The applied boundary conditions were not guaranteed to be exactly compatible with the RANS equations being solved, and in general the typical measures of iterative convergence (max and rms residual values) did not reduce with increasing number of iterations. Instead, the velocity at several points within the domain was monitored and simulations were considered converged when these velocities no longer changed with further iteration. As a second verification of iterative convergence, the max and rms residuals were checked during post processing for a square region with side length 160m centered on the porous disc location (i.e. offset 20m from the inlet outlet and lateral bounds.) Within this region the residuals converged to acceptable values.

The results were post-processed to provide thrust, power, and $C_T^\star, C_P^\star$ based on volume averaged velocities for the ocean scale horizontal grid cell size.

6.4.1 Turbine Parameters

The results from the CFD model are volume-averaged over the horizontal area of a computational element in the ocean model (66.67 m square and 40 m square) and over the depth of the water (2d) or over twice the turbine diameter (3d) in the vertical. The turbine is at the center of the averaging volume.

From the results of the CFD model, the parameters have the values shown in Table 6-1.

Table 6-1: Values for C_T^* and C_P^* for the 4 sites at peak flood. θ is the rotation angle of the sub-grid clockwise from north, dz=H indicates a 2d result.

site	*dx(m)*	*dz(m)*	θ	*T (kN)*	*P(kW)*	C_T^*	C_P^*
A	40	H	126	568.0	989.7	1.031	0.767
B	66.67	H	113	745.2	1501.7	0.988	0.727
C	66.67	H	117	721.6	1424.2	1.002	0.739
D	40	H	121	695.0	1350.5	1.020	0.761
A	40	32	126	568.0	989.7	1.080	0.822
B	66.67	32	113	745.2	1501.7	0.995	0.734
C	66.67	32	117	721.6	1424.2	0.981	0.716
D	40	32	121	695.0	1350.5	1.072	0.821

6.4.2 Ocean Model Setup

The model grid was constructed from unstructured triangles that vary in edge length from 12 km on the open boundary to 40 m at the sites in Minas Passage. In total, there are 69583 vertices and 135101 triangular elements in the horizontal. On a desktop computer, the model runs 60 times faster (2d) and 15 times faster (3D) than simulated time.

In the vertical dimension, the discretization in the ocean model is a depth-average (2d), or terrain following (σ) coordinates (3d). For the 3d results 24 layers were used with increased resolution near the bottom to resolve the bottom boundary layer.

Initially the Ocean model was run with approximate turbine parameter values to provide boundary conditions to the CFD model. The CFD model was then used to recalculate the turbine parameters. The Ocean model was then run again with the recalculated turbine parameters. The results were checked against the first run to determine if further iteration was necessary. In all cases a single iteration was sufficient to achieve converged results.

6.4.3 Results

The Ocean model was run with turbines in both 2d and 3d using the parameters given in Table 6-1. The results for power from the four turbines in each simulation are given in Table 6-2. Figure 6-5 and Figure 6-5 show a time series of along-axis current speed and power for each site (2d). Figure 6-7 shows the currents over the FORCE site at peak flood.

Table 6-2: Turbine power results at peak flood.

Site	*dx(m)*	*dz(m)*	θ	C_T^*	C_P^*	$P_{CFD}(kW)$	$P_{ocn}(kW)$	*% Diff*
A	40	H	126	1.031	0.767	989.7	1117	13%
B	66.67	H	113	0.988	0.727	1501.7	1266	-16%
C	66.67	H	117	1.002	0.739	1424.2	1284	-10%
D	40	H	121	1.020	0.761	1350.5	1397	3%
A	40	32	126	1.080	0.822	989.7	1249	26%
B	66.67	32	113	0.995	0.734	1501.7	1220	-19%
C	66.67	32	117	0.981	0.716	1424.2	1249	-12%
D	40	32	121	1.072	0.821	1350.5	1456	8%

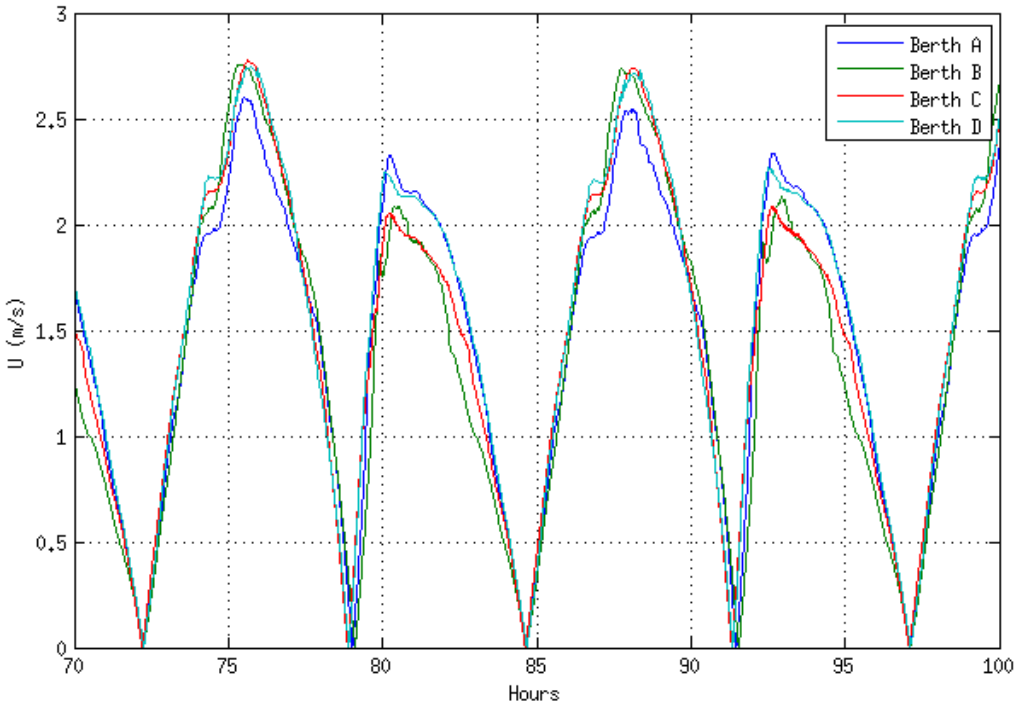

Figure 6-5: Time series of along-axis current speed for the 4 sites in Minas Passage.

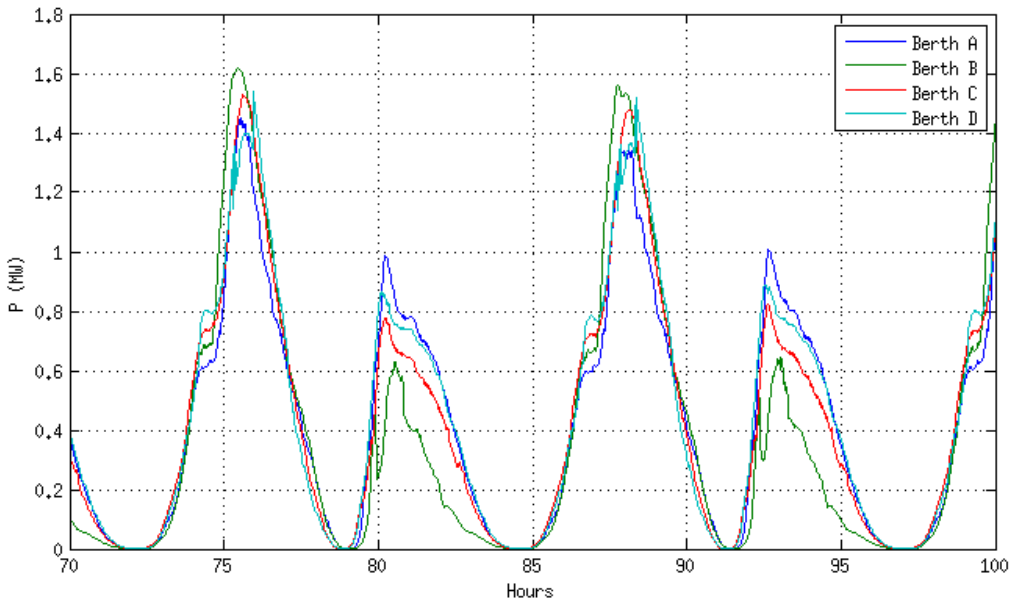

Figure 6-6: Time series of power for the 4 sites in Minas Passage.

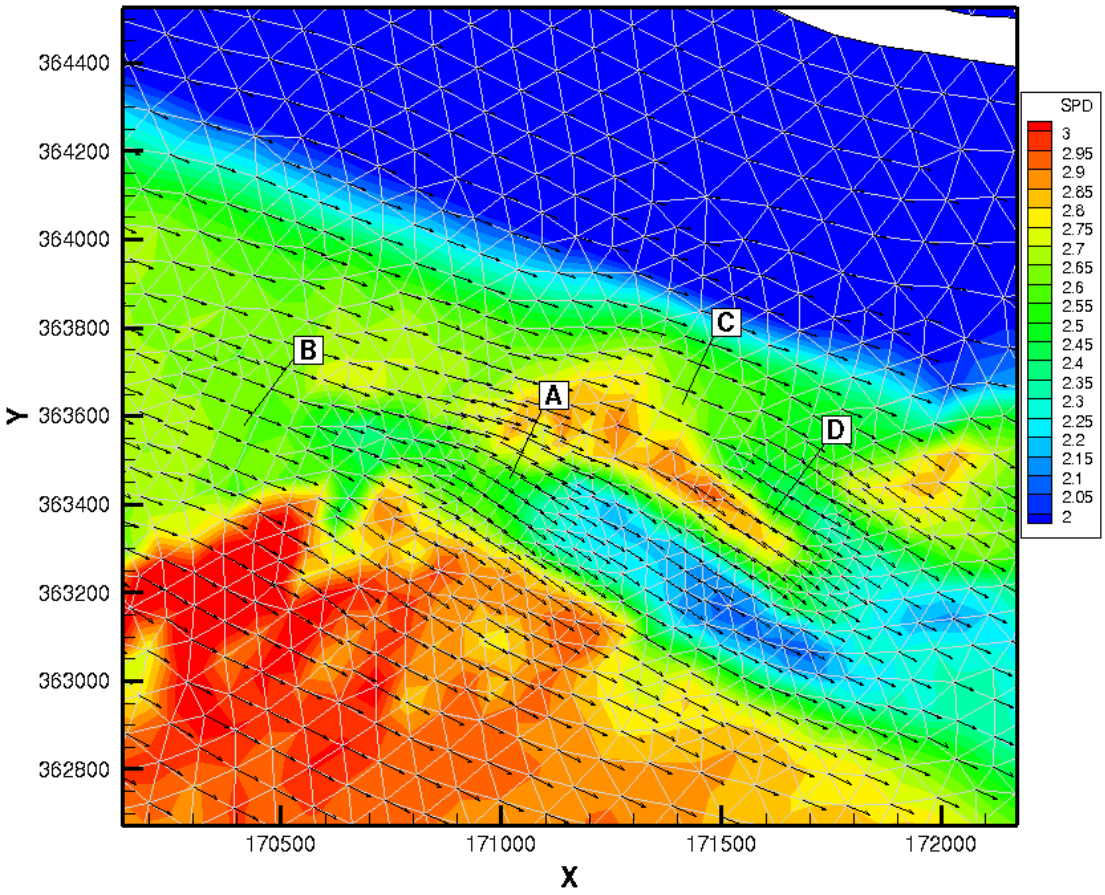

Figure 6-7: Current speed contours and direction quivers at peak flood.

6.4.4 Discussion

The 2d and 3d Ocean model show good agreement, but in general the results for the FORCE tests sites do not show the same agreement between the CFD and Ocean model power estimates that was observed in the simple channel test cases. The FORCE test site scenario tested here is significantly more complex problem than the simplified test channel. The CFD models are driven with boundary conditions derived from the Ocean model, but even within the small sub-domain the models are resolving the flow differently. This is most pronounced at Berth A, where most of the sub-domain sits on a ledge of about 38m depth. But in the north portion of the domain the bottom falls down to about 55m depth. Current speed is highly variable within the sub-domain; even when simulated without the presence of a turbine there is an estimated 10cm/s difference in flow speed across the face of the averaging volume. The different resolutions and physics between the models result in different estimates of the flow field and therefore different estimates of velocity and power at the turbine.

Testing with a range of inlet conditions has shown the turbine parameters C_T^* and C_P^* to be quite stable. This suggests that any discrepancy in the flow field between the CFD and Ocean model will have little impact on the values of C_T^* and C_P^*. The turbine power is much more sensitive to the current speed. The difference in power estimates comes down to the consistency of the calculations in each model. So

the coupling methodology should be considered successful, but the accuracy of the power estimates are of course dependent on the accuracy of the ocean model.

6.5 SUMMARY AND NEXT STEPS

An advantage of the volume-averaging method is that it allows the CFD model to do what it does best in modeling the small-scale flow accurately, and allows the ocean model to do what it does best in efficiently modeling the large-scale flows. For given power conditions, the coefficients C_T^* and C_P^* are relatively constant over a range of current speeds so that the method is robust. A natural extension is to include operating conditions as well and the efficiency of this method becomes more obvious.

For this first iteration, the peak power from the ocean model is less than the power calculated by the CFD model mainly because of differences in how the flow field was resolved within the sub-domains containing the turbines. To achieve agreement in power estimates between the Ocean and CFD models in complex scenarios such as this, further work is required to make the formulation for bottom friction consistent between the models, to modify the turbulence closures to be the same, and to include free surface effects in the CFD model.

7 MID-FIELD CROSS COUPLING METHOD

The mid-field cross coupling method relies on modeling the complex turbulent flow within the tidal channel using CFD. The tidal flow conditions at the entrance and exit of the channel are specified based on far field Ocean model data. The general approach is illustrated in Figure 7-1 for both the case of a channel between two large bodies of water (ex. Petit Passage and Grand Passage) as well as for the case of a channel between open water and a bay (ex. Minas Passage, Digby Gut).

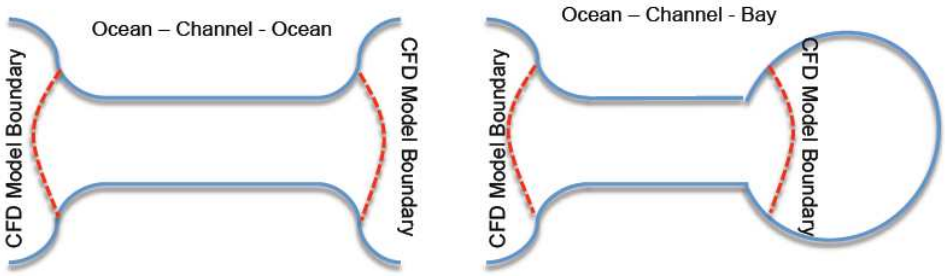

Figure 7-1: Mid field CFD cross coupling method

Upon examination of the flow field for Minas Passage (as predicted by Acadia's Ocean models) it became apparent that a very large CFD domain would be required to capture highly turbulent flow forming near Cape Split during flood tide (shown in Figure 7-2). It was therefore decided that Petite Passage, one of the smaller tidal sites in Nova Scotia, be used as a test case for studying this cross-coupling approach.

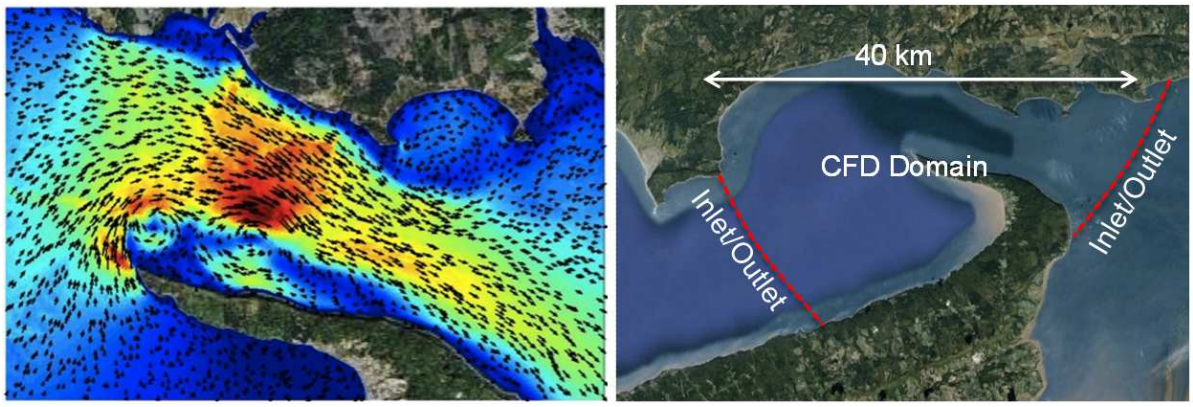

Figure 7-2: Minas Passage, NS: flow speed and direction (left), proposed size of mid-field CFD model (right)

The reversing flows as predicted by Acadia's Ocean models and approximate dimensions for Petit Passage are shown in Figure 7-3.

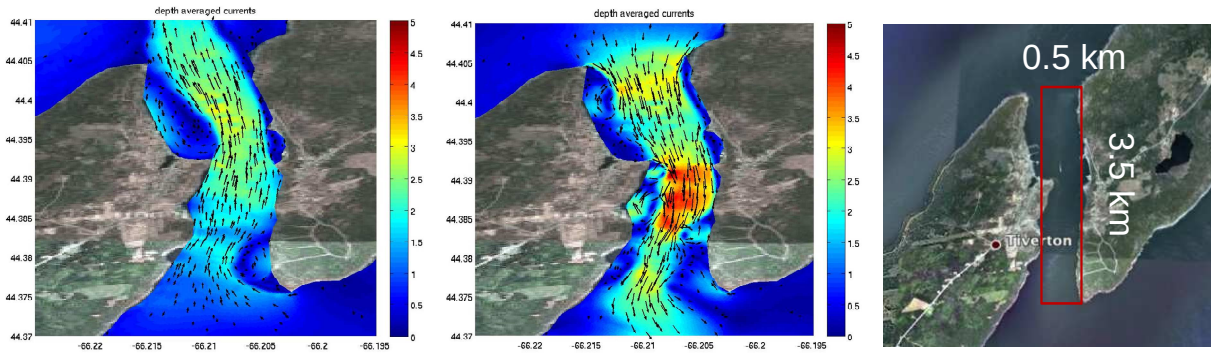

Figure 7-3: Petit Passage, NS

7.1 METHOD

A flow chart summarizing the methodology used to develop a mid-field cross-coupled model of a tidal channel is presented in Figure 7-4. The accuracy of this approach is directly linked to the quality of the bathymetry data available for the site and the accuracy of the Ocean model used to generate boundary conditions for the CFD model. This suggested approach should therefore be considered preliminary as it has only been applied to a single case thus far and has not yet been validated against tidal current measurements taken in the field. The model predictions will become more accurate and the approach much more streamlined as mid-field cross coupling is applied to future tidal sites.

It is also worth noting that over the course of developing a tidal project, the Ocean and CFD models will likely be re-run multiple times as the required level of accuracy increases.

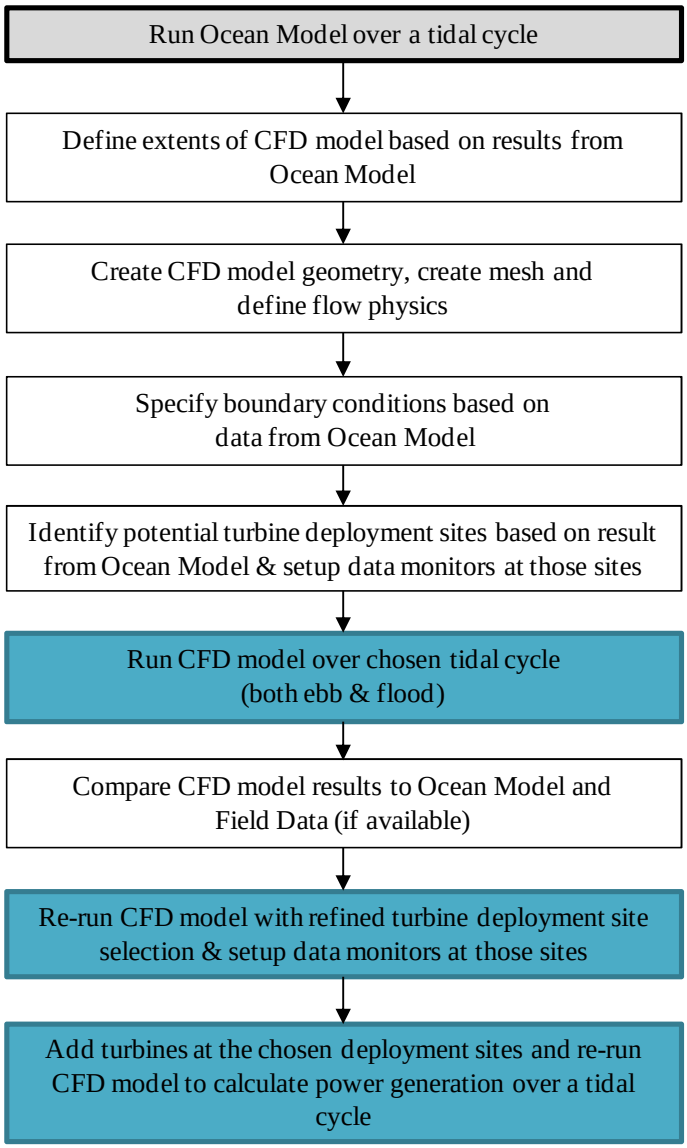

Figure 7-4: Flow chart of mid-field cross coupling approach

7.2 PETIT PASSAGE TEST CASE

Petit Passage was selected as a test case for the mid-field cross coupling. Petit Passage is a tidal channel that flows between Long Island and Digby Neck in Nova Scotia. The passage is roughly a rectangular passage 3.5 km long and 0.5 km wide, with water depths from 20 to 70 m. Acoustic Doppler Current Profiler (ADCP) measurements from the passage have measured maximum currents in excess of 4 m/s. There are regions of flow that are particularly suitable for turbine deployment, with strong bi-directional flow that has relatively low variance in the magnitude and direction of the flow. There are also regions where the bathymetry creates more turbulent flow. It has been estimated that Petit Passage could support turbine arrays with an installed capacity of 13 MW [25] and Fundy Tidal Inc. has been awarded a 0.5 MW ComFIT for the passage. In many ways, the passage is an ideal test site for turbine deployment, and the monitoring and modeling of turbines performance and impact.

7.2.1 Ocean Model

Acadia University has been developed a high-resolution numerical model of the Digby Neck Passages. The numerical simulations are run using the Finite Volume Coastal Ocean Model (FVCOM) [26] using an unstructured grid. The model grid covers the entire Bay of Fundy and Gulf of Maine region, extending out into the Atlantic Ocean beyond the continental shelf. The bathymetry and the coastlines of the passage used in the model were gathered as part of the South West Nova Scotia Tidal Energy Resource Assessment Project (SWNS Resource Assessment) (see [27]). On the open boundary the surface elevation is specified, and the tides throughout the region are allowed to spin up to the observed values. The large domain guarantees that the tidal head across the passages and the flow through the passage develop naturally in response to the local bathymetry and are not strongly dependent on the boundary conditions. As such, this model can be used to determine the boundary conditions for the CFD model described below. The numerical grid has a resolution of about 10 m in Petit Passage (see Figure 7-5). This resolution is sufficient to resolve some of the unsteady flow caused by the changes in bathymetry and coastal features.

Numerical simulations of the flow through the passages were run in both 2D and 3D. The 2D simulations are run over a typical month long tidal cycle. The 3D simulations are run for only a short period of time due to the computational costs of the simulations. The cost of the 3D simulations is strong motivation for the development of the CFD model discussed below.

The results of the 2D simulation were compared to ADCP measurements gathered as part of the SWNS resource assessment. While this comparison and refinement of the model continue, the initial results suggest that the model is capturing much of the behavior of the flow (see Figure 7-5). The simulated flow tends to be too strong and shows larger variation than the ADCP measurements.

The results of the 2D FVCOM simulation was used to produce the boundary conditions for the CFD model described below. And the results of the FVCOM were used to validate the CFD results.

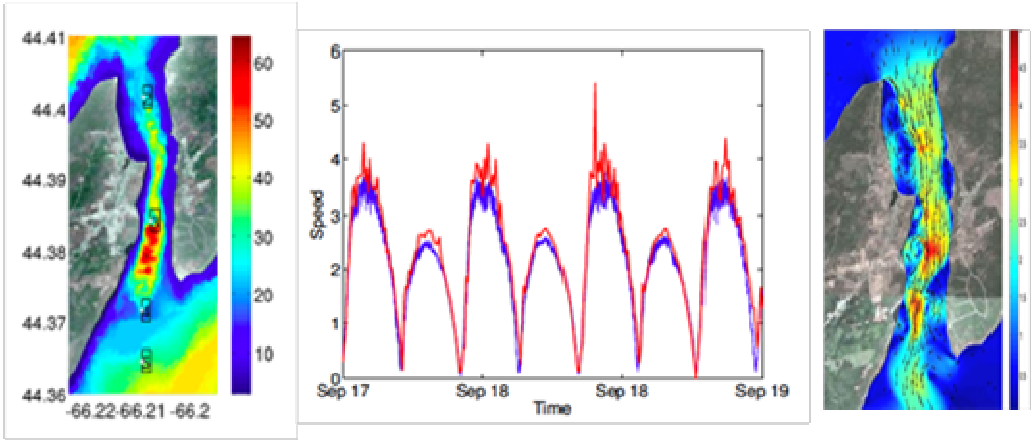

Figure 7-5: Petit Passage Ocean Model. (left) Model water depth in m as used in the model, with the 4 locations of ADCP measurements. (centre) A comparison of tidal current speed at location 3 from ADCPs (blue) and a 2D numerical simulation (red). (right) A snap shot of the flow through Petit Passage from a 2D FVCOM simulation. The colours are the current speed in m/s.

7.2.2 CFD Model

The first step to creating the CFD model was to determine where to place the inlet and outlet boundaries. Flow visualization results from the Ocean models described above were studied to decide how much area to include in the model beyond the channel itself. The initial CFD model created (shown in Figure 7-6a) sought to minimize model extents as the size of the CFD model is directly linked to the computer run time. Simulation results, however, showed that the structure of the flow exiting the channel had a strong influence on the flow through the entire channel. Moreover, having a boundary right at the channel entrance also did not allow the flow to develop naturally. It was concluded that the extents of the model had to be extended further out to more accurately capture the complex flow structures entering and exiting the channel.

A revised model (shown in Figure 7-6b) was subsequently created. This revised model included large areas extending into St-Mary's bay to the south and the Bay of Fundy to the north. The revised model was also created to simulate both ebb and flood tidal flows with a simple reversal of inlet and outlet boundary conditions.

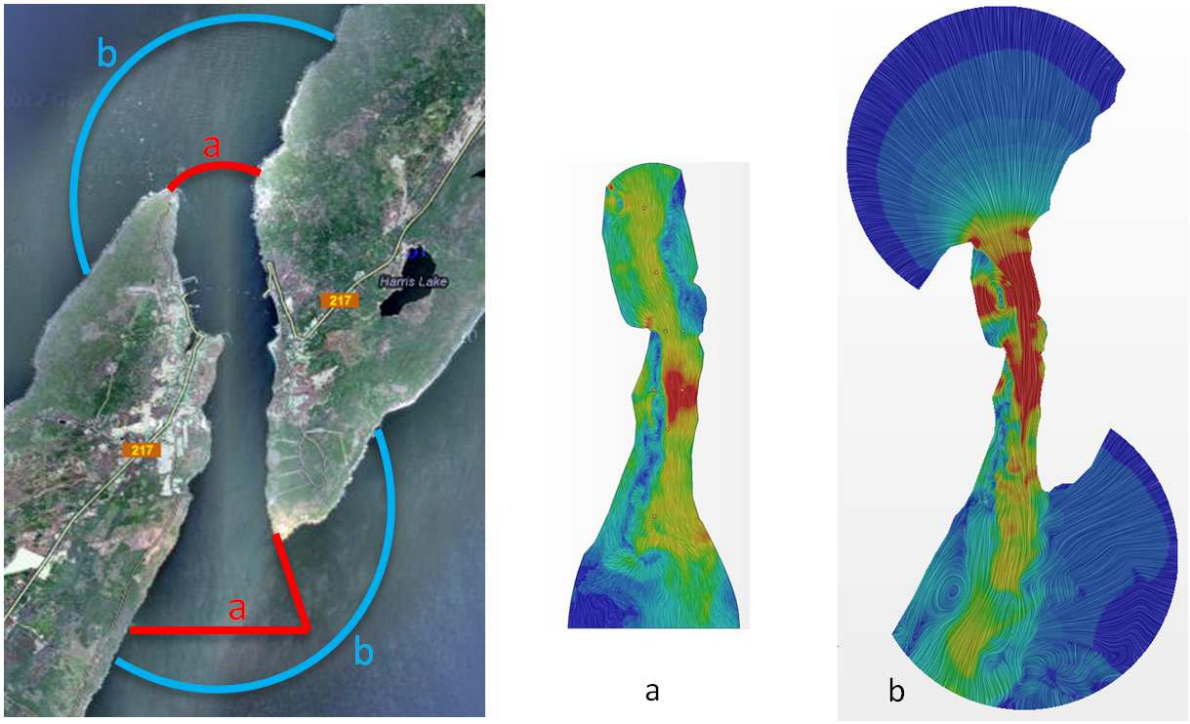

Figure 7-6: Petit Passage CFD model extents. a) Initial model, b) Revised model

The CFD model was created using the same bathymetry data as the Ocean model. The water elevation was fixed at 0m which corresponds to mean sea level in the Ocean model. The air water interface was therefore not modeled. Instead, a slip wall (zero friction) boundary condition was used to model the water surface. This was a necessary simplification because of the very long computer run times that would have been required to model the changing water elevation over a tidal cycle.

The mesh generated for the Petit Passage model is shown in Figure 7-7. Additional mesh refinement was used within the passage to resolve the complex turbulent flows. A maximum grid spacing of 12.5

m in the horizontal direction (x-y) was used in the passage with additional refinement along the shoreline in shallow areas as required. Beyond the channel, the grid spacing was increased to 25 m. The mesh spacing in the vertical direction varied throughout the model depending on the local depth. A cross section of the vertical mesh spacing is shown in Figure 7-7 . The mesh density was increased near the channel bottom to resolve the boundary layer. For reference, the vertical mesh spacing shown in Figure 7-7 is approximately 0.5m near the bottom and 2.5m near the water surface.

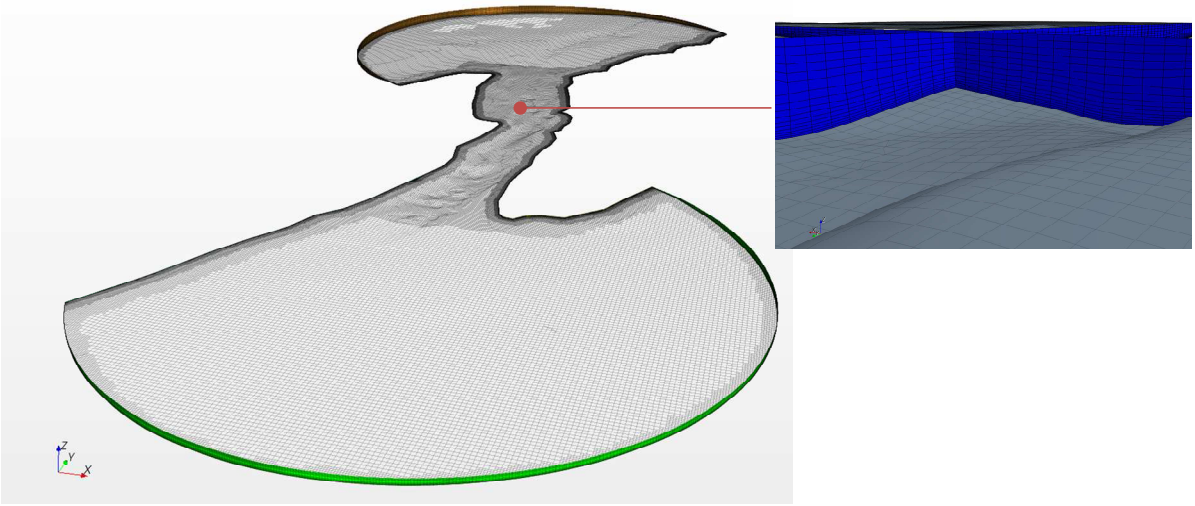

Figure 7-7: Mesh for Petit Passage CFD Model

With the geometry and mesh generation complete, the next step was to define the CFD solver settings and to assign boundary conditions at the channel inlet and outlet. The CFD simulation was run using a number of turbulence models to evaluate model stability, convergence and agreement with Acadia's Ocean model results. The following turbulence models were evaluated:

1. Reynolds Averaged Navier Stokes (RANS) + k-epsilon
2. RANS + Spalart-Allmaras
3. RANS + SST k-omega
4. Detached Eddy Simulation (DES) + Spalart-Allmaras
5. DES + SST k-omega

In terms of boundary conditions, the chosen approach was to specify the mass (water) flow at the inlet boundary using values predicted by the Ocean model. A pressure outlet condition was specified at the channel exit.

The mass flow rate was extracted from the Ocean model over a period of 6 hours (21,600s) when the tide flows from north to south and for an additional 6 hours when the tide flows from south to north. A trend line was fitted through the mass flow data as shown in Figure 7-8 and Figure 7-9. The equation for the trend lines constituted the inlet boundary conditions for the CFD model. Alternatively, a lookup table can be used, but requires addition model setup time depending on software used.

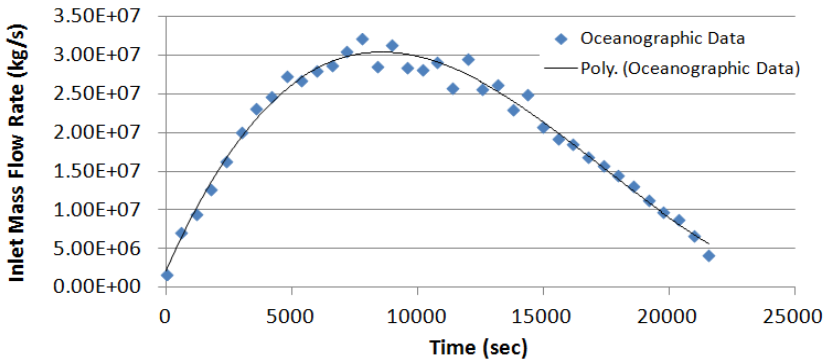

Figure 7-8: Inlet Mass Flow rate predicted by Ocean Model – North to South Tidal Flow

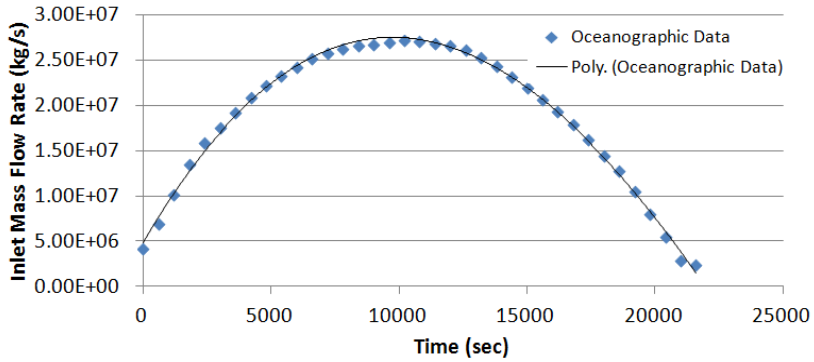

Figure 7-9: Inlet Mass Flow rate predicted by Ocean Model – South to North Tidal Flow

Finally, with the model fully configured and ready to be run, a series of velocity probes were specified throughout the channel to monitor current speeds over the entire tidal cycle (see Figure 7-10).

The model was then run repeatedly to compare results from all five turbulence models listed above. The velocity data recorder for each probe was subsequently plotted over the course of the tidal cycle. The current speeds predicted by the Ocean model were also plotted for comparison.

Figure 7-11 and Figure 7-12 provide a comparison of velocity magnitudes for all probes for a North-South tidal cycle and South-North tidal cycle. In general, relatively good agreement was shown between the CFD and oceanographic simulations. The Spalart-Allmaras based turbulence models showed the largest fluctuations in velocity. They were also the least stable of the turbulence models exhibiting poor convergence.

Since field data was not available for validation (at the time the models were run) it is was not possible to determine which turbulence model produced the most accurate results. The DES + SST model was therefore selected because it is a hybrid modeling approach that combines the strengths of RANS models in the shear layers with Large Eddy Simulation (LES) models in the unsteady separated regions. This decision will need to be reviewed once validation data is available from current measurements in Petit Passage.

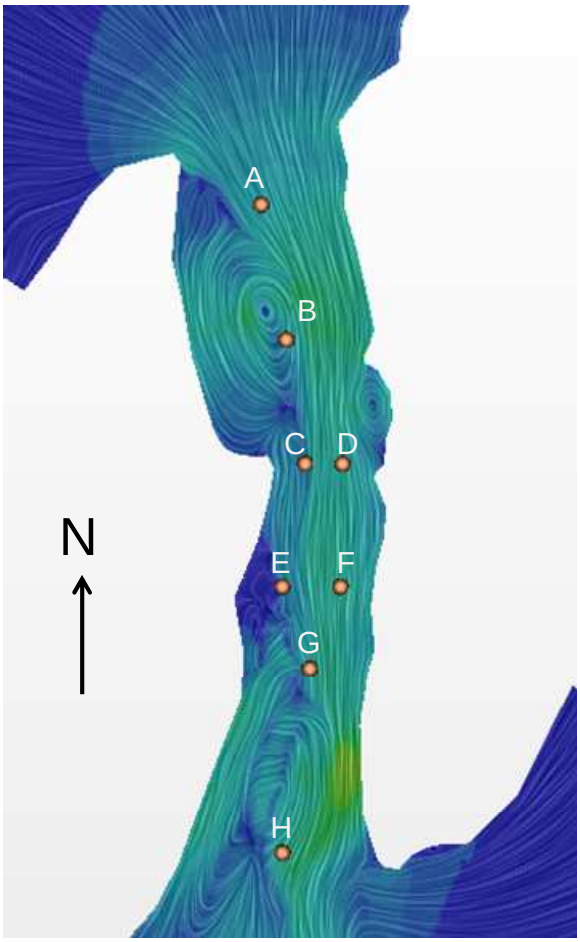

Figure 7-10: Locations selected for velocity probe monitors

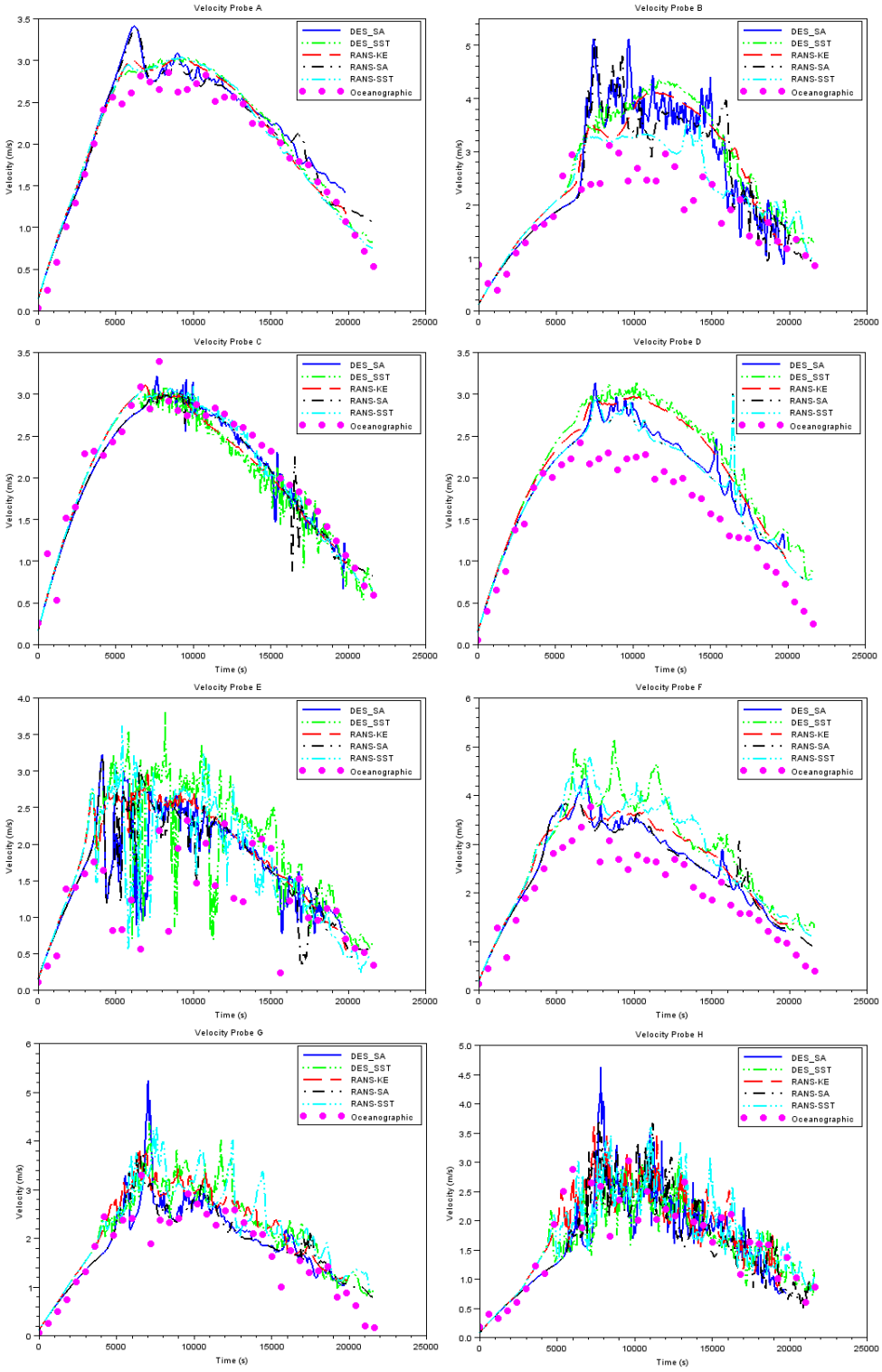

Figure 7-11: Velocity over North-South Tidal Cycle for probes A to H

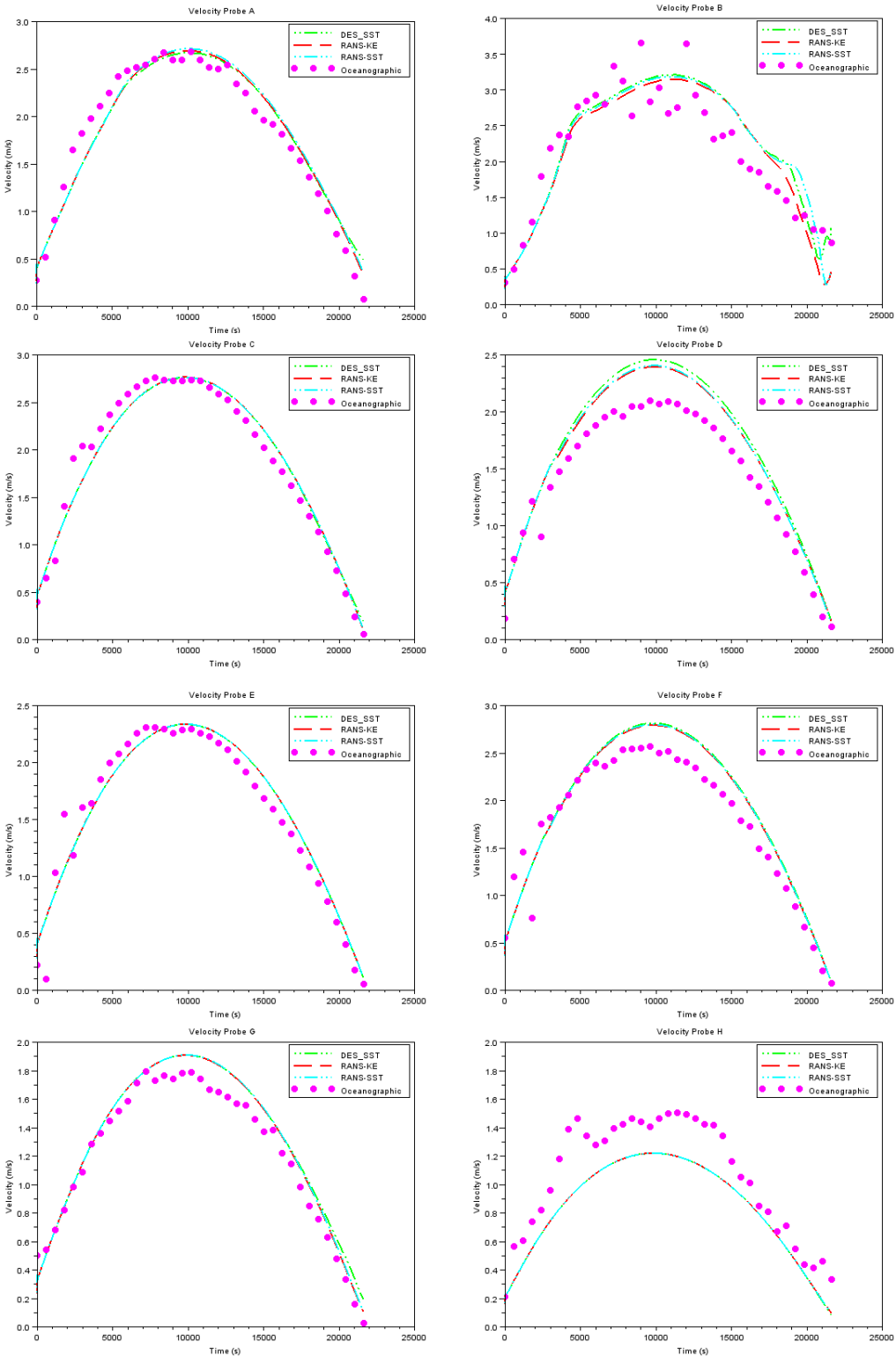

Figure 7-12: Velocity over South-North Tidal Cycle for probes A to H

7.2.3 Selection of potential turbine deployment sites

The primary objective of CFD and Ocean modeling is to enable the project developer and technology provider to select a suitable turbine deployment site. Typical criteria for site selection include:

- Low turbulence levels;
- High capacity factor;
- Flow speeds consistently reaching 3m/s on both ebb and flood;
- Minimize distance to shore (minimize cost of sub-sea cable);
- Minimum variation in incoming flow direction along and 180deg change in flow direction between ebb and flood;
- Added criteria may be imposed related to depth of submergence and minimum draft allowance overtop of the turbine.

For Petit Passage, it was assumed that the turbine would be submerged and requires at least 5 m of draft allowance overtop during low tide to enable safe passage of local fishing vessels.

An animation showing the flow through petit passage as predicted by the CFD simulations was created to help narrow down a suitable turbine deployment site. The animation was created using images showing streamlines and velocity magnitudes along the water surface that were exported every 60s over the course of the 6h simulation for both ebb and flood tides. Snapshots from the videos, provided in Figure 7-13, clearly show that there are areas of clean, fast uni-directional flow as well as large areas in Petit Passage dominated by large turbulent eddies.

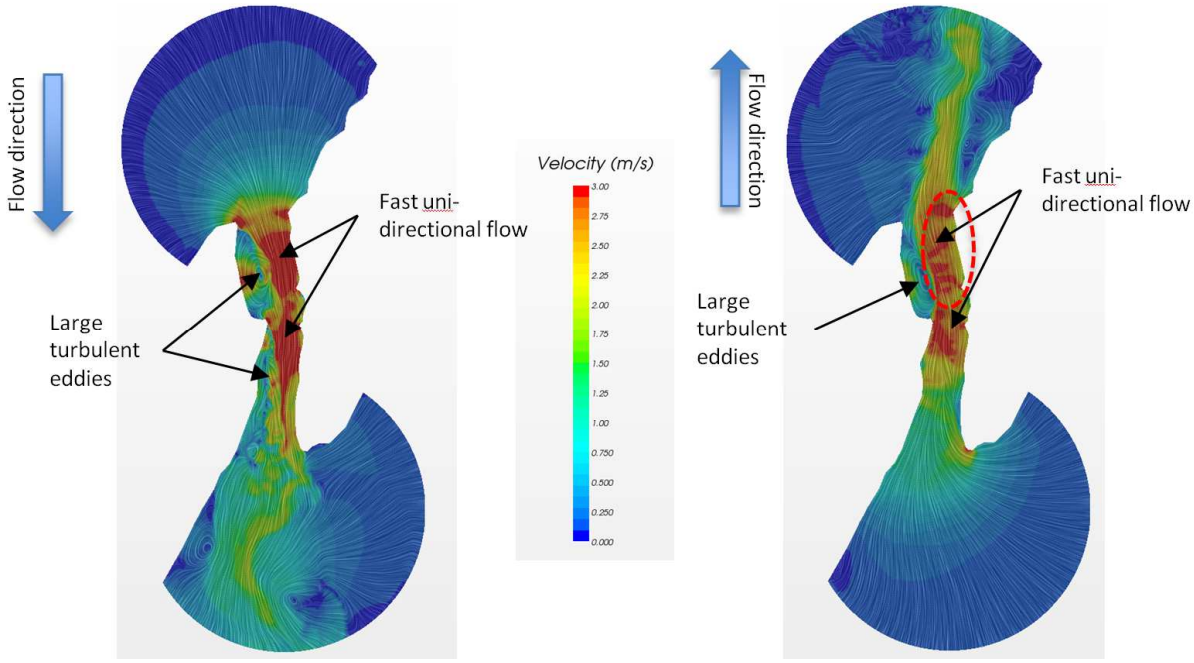

Figure 7-13: Velocity magnitude and streamlines during peak North-South (left) and South-North (right) flow

The simulation results therefore suggest that the east shore of Petit Passage is more suitable for turbine deployment. Based on this information, the bathymetry along the east shore was examined in search of a promising deployment sight that satisfies the general criteria sought by project and technology

developers. As shown in Figure 7-14, the northern half of Petit Passage, especially near the channel entrance, is relatively shallow (approx 30m) and has a more gradual slope leading up to the shore when compared to the southern half. Turbines deployed along the south-eastern shore of the passage would therefore be located in waters up to 60m in depth or on a sloping bottom. While a more detailed analysis of the bathymetry may reveal suitable deployment locations along the south-eastern shore, for the purposes of this project, the north-eastern portion of Petit Passage was selected for further study.

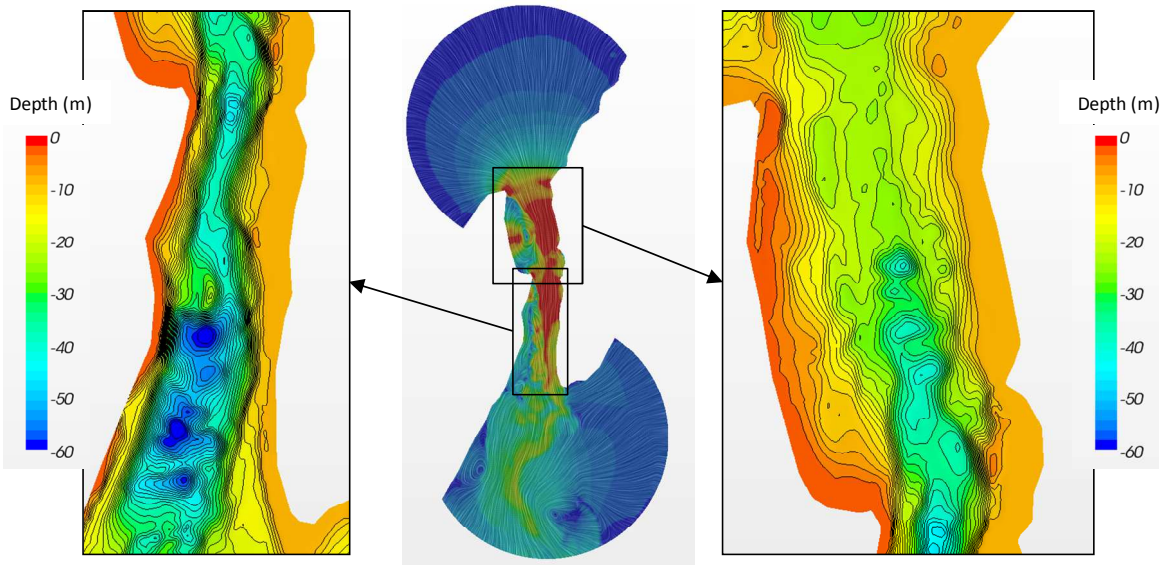

Figure 7-14: Depth Contours for Petit Passage

A series of velocity probes were placed 15m below the water surface along the north east shore of Petit Passage as shown in Figure 7-15. The model was then re-run in both flood and ebb directions in order to select a final deployment location for a turbine.

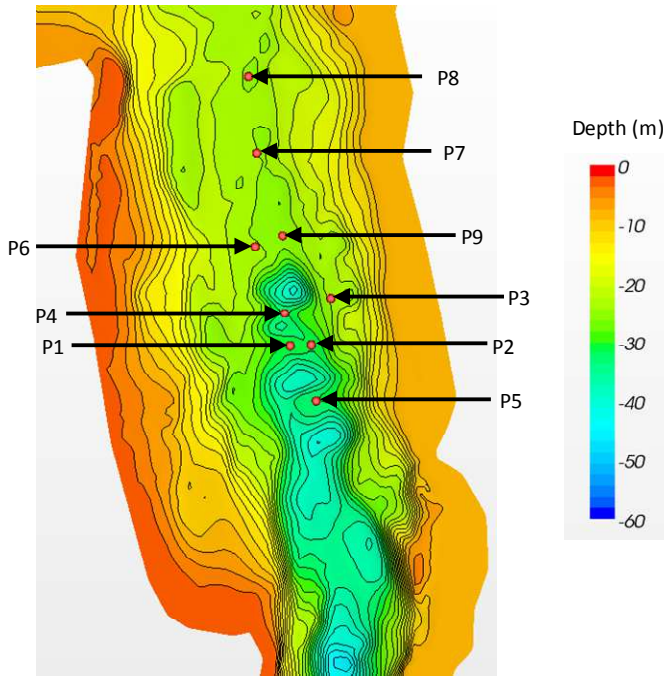

Figure 7-15: Velocity probes placed along north-eastern shore of Petit Passage

The results from the model runs are presented in Figure 7-16 for the North-South flow and in Figure 7-17 for the South-North flow. Both figures show velocity magnitudes measured at each of the points over the course of a tidal cycle. In addition to recording velocity magnitudes, the x and y direction components of velocity were recorded in order to optimally align the turbine to maximum power generation (capacity factor) during ebb and flood tidal flows.

Based on results from these simulations, point P7 was selected as the deployment location for the turbine because the flow at that site exhibited lower fluctuations in velocity compared to other locations such as P1. Point P7 is also located in relatively shallow water (~20m), reaches speeds of 3m/s and is situated on a level shelf which makes it easier for installation of a submerged turbine. In general, the region between points P9 and P8 makes for a promising site for turbine deployment. Final selection should be made by running the model for a range of tidal cycles including a maximum spring tide as opposed to the "typical" case considered for this study. Other factors such as distance to shore for cable laying, bottom composition, turbine specific requirements, etc. will also need to be considered before selecting a deployment location.

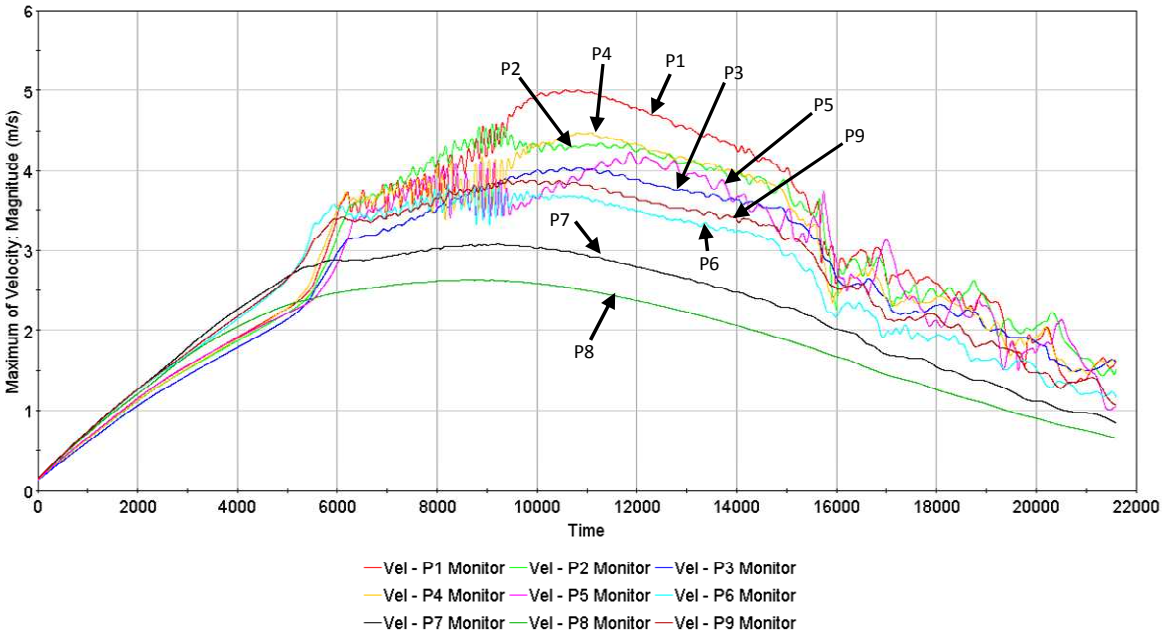

Figure 7-16: Velocity magnitudes for probes P1-P9 for North-South flow

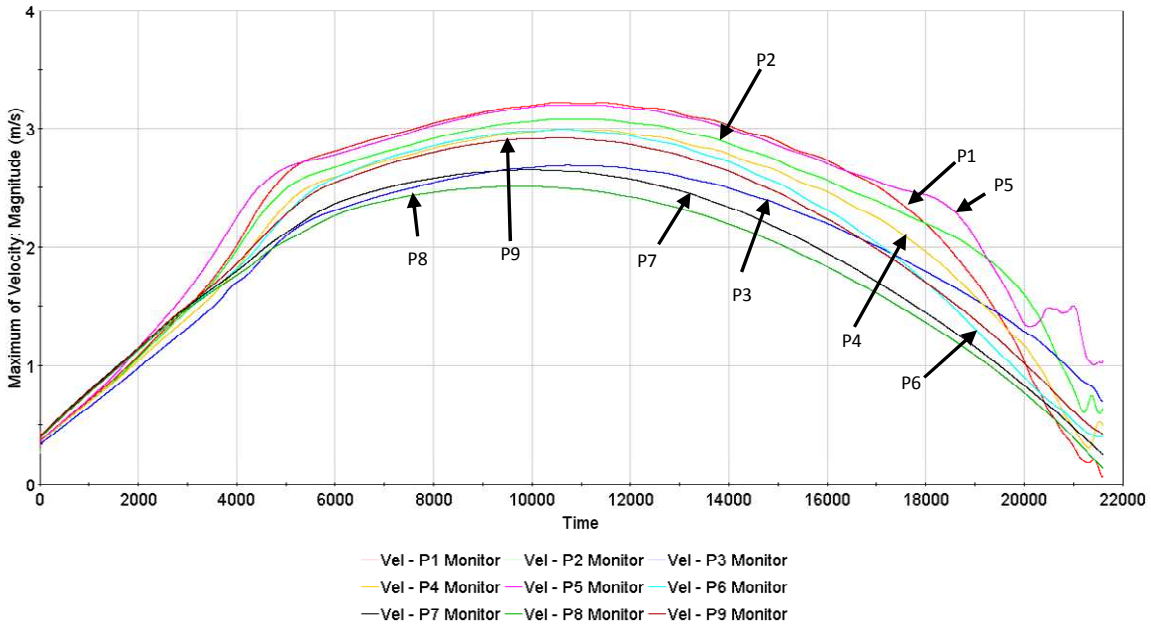

Figure 7-17: Velocity magnitudes for probes P1-P9 for South-North flow

7.2.4 Power prediction by a single turbine over a typical tidal cycle

As a final step, a 10m diameter turbine (modeled as a porous disk) was added to the Petit Passage CFD model. The turbine was placed at point P7, which was identified in the initial Petit Passage simulations as having relatively stable, high speed flows.

To extract the maximum possible power, the turbine should be aligned perpendicular to the flow. The x and y direction velocity vectors at point P7, corresponding to peak current speeds, were therefore calculated for both ebb and flood tidal flows. The optimum turbine orientation for each flow direction was determined from these velocity vectors. Since the ebb and flood flow directions were not exactly 180 degrees apart, the turbine was aligned based on the average between the two optimum orientations. The final disk normal is oriented at 106.42° off of the West vector as shown in Figure 7-18.

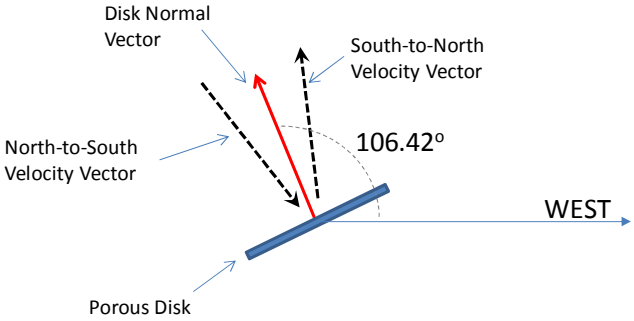

Figure 7-18: Turbine disk orientation for Petit Passage Model

The mesh topology and density on and around the porous disk was based on the flume tank scale simulations described in Section 4. The mesh used for the 10m diameter porous disk is a scaled up version of the final mesh used in the flume tank simulation. Figure 7-19 shows a top view of the Petit Passage mesh used for the North-to-South flow. The refined mesh region containing the porous disk can be seen in the context of the larger Petit Passage mesh. The refined wake region shown in Figure 7-19 also indicates the orientation of the porous disk. A separate mesh was built for the South-to-North flow with the refined wake region located to the North of the disk.

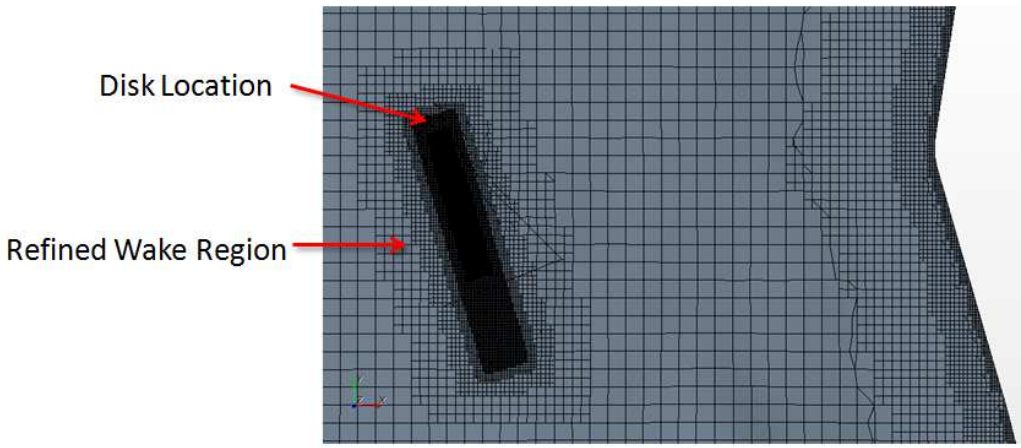

Figure 7-19: Top view of Petit Passage mesh with local mesh refinement around a porous disk. The mesh shown was for the North-to-South flow case.

The porous disk resistance coefficients were tuned to correspond to a C_T of roughly 0.9. The extracted power results for both flow directions are shown in Figure 7-20. Clearly, for a turbine located at point P7, the extracted power is significantly greater when the tides flow from North to South. It is important

to bear in mind, however, that these results represent the amount of power an idealized turbine can extract from the flow and do not take into account turbine specific hydrodynamic or mechanical losses.

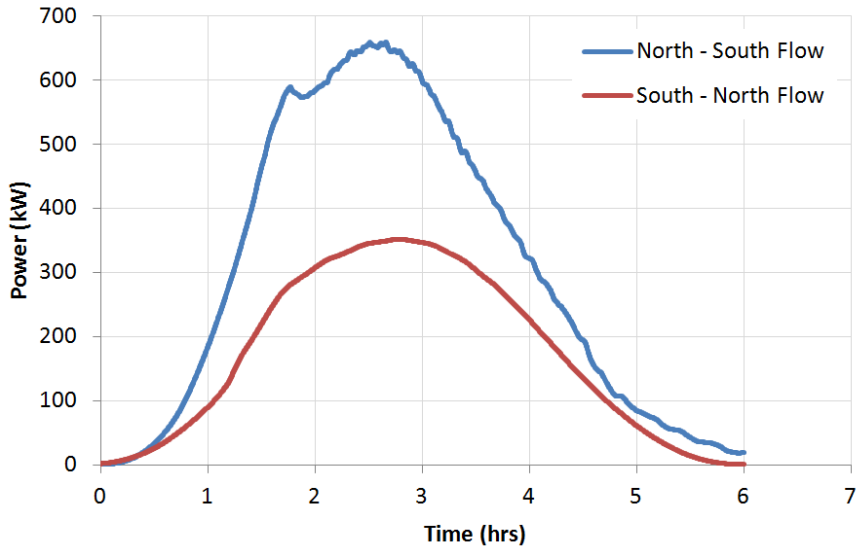

Figure 7-20: Power extracted through porous disk in Petit Passage

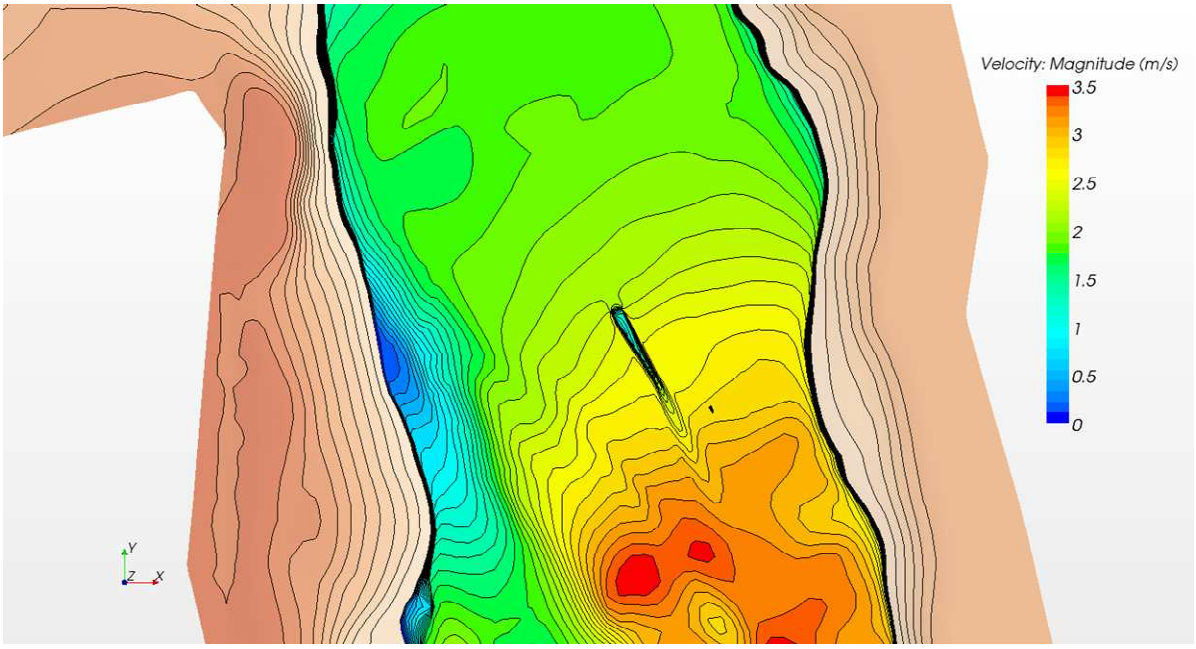

Figure 7-21: Wake shown behind turbine along a plane 15m below water level

7.3 SUMMARY AND NEXT STEPS

A mid-field cross-coupling method was successfully implemented and demonstrated for Petit Passage. In general results from the CFD simulations showed good agreement with Ocean model data, especially

where the flow is relatively uni-directional and not dominated by large eddies. The final set of simulations run with the inclusion of a turbine also demonstrated the potential for using CFD to calculate power extracted by the turbine over a tidal cycle as well as the wake generated by the turbine. This methodology could therefore be extended to modeling tidal farm arrays with inclusion of turbine interaction effects.

At this point, the CFD model of Petit Passage is still considered preliminary because it has not been validated against field data. While ADCP measurements have been completed at several locations in Petit Passage, the data is not yet available for public release.

The next critical step in improving the mid-field cross-coupling approach is therefore to validate the CFD models. The validation work entails:

- Determining if the turbulence model chosen (DES-SST) is in fact the most suitable for modeling tidal flows;
- Mesh sensitivity study to determine if a coarser (or finer) mesh is required to best match ADCP results, especially in terms of vertical resolution;
- Time step study to determine if a time step larger than 2 seconds can be used in order to decrease overall computer time. For reference, it took approximately 24h of computer time to run 6h of real time using 6 processors in parallel. Increase the time step size (provided the simulation remains stable and valid) will make running multiple tidal cycles much more feasible.
- Determine impact of varying the bottom friction specification. For the simulations completed as part of this project, the solver default value for a smooth surface was used to set the bottom friction along the sea bottom. Specifying a roughness will likely impact the vertical velocity distribution by affecting the boundary layer growth. The roughness parameters should therefore be tuned to better match the field data.

Once the validation work is complete, the next step is to determine what impact the assumption of a fixed water elevation (fixed slip wall as opposed to a free air-water interface) has on the accuracy of results for modeling flows through Petit Passage.

For shallow channels experiencing a significant tidal range, a method will need to be developed to capture the changing water elevation. A number of options exist including:

- Creating a series of CFD models with varying depth and running incrementally over shorter durations;
- Modeling the air-water interface (this will significantly increase the computational time), or;
- Using a morphing mesh that allows the water surface to vary over the course of the simulation.

Clearly, significant work remains to standardize the mid-field cross-coupling method such that it can be applied with confidence for a wide range of tidal sites. Notwithstanding, the results to date are very promising and form a solid foundation for future work.

8 CONCLUSIONS

The yearlong project developed novel methods of modeling tidal flows and turbine interactions. When the project was initiated, the bounds of Ocean models and CFD models were not yet understood by the team. To date, the accepted approach by researchers and technology/project developers was to use Ocean models for assessing the available tidal resource and modeling the flow through the channel. The used of CFD models was typically limited to modeling the actual turbine under idealized conditions (straight channel) and for constant water speed.

This project pushed the bounds of both Ocean and CFD models. Attempts were made by the Ocean modelers to refine their models down to the scale of a turbine rotor. Attempts were also made by the CFD modelers to simulate entire channels. Based on these two approaches, the following two types of coupling methods were identified and subsequently applied to tidal passage in Nova Scotia:

1. **Near Field Model:** The Ocean model is used to model the tidal channel. The resolution is refined down to a volume no smaller than 2 turbine diameters in size and relies on the CFD model to provide thrust and power characteristics of the turbine. This method was applied to Minas Passage.
2. **Mid Field model:** The CFD model is used to model the entire tidal channel. The conditions at the boundaries of the channel are obtained from Ocean models that span the entire region. This method was applied to Petit Passage.

In the end, it was found that each modeling approach had its share of strengths and weakness.

The CFD model is likely more effective at resolving complex turbulent flow, 3D flow variations caused by abrupt changes in bathymetry, and turbine array interactions, but (at this point), does not take into account the changing water elevation (free-surface). Including the free-surface will likely make the CFD model impractical for modeling more than a few hours of a tidal cycle due to long computer run times.

The Ocean models on the other hand remain the most effective tool for modeling tidal flows spanning hundreds of kilometers. Promising results were also obtained on the turbine scale demonstrating that Ocean models can be further improved to capture turbine-tidal resource interactions.

Whether a near field or mid-field approach is used therefore depends on factors such as the complexity and scale of the site, if the purpose is for initial site survey or laying out of a tidal array, scale of the project, etc.

The following sections provide more detailed conclusions on each of the tasks completed as part of this project.

8.1 FLUME TANK EXPERIMENTS

The flume scale experiments provided flow-field data and porous disc drag force values that were used to validate CFD simulation. The PIV system also provided very rich flow-field data for a variety of array configurations clearly showing disc interactions and wake recovery.

The disc drag force was measured with a load cell housed in a custom built water-tight shell. It was found that a disc porosity of 50% provided the desired thrust coefficient of ≈0.9 which is representative of a turbine operating at its maximum power output. It was found that the manufacturing process was

repeatable, and different discs of the same design and porosity had sufficiently similar drag characteristics. It was also found that within the range of flow speeds employed, the drag and wake recovery was not sensitive to the Reynolds number (within the experimental uncertainties).

8.2 COMPARISON BETWEEN CFD AND EXPERIMENTS

It was found that the CFD simulations do a reasonable job in predicting the thrust force acting on porous discs in several different array configurations. For all cases considered as part of this project, the thrust was predicted within 8% error. The estimated uncertainty of porous-disc CFD predictions of power relative to physical porous-disc experiments is approximately 12% for all array configurations considered in this report. Note that both CFD and experimental porous disc methods are analogs for real rotors, and both represent ideal turbine power neglecting losses due to blade drag, tip loss etc.

The CFD simulations also did an adequate job predicting the wake recovery behind porous discs, however, significant tuning of turbulence parameters was required to get a good match to experimental data. Generally, the simulated wakes recover too slowly unless sources of turbulence are added at the disc, and even with increased turbulence it appears that larger scale unsteady mixing is at play rather than simply subgrid-scale turbulent viscosity. Furthermore, the turbulence seems to decay too rapidly in the simulations.

The fact that thrust forces for each of the turbines can be predicted with reasonable accuracy and the wake can be tuned will allow site developers to use this simplified method for initial layout of turbine arrays, especially when incorporated into a mid-field cross coupled model.

8.3 NEAR FIELD CROSS-COUPLING METHOD

The approach of the near-field coupling methodology is to imbed individual turbines within the Ocean model as sub-grid, volume-averaged drag elements. The turbine's thrust and power are characterized using CFD and subsequently averaged over an appropriate volume and embedded in the Ocean model. Passing the thrust and power parameters from the CFD to the Ocean model effectively couples the models.

An advantage of this method is that it allows the CFD model to do what it does best in modeling the small-scale flow accurately, and allows the ocean model to do what it does best in efficiently modeling the large-scale flows. The method is especially powerful when the turbines are fully modeled using CFD as opposed to using a porous disk facsimile.

The near-field coupling methodology was initially tested in a simplified ocean-scale test channel of dimension 5km x 1km x50m. This stage of testing identified an appropriate volume over which turbine thrust and power characteristics should be averaged (a cube with side-length at least twice the diameter of the turbine) and issues concerning the compatibility of each model's representation of turbulence and bottom friction. Typical differences in power estimates were small; between the models were 1-3%.

Some simplified channel tests were also performed with a tight packed three turbine array. The results indicate that the turbine effects scale with the size of the entire array rather than a single turbine. In some cases the volume may be too large to effectively resolve the large-scale flow in the Ocean model. Further development was outside the scope of this work, but some strategies for future work have been provided in the recommendations section.

Testing in the simplified ocean-scale test channel provided the background understanding necessary to apply the methodology to a much more complex real-world environment: Minas Passage.

8.4 MINAS PASSAGE: NEAR FIELD CROSS-COUPLED METHOD

The near field-modeling approach was tested on the Minas Passage site by modeling four 16m diameter turbines, one at each of the FORCE test berths. Each of the four turbines was first modeled in CFD (as a porous disk) in a 200m x 200m area surrounding each berth with detailed bathymetry. Inflow and turbulence conditions were sourced from the Ocean model for the peak flood. To simplify the analysis only the M2 tidal component was used to drive the system. At peak flood (nominally U=2.5m/s) the total estimated power production in the Ocean model was 5MW. This value compares well with the total predicted in CFD, but there are differences in the power of individual turbines (10-26%). These differences arise due to inconsistencies in how each model resolves the flow in each sub-domain. Nonetheless, since the turbine parameters change little with operating conditions the Ocean model is still able to provide a robust estimate of power.

The near-field coupling method work shows great promise. The objective was to ensure consistency between the Ocean and CFD models and in large part this was achieved. This methodology has a range of potential applications including:

- estimation of total extractable power from a tidal system;
- informing wide tidal site selection,
- array layout and channel build-out;
- investigation of the impact of a tidal installation on current patterns and tidal range;
- Investigation of the impacts of tidal installations on one another, etc.

With this methodology, regulators, developers and other stakeholders in tidal energy can virtually investigate any number of 'what if' scenarios for the installations of free stream turbines before ever driving a pile or laying cable.

8.5 PETIT PASSAGE: MID FIELD CROSS-COUPLED METHOD

A mid-field cross-coupling method was successfully implemented and demonstrated for Petit Passage. In general results from the CFD simulations showed good agreement with Ocean model data, especially where the flow is relatively uni-directional and not dominated by large eddies. The final set of simulations run with the inclusion of a turbine also demonstrated the potential for using CFD to calculate power extracted by the turbine over a tidal cycle as well as the wake generated by the turbine. This methodology could therefore be extended to modeling tidal farm arrays with inclusion of turbine interaction effects.

At this point, the CFD model of Petit Passage is still considered preliminary because it has not been validated against field data. While ADCP measurements have been completed at several locations in Petit Passage, the data is not yet available for public release.

9 RECOMMENDATIONS FOR FUTURE WORK

The recommendations for future work are summarized as follows:

- Repeat the flume tank experiments using an actual spinning rotor instead of the porous disks to compare thrust and wake characteristics. This will provide a better understanding of the strengths and weaknesses of using porous discs as turbine facsimiles;
- Repeat CFD simulations of turbine arrays using more sophisticated turbine representations such as by using spinning actuator disks, actuator-line approaches, or modeling fully modeling the turbine blades. This will provide a better understanding each models capability to predict thrust and wake interactions representative of turbines that will be deployed;
- Investigate and develop methods of modeling turbine arrays in Ocean Models;
- Determine if the near-field cross-coupling method accurately accounts for channel blockage effects;
- Develop and test a full-coupled method by integrating Ocean and CFD models using custom "junction-box" routines that would update boundary conditions shared by both models every time step;
- Validated the CFD model of Petit Passage against field data;
- Implement a free-surface, or variable water surface for mid-field CFD models.

These recommendations are explained in additional detail below.

9.1 FLUME TANK EXPERIMENTS

It was observed that the wake downstream of the discs contained large scale eddies with a diameter approximately 1/3 of the disc diameter. These eddies were shed from the peripheral edge of the disc, and persisted for several diameters downstream before breaking-up into smaller scale turbulence. Due to the presence of these flow structures, isotropic turbulence is not a good assumption since the eddies contribute to momentum transfer with a preferred direction. Additionally, a time-averaged velocity field is not sufficient to fully describe such a flow and a more detailed characterization of the turbulence would be beneficial for better understanding of the flow. However, the value of such a study is limited since the wake structure behind a spinning rotor will differ from that of a porous disc. It is thought that the study of actual spinning rotors is of much greater benefit, and therefore UVIC will continue with detailed flume tank experiments of a spinning rotor in the near future.

9.2 CFD SIMULATIONS

It would be possible to spend a great deal of time tuning turbulence model coefficients and sources of turbulent kinetic energy to improve the match of CFD predictions to the measured wakes behind porous discs. It would also be possible to use large-eddy-simulation to better resolve the turbulence structures in the wake. However, considering that the wake behind a spinning rotor will differ from that of a porous disc, there is not a great deal of value in fine-tuning the turbulence parameters for the porous disc simulations. More time should be spent understanding how to best represent arrays of actual spinning rotors in CFD simulations. UVIC plans to use a combination of high-fidelity CFD methods, including actuator-line approaches, and experiments to work towards better understanding wake interaction effects in arrays of spinning rotors.

9.3 NEXT STEPS FOR NEAR FIELD METHOD

Issues with the near-field coupling methodology were identified both in the simplified ocean channel scenario and in the Minas Passage scenario. The CFD and Ocean models were found to provide differing results because the treatment of bottom friction and turbulence in each model were not strictly consistent. Further work should be done to investigate these inconsistencies and to determine whether they not they are important.

In the simulation of tight packed multi-turbine arrays it was found that the required averaging volume scaled with the entire size of the array rather than the individual turbines. Depending on the specific problem, this scale may be too large to resolve the large scale flows. A solution may be to use the concept of building blocks of turbines. This involves dividing the arrays along lines of symmetry, then using these planes as walls in the CFD model. The individual pieces would be assembled in the ocean model; the end turbines would require special treatment. It is recommended that this approach be investigated in future work. If successful it would extend the applicability of the near-field coupling method to tight packed multi turbine arrays.

Testing of multi-turbine arrays leads to discussion of blockage effects (where the presence of one turbine affects the performance of another). This is not believed to be an issue with the ocean model where any distribution of drag and closure is accepted and the flow adjusts accordingly. It is an issue with the CFD calculations however. At high blockage ratios ideal tidal turbine performance can no longer be considered independently; ideal turbine resistance coefficients may be much larger than those predicted by the Betz Limit. This leads into further discussion of independent turbine control within an array as investigated by Vennel [17]. Further research is required to identify how these concepts of blockage and control can be applied to the near field coupling methodology.

Finally, a natural extension of this work is incorporation of real turbine operation limitations (thrust and power parameters curves, cut-in, cut out speed, etc), so that the turbine parameters are a function of the ambient current velocity. This would provide better estimates at current velocity, drag and power outside of the turbine's ideal operating condition and more closely simulate the operation of a real turbine.

9.4 FULLY COUPLED APPROACH

The near-field coupling method presented in this report requires that CFD simulations be given boundary conditions from ocean-scale simulations. The work done applying the near-field approach to simulating turbines in Minas passage highlighted the workload involved in passing boundary conditions from one type of model to another. The workload may be reduced by developing software to actively pass boundary conditions and turbine forces between ocean-scale and CFD scale simulation codes. Fully coupling the methods in this manner has many advantages. For one, the need for empirical parameterization of the turbines as sub-grid entities is eliminated. This means that the power calculation will come directly from the CFD simulation, which can resolve local flows due to bathymetry and due to other turbines. UVIC plans to develop such a method by integrating FVCOM with CFX using Fortran "junction-box" routines.

A fully coupled model can provide a benchmark for other methods. This benchmark would be determined by running the coupled model with transient CFD simulations where the inflow boundaries

are updated for each timestep of the ocean scale model. This would be the highest fidelity option and therefore provide the best predictions of power production. It will also be very computationally expensive. With a benchmark established, several different lower fidelity (faster) approaches can be evaluated. For example, one approach would be a quasi-static method where the turbine is treated with a sub-grid model as done in the near field approach presented in this report. The CFD simulation would be run a few times throughout the tidal cycle to re-evaluate C_T* and C_P* at different phases of the tidal cycle. Many different schemes are possible, but without an established benchmark it would be difficult to assess the merits of each.

9.5 NEXT STEPS FOR MID FIELD METHOD

The next step in improving the mid-field cross-coupling approach is to validate the CFD models against field date. The validation work entails:

- Determining if the turbulence model chosen (DES-SST) is in fact the most suitable for modeling tidal flows;
- Mesh sensitivity study to determine if a coarser (or finer) mesh is required to best match ADCP results, especially in terms of vertical resolution;
- Time step study to determine if a time step larger than 2 seconds can be used in order to decrease overall computer time. For reference, it took approximately 24h of computer time to run 6h of real time using 6 processors in parallel. Increase the time step size (provided the simulation remains stable and valid) will make running multiple tidal cycles much more feasible.
- Determine impact of varying the bottom friction specification. For the simulations completed as part of this project, the solver default value for a smooth surface was used to set the bottom friction along the sea bottom. Specifying a roughness will likely impact the vertical velocity distribution by affecting the boundary layer growth. The roughness parameters should therefore be tuned to better match the field data.

Once the validation work is complete, the next step is to determine what impact the assumption of a fixed water elevation (fixed slip wall as opposed to a free air-water interface) has on the accuracy of results for modeling flows through Petit Passage.

For shallow channels experiencing a significant tidal range, a method will need to be developed to capture the changing water elevation. A number of options exist including:

- Creating a series of CFD models with varying depth and running incrementally over shorter durations;
- Modeling the air-water interface (this will significantly increase the computational time), or;
- Using a morphing mesh that allows the water surface to vary over the course of the simulation.

Clearly, significant work remains to standardize the mid-field cross-coupling method such that it can be applied with confidence for a wide range of tidal sites. Notwithstanding, the results to date are very promising and form a solid foundation for future work.

10 REFERENCES

[1] P. Lavoie, G. Avallone, F. Gregorio, G. Romano and R. Antonia, "Spacial resolution of PIV for the measurment of turbulence," *Experimental Fluids*, vol. 43, pp. 39-51, 2007.

[2] L. Benedict and R. Gould, "Towards better uncertainty estimates for turbulence statistics.," *Experiments in Fluids*, vol. 22, pp. 129-136, 1996.

[3] T. Tanaka and J. Eaton, "A correction method for measuring turbulent kinetic energy dissipation rate by PIV," *Experimental Fluids*, vol. 42, pp. 893-902, 2007.

[4] G. Corten, "Heat Generation by a Wind Turbine," *IEA Symposium on the aerodynamics of wind turbines, NREL*, vol. 14, Dec 4-5, 2000.

[5] H. Versteeg and W. Malalasekera, An Introduction to Computational Fluid Dynamics: The Finite Volume Method., vol. 2007, Pearson Education Limited, 2007.

[6] F. Menter, "Two-Equation Eddy-Viscosity Turbulence MOdels for Engineering Applications.," *AIAA Journal*, vol. 32, pp. 1598-1605, 1994.

[7] J. Bardina, P. Huang and T. Coaklye, "Turbulence Modeling Validation Testing and Development," *Technical Memorandum 110446, NASA*, 1997.

[8] M. Yaras and A. Grosvenor, "Evaluation of one and two equiation low Re turbulence models. Part 1: Axi-symmetric separating and swirling Flows," *International Journal for Numerical Methods in Fluids*, vol. 42, pp. 1293-1319, 2003.

[9] F. Menter, "Review of the shear-stress transport turbulence model experience from an industrial perspective," *International Journal of Computational Fluid Dynamics*, vol. 23(4), pp. 305-316, 2009.

[10] M. Shives, "Hydrodynamic Modeling, Optimization and Pe4rformance Assessment for Ducted and Non-ducted Tidal Turbines," MSc, University of Victoria, 2011.

[11] T.Burton, D. Sharpe, N. Jenkins and E.Bossanyi, Wind Energy Handbook, John Wiley & Sons Ltd, 2001.

[12] M. Harrison, W. Batten, L. Myers and A. Bahaj, "A comparison between CFD simulations and experiments for predicting the far wake of horizontal axis tidal turbines," in *EWTEC*, 2009.

[13] V. Nikora, I. McEwan, S. McLean, S. Coleman, D. Pokrajac and R. Walters, "Double-averaging concept for rough-bed open-channel and overland flows: Theoretical background," *Journal of Hydraulic Engineering*, vol. 133, pp. 873--883, 2007.

[14] V. Nikora and P. Rowiński, "Rough-bed flows in geophysical, environmental, and engineering systems: Double-Averaging Approach and its applications. Preface to the special issue," *Acta Geophys.*, vol. 56, pp. 529--533, 2008.

[15] R. Walters and D. Plew, "Numerical modeling of environmental flows using DAM: Some preliminary results," *Acta Geophysica,* vol. 56, pp. 918--934, 2008.

[16] R. Vennell, "Tuning tidal turbines in-concert to maximise farm efficiency," *Journal of Fluid Mechanics,* vol. 671, pp. 587--604, 2011.

[17] R. Vennell, "The energetics of large tidal turbine arrays," *Journal of Renewable Energy,* vol. 48, pp. 210--219, 2012.

[18] D. A. Greenberg, "A numerical model investigation of tidal phenomena in the Bay of Fundy and Gulf of Maine," *Marine Geodesy,* vol. 2, no. 161--187, 1979.

[19] C. Garrett, "Tidal Resonance in the Bay of Fundy and Gulf of Maine," *Nature,* vol. 238, pp. 441-443, 1972.

[20] P. V. Sucsy, B. R. Pearce and V. G. Panchang, "Comparison of Two- and Three-Dimensional Model Simulation of the Effect of a Tidal Barrier on the Gulf of Maine Tides," *J. Phys. Oceanogr.*, vol. 23, pp. 1231--1248, 1993.

[21] C. Garrett and P. Cummins, "Generating power from tidal currents," *Journal of Waterway, Port, Coastal and Ocean Engineering,* vol. 130, pp. 114--118, 2004.

[22] C. Garrett and P. Cummins, "The power potential of tidal currents in channels," *Proceedings of the Royal Society A: Mathematical, Physical and Engineering Sciences,* vol. 461, pp. 2563--2572, 2005.

[23] R. A. W. Tarbotton, C. E. Hiles and M. R., "Estimation of tidal power potential," *Journal of Renewable Energy,* vol. 51, pp. 255--262, 2013.

[24] D. R. Parrott, B. J. Todd, J. Shaw, J. E. H. Clarke, J. Griffin, B. MacGowan, M. Lamplugh and T. Webster, "Integration of Multibeam Bathymetry and LiDAR Surveys of the Bay of Fundy, Canada," in *Proceedings of the Canadian Hydrographic Conference and National Surveyors Conference 2008*, 2008.

[25] R. Karsten, "Tidal Energy Resource Assessment Map for Nova Scotia," *prepared for Offshore Energy Environmental Research Association,* p. 41, 2012.

[26] C. Chen, R. Beardsley and G. Cowles, "An unstructured grid finite volume coasta ocean model (FVCOM) system," *Oceanography,* vol. 19, pp. 78-89, 2006.

[27] Hay, "OERA report (in progress)," 2013.

APPENDIX A: OVERVIEW OF RICOM

The River and Coastal Ocean Model (RiCOM) was developed by Dr. Roy Walters formally of the National Institute for Water and Atmospheric Research of New Zealand and US Geological Survey who is now a modeling consultant with Cascadia Coast Research and formerly with Triton Consultants. RICOM was developed to solve some of the longstanding problems with finite element methods – namely lack of local mass conservation and problems with stability and/or accuracy with advection-dominated flows. In addition, a double-averaging method (DAM) has been incorporated into the model to allow an accurate approximation of subgrid objects and their effects on the volume averaged flow. The latter provides a means to couple the results of small-scale CFD models with the large-scale Ocean model.

RICOM solves the primitive hydrodynamic equations with a semi-implicit time-stepping scheme that is unconditionally stable with respect to time-step size so that the time-step size is controlled by the physics of the specific problem under consideration rather than by numerical constraints. Secondly, the model uses a semi-Lagrangian approximation for advection that is accurate, stable, and robust which yields accurate results without oscillations for high speed flows such as occur over weirs, in flow constrictions, and tidal rapids. Finally, the model uses a finite element spatial approximation that gives considerable flexibility in designing the computational grid. The particular elements that are chosen have no spurious modes so that the solution is free of grid-scale oscillations (Walters and Casulli, 1998; Walters, 2006; Walters et al, 2009). Because of the design of the algorithm, wetting and drying capabilities are inherent to the finite volume continuity equation and do not require any special attention. In addition, the model conserves mass both locally and globally which is an important property when dealing with solute and particulate transport, especially when the transport equations are in a finite volume form.

RiCOM is formulated from the Reynolds-averaged Navier-Stokes equations that are time averaged over turbulent time scales. The governing equations are derived using the Boussinesq approximation and by introducing a rotating frame of reference. The equations are spatially averaged to derive double-averaged equations that allow sub-grid spatial effects (vegetation, bottom roughness, etc.) to be included in a rigorous manner (Walters and Plew, 2008). The discretized equations are derived using a finite element approximation in space and a finite difference approximation in time. A more detailed description of the technical model background can be found in Walters et al (2009, model NPI).

Triton have applied RiCOM successfully to a number of recent projects including storm surge estimates for the southern Beaufort Sea (Canada), tidal dynamics in the Fraser River (B.C.), Cook Inlet Alaska, South West Korea, Discovery Islands (BC) and the Bay of Fundy/Minas Passage (years 2009 to 2011) in eastern North America. In all these projects the model was validated in both 2D and 3D mode against measured tidal height and ADCP current data. The later three projects include the determination and location of tidal current resources for two large ocean energy developments.

Two unstructured RiCOM computational model grids were developed for the 2009-2011 Bay of Fundy/ Minas Tidal Resource Modelling studies. Model 1 has a maximum resolution of 50-75 m in Minas Passage. Model 2 has a maximum resolution of 10-15 m in Minas passage. In both model grids the computational edge size reduces from about 17 km on the deepwater Atlantic driving boundary to the refined area of the model in Minas Basin and Minas Passage. In recent 2011 work the RiCOM model

was successfully validated (in both 2D & 3D) against 3D ADCP measurements (8 deployments) collected by DFO in 2009.

REFERENCES

Walters, R.A., 2006. Design considerations for a finite element coastal ocean model, Ocean Modelling 15, 90-100.

Walters, R.A. and Casulli, V., 1998, A robust, finite element model for hydrostatic surface water flows. Communications in Numerical Methods in Engineering 14, 931-940.

Walters, R.A., and D.R. Plew, 2008. Numerical Modeling of environmental flows using DAM: Some preliminary results. Acta Geophysica 56(3), 918-934.

Walters, R.A., Hanert, E., Pietrzak, J., Le Roux, D.Y., 2009. Comparison of Unstructured, Staggered Grid Methods for the Shallow Water Equations. Ocean Modelling 28, 106--117.

APPENDIX B: PIV SOFTWARE SETTINGS:

Specific software options for processing instantaneous vector fields using Davis 7.2 are described in the following:

- **Image pre-processing:** Some images did not have constant background intensity, which can interfere with the correlation function evaluation. The option *subtract sliding background* was used to normalize the background intensity. A length scale of 10px (approximately 3 times the average particle diameter) was chosen for this option.
- **Correlation mode:** Since images were taken using the double-frame double-exposure model, the vectors were calculated using cross correlation between the two frames taken for each recording.
- **Adaptive multi-pass processing**: An initial vector field was first computed using large interrogation windows 128px × 128px. The next pass used 64px × 64px and the windows were shifted in the second frame using the vector field from the first pass. Shifting the windows reduces the number of particles leaving the interrogation window in the second frame and therefore allows the vector field to be computed with better resolution. The final pass used 32px × 32px windows.
- **Oversampling:** The interrogation windows overlapped each other. The greater the overlap, the higher resolution the flow field solution for a fixed interrogation window size. 50% overlap was used for all passes of the multi-pass processing, and the final flowfield therefore had a resolution of 16px ≈ 1.7mm.**Correlation Function Evaluation:** The correlation function was evaluated using a cyclic fast Fourier transform (FFT) approximation which is much faster (≈ 50×) than a direct evaluation. The selected software option was *I1 × I2 via FFT with no zero padding*. This method requires that the pixel displacement **i**s less than 1/3 of the (shifted) interrogation window and therefore requires iterative reduction of the window size (see the bullet on adaptive multi-pass) for good results. The correlation function is calculated for each interrogation window and maps correlation intensity to displacement (dx,dy). The peak correlation corresponds to the most likely displacement within the interrogation window. In multi-pass processing, the window is shifted in the second frame, so the total displacement used to calculate the velocity is equal to the window displacement plus the displacement found using the correlation function.
- **Q criterion:** sometimes the correlation function gives multiple peaks, resulting in some ambiguity about the true velocity. When there is only one peak, there is a low probability that the computed vector is erroneous. When two peaks have similar magnitude, the vector may be erroneous and is deleted. With reference to figure a quality parameter can be defined: $Q = \frac{P1-min}{p2-min}$. Any vectors with Q<1.3 were removed to reduce the likelihood of bad vectors.

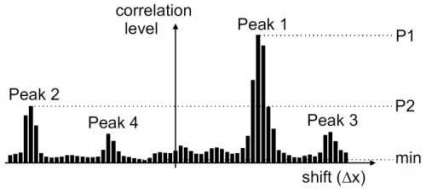

Figure B-1: The correlation function may produce multiple peaks

- **Median Filter:** The Q-criterion is sometimes insufficient for identifying erroneous vectors, so an additional vector removal strategy called a median filter was also used. The selected software option was *strongly remove and iteratively replace*. This filter involves several steps that will not be discussed here, but the general strategy is to remove any vectors which were different by more than X (user choice set to X=2) standard deviations from the median of their neighboring vectors. This filter is robust and eliminates most bad vectors. Sometimes this filter leaves isolated small groups of vectors (which may be erroneous) and an additional removal criterion that groups of less than 4 vectors be deleted was also used.
- **Interpolation:** Once the above two filters have been applied there are typically some holes in the vector field. These were filled-in using the average of all remaining neighbor vectors. (This is applied iteratively)

The vector removal and filling-in of missing vectors are applied at each step of the adaptive multi-pass procedure. This is important because erroneous vectors would produce incorrect window shifts which would then produce more bad vectors. After the final pass, the Q-criterion and median filter were re-applied for post processing. An additional 3×3 smoothing filter was also applied to ensure a smoothly varying velocity field.

APPENDIX C: DISSIPATION RATE CALCULATION

This appendix gives further detail regarding the calculation of the turbulent dissipation rate using the available PIV data.

Most of the turbulent kinetic energy is contained in the largest scale turbulent eddies (with length scale L_ϵ). So it is a reasonable approximation to assume that the dissipation rate can be defined by;

$$\epsilon = \frac{k^{\frac{3}{2}}}{L_\epsilon} \tag{36}$$

Once the dissipation rate is estimated, the Kolmogorov scale can be found from its definition;

$$\eta = \left(\frac{\nu^3}{\epsilon}\right)^{\frac{1}{4}} \tag{37}$$

Now, there is an additional complication due to the fact that PIV inherently under-predicts the fluctuating velocity components at wavelengths which are short relative to the data resolution. Each velocity vector calculated by PIV represents an averaged quantity taken from a sampling volume with dimensions L × L × H where L is the spatial dimension of the interrogation window and H is the lesser of the laser sheet thickness or the camera depth of focus. This volume averaging inherent in PIV filters out fluctuations below a certain cutoff wavelength. An analytical correction has been defined by Lavoie et al. (2007) to correct for this spatial attenuation. A strict application of the method would require *a-priori* knowledge of the turbulence spectra, which is unavailable for the present experiments. However, given that only the inertial subrange (which is similar in all turbulent flows) is of interest for the present method, the particular spectra used in determining the correction factor is of little relevance. As such, the correction $R_{ui}(K_1)$ was applied using interpolation between the curves provided by figure 2 of Lavoie et al. (2007). Note that $R_{ui}(K_1)$ is a function of wavenumber, and depends on the ratio of the PIV sampling volume size to the Kolmogorov scale η. The energy spectra were corrected according to;

$$E_{ii}^{correct}(K_1) = \frac{E_{ii}^{meas}(K_1)}{R_{ui}(K_1)} \tag{38}$$

The general procedure for the method was as follows:

1. Use a one-dimensional FFT to find averaged $E_{11}(K_1)\ and\ E_{22}(K_2)$ from N_t vector fields.
2. Find the turbulent kinetic energy
3. Assume an integral length scale L_ϵ
4. Calculate the dissipation rate and Kolmogorov scale.
5. Determine the spatial resolution correction $R_{ui}(K_1)$
6. Non-dimensionalize the obtained energy spectra.
7. Plot the corrected PIV spectra and the universal theoretical spectra together.
8. Tune the length scale and repeat steps 3-7 until the corrected PIV spectra and the theoretical spectra match-up in the inertial subrange.

The method was applied to the PIV data for the most upstream frame of case 7b. For this particular case, the PIV vector field was determined using interrogation windows of 12px×12px=1.7mm×1.7mm.

The resulting energy spectra for each sample in time are plotted in Figure C-1. The averaged and corrected energy spectra are plotted along with the theoretical spectra for the inertial subrange in Figure C-2.

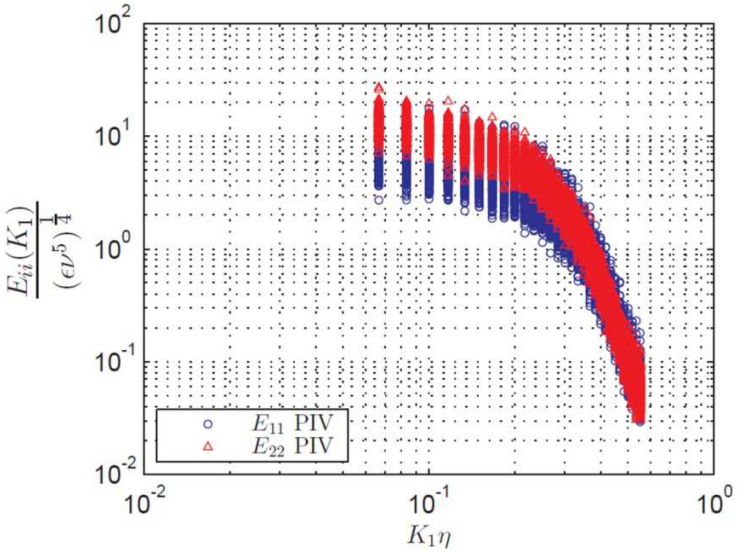

Figure C-1: One-Dimensional turbulence energy spectra from PIV data

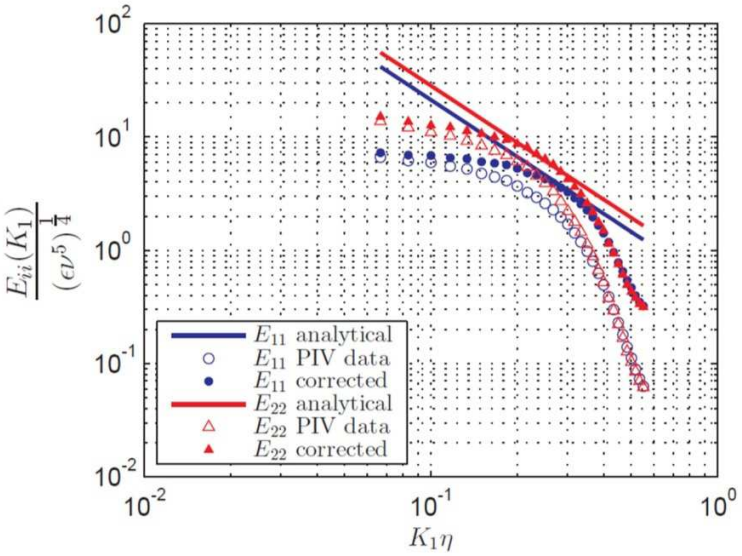

Figure C-2: Averaged one-dimensional turbulence energy spectra from PIV data compared to theoretical spectra for the inertial sub-range

APPENDIX D: MAVI MESH REFINEMENT STUDY

1. Momentum Source Mesh Study

A limited mesh study was completed to ensure mesh independent results. The Set 1 experimental configuration was used a test case. The free surface was not modeled. A trimmer mesh model was used to generate the mesh because, in looking forward, the trimmer model is particularly well suited for resolving the air-water interface. Figure D-1 shows the five models of varying mesh densities that were run. Mesh element sizes were scaled by a factor of $\sqrt{2}$ between Mesh 1, 2, and 3, with Mesh 1 being the highest density mesh. The density of Mesh 4 and 5 were defined to have total cell counts between Mesh 1 and 2. The level of mesh refinement was varied both in the far field as well as in close proximity to the disks. A comparison case was also run using a polyhedral cell model as shown in Figure D-2.

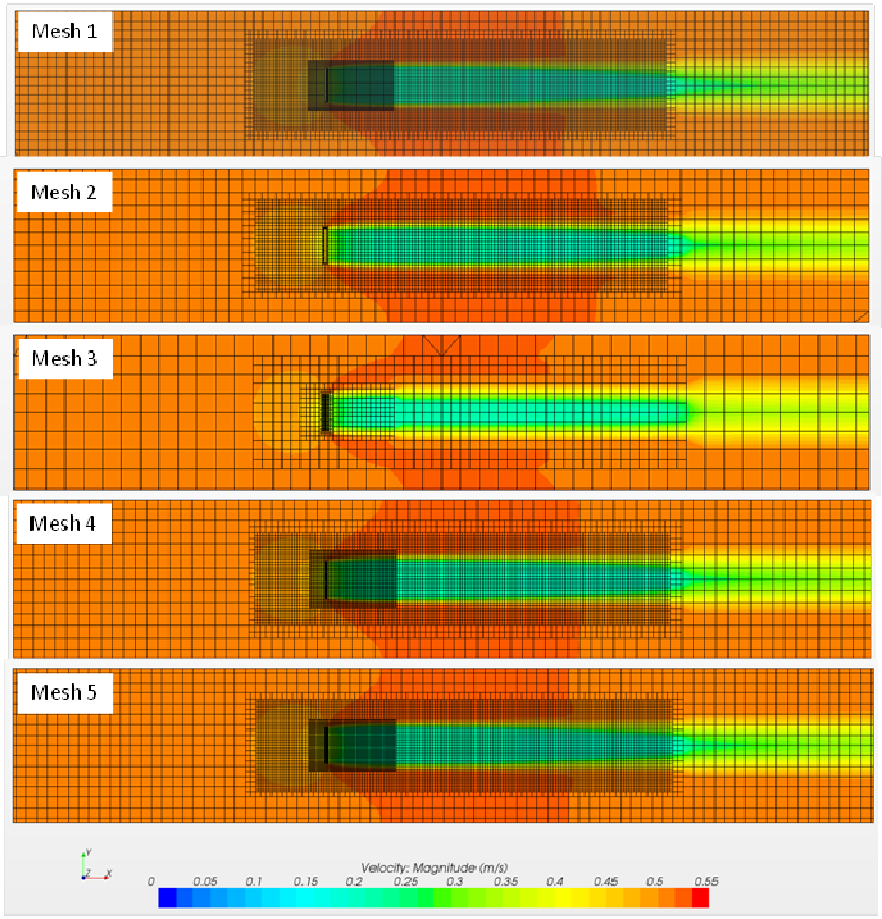

Figure D-1: Horizontal Plane along tank centerline shoiwn gmesh refinement

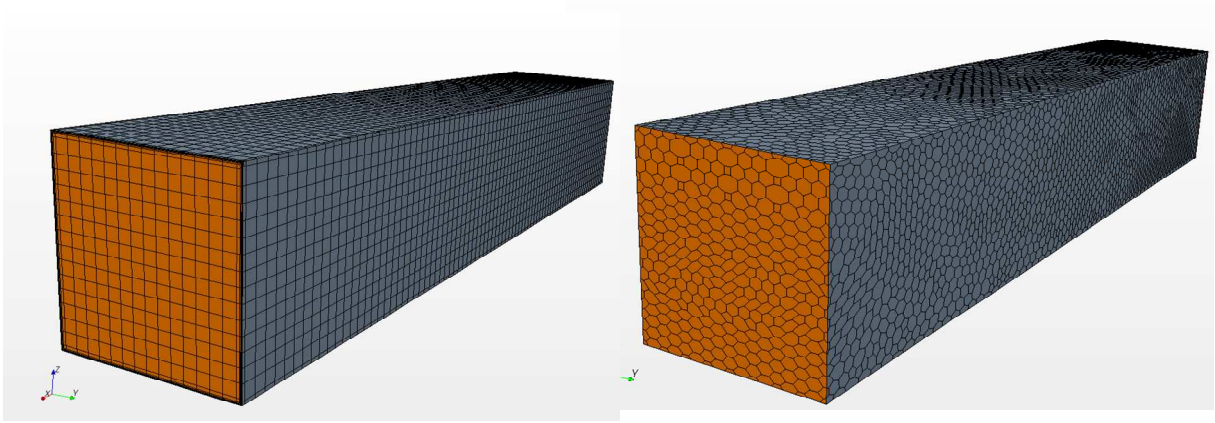

Figure D-2: Trimmed mesh with prism layers (left), Polyhedral mesh without prims layers (right)

The key parameters used and the results of the mesh refinement study are presented in Table D-1. Disk thrust and power were calculated by summing the thrust and power values through each mesh cell on the disk. The same momentum source strength was specified for all simulations. The following formula was used to estimate the momentum source strength need to achieve the target thrust coefficient of 0.9.

$$Mom.Strength = \frac{\frac{1}{2}\rho v^2 C_T}{thk}$$

Where:

ρ is the density of water;

v is the velocity at the inlet;

C_T is the thrust coefficient, and

t is the thickness of the disk.

The volume averaged x-direction velocity passing through the disk was also monitored for comparison. The results show that the strength of the momentum source estimated using the above formula needs to be increased to achieve the desired thrust coefficient. Nonetheless, a comparison can be made to determine the level of mesh density required to ensure valid results.

Table D-1: CFD results from mesh refinement study

Number of Cells	Sim.	Inlet Velocity	Target C_T	X-Mom. Strength [N/m^3]	Disk Force [N]	Disk Velocity [m/s]	Disk Power (W)	Measured C_T	Measured C_P
17374	SET_1-a-msh3	0.50	0.90	22433	0.742	0.343	0.26396	0.758	0.5393467
101892	SET_1-a-msh2	0.50	0.90	22433	0.738	0.342	0.26277	0.754	0.5369143
217404	SET_1-a-msh4	0.50	0.90	22433	0.780	0.351	0.2795	0.797	0.5710991
290576	SET_1-a-msh5	0.50	0.90	22433	0.772	0.351	0.27616	0.789	0.564291
373539	SET_1-a-msh1	0.50	0.90	22433	0.771	0.352	0.27476	0.787	0.5614118
354996	SET_1-a-msh5 poly mesh	0.50	0.90	22433	0.766	0.352	0.26983	0.782	0.5513531
333584	SET_1-a-msh5 prim mesh	0.50	0.90	22433	0.771	0.367	0.28288	0.788	0.5780046

As shown in Figure D-3, Mesh 5 provides a good compromise between accuracy and mesh density.

In order to evaluate the choice of meshing model on the measured thrust (trimmer vs. polyhedral mesher), the Mesh 5 parameters were used with a polyhedral mesh model. A percent difference of 1.7% was calculated for the power coefficient.

An additional model based on Mesh 5 was created with a prism layer along the tank walls, bottom and top with adequate refinement to capture the boundary layer. For this model, the walls were specified with a non-slip condition. The refinement along the walls was specified to achieve a y+ value of approximately 1 as required by the SST model.

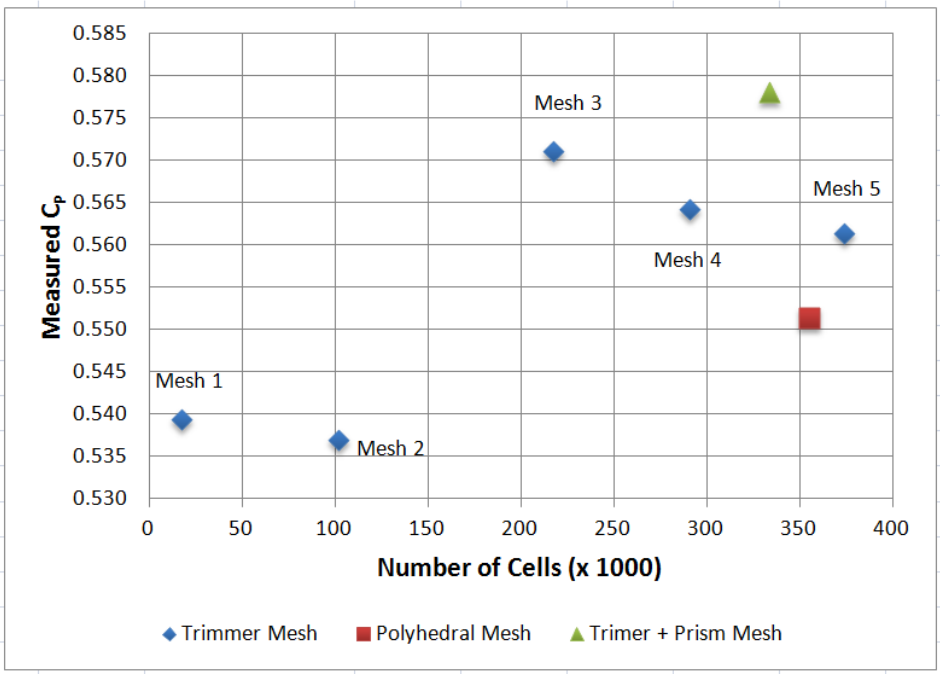

Figure D-3: Results from Mesh Density Study

Figure D-4 provides velocity contour plots on a horizontal plane centered along the disk contrasting the case of using slip walls vs. no-slip walls. Even though the calculated thrust on the disk was nearly identical for both cases, some variation in the flow field can be observed, especially near the walls. At this point in the study, this variation is noted but deemed to be second order given that the impact on measured thrust is negligible.

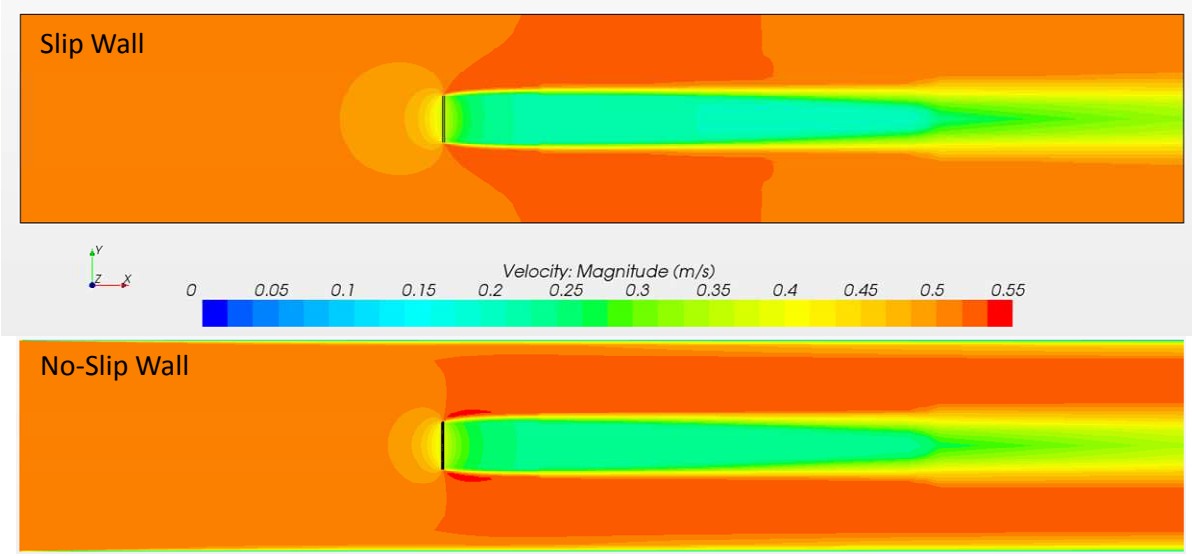

Figure D-4: Velocity magnitude contours comparing a model run with and without slip walls

2. Porous Disk Mesh Study

For future simulations with the porous disk, a limited mesh study was completed on the porous disk simulations to ensure mesh independent results. The Set 1 experimental configuration was used as a test case. The free surface was not modeled. In the previous mesh study the trimmer meshing model was used because this model is well suited to resolving the air-water interface and it was expected that a free-surface would need to be modeled as the project progressed to modeling large ocean channels. However, initial simulations of these large channels suggest that accurately capturing the free-surface shape is not necessary when modeling these submerged turbines operating at low blockage ratios. Therefore, for the porous disk mesh study, the polyhedral mesher was used due to the greater control over mesh density it provides.

Five unstructured polyhedral meshes of increasing density were generated and run at a free-stream velocity of 0.5m/s. Mesh element sizes were scaled by a factor of 1.3 between the meshes. All simulations were run at the default turbulence intensity of 1%. Table D-2 contains the mesh details and thrust and power coefficient results.

Table D-2: Porous disk mesh study results

Mesh	# of Elements	C_T	C_P
A	1109524	0.919	0.601
B	491421	0.919	0.602
C	267245	0.923	0.605
D	143446	0.923	0.605
E	78345	0.930	0.611

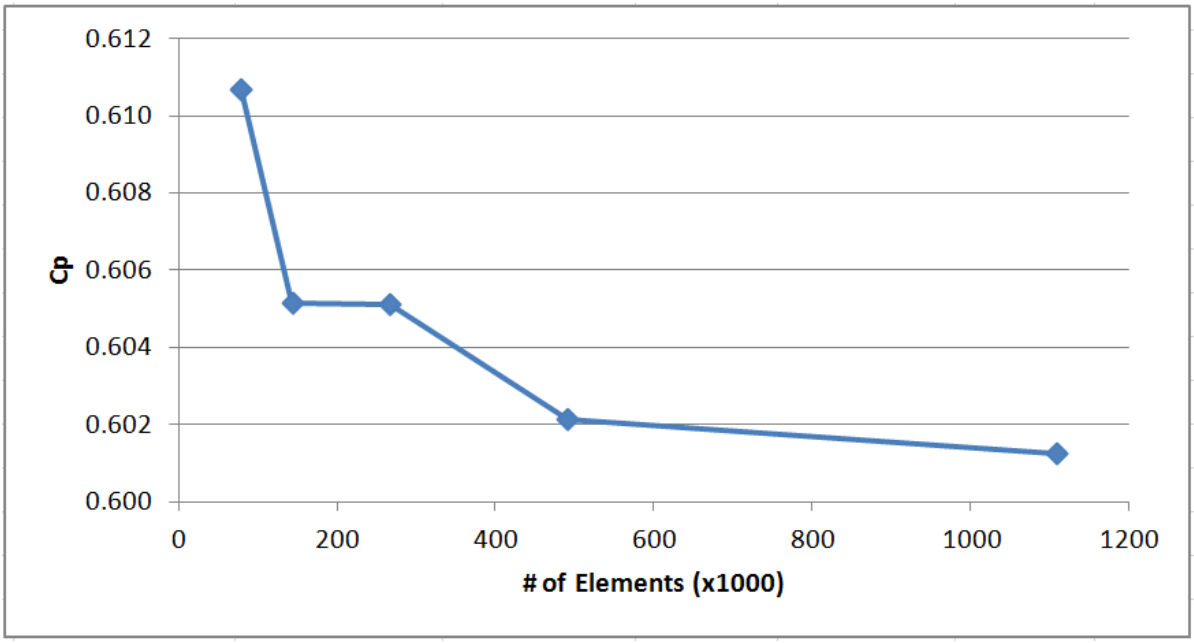

Figure D-5: Power coefficient vs. number of mesh elements for porous disk simulations

Figure D-5 shows the power coefficient vs. the number of mesh elements. Over the range of mesh sizes run, there is a small variation in C_P. The difference in C_P between the highest density mesh (Mesh A) and the lowest (Mesh E) is 1.57%. The difference between Mesh C and Mesh A is 0.64%. Mesh C provides a good compromise between accuracy and computational time and therefore is used in all subsequent single disk simulations.